OPTIMIZATION OF PROCESS PARAMETERS FOR THE MANUFACTURE OF 3D PRINTED BIOPOLYMER COMPOSITE FOR MEDICAL IMPLANTS

GAUDENCE NYIRANZEYIMANA

DOCTOR OF PHILOSOPHY
(Mechanical Engineering)

JOMO KENYATTA UNIVERSITY
OF
AGRICULTURE AND TECHNOLOGY

2023

Optimization of Process Parameters for the Manufacture of 3D Printed Biopolymer Composite for Medical Implant

Gaudence Nyiranzeyimana

A Thesis Submitted in Partial Fulfilment of the Requirements for the Degree of Doctor of Philosophy in Mechanical Engineering of the Jomo Kenyatta University of Agriculture and Technology

2023

DECLARATION

This thesis is my original work and has not been presented for a degree in any other university.

Signature..... Date...../...../.....

Gaudence Nyiranzeyimana

This thesis has been submitted for examination with our approval as university supervisors:

Signature..... Date...../...../.....

Dr. James Mutuku Mutua, PhD

JKUAT, Kenya

Signature..... Date...../...../.....

Dr. Thomas Ochuku Mbuya, PhD

UoN, Kenya

Signature..... Date...../...../.....

Dr. Bruno Robert Mose, PhD

JKUAT, Kenya

DEDICATION

To my lovely husband Dieudonne Ruzigamanzi, our daugther, Nicole Manzi Ineza, and my parents.

ACKNOWLEDGMENT

I am grateful to the Almighty God for protecting me throughout this research. I am deeply thankful to my supervisors, Dr. James Mutuku Mutua, Dr. Thomas Ochuku Mbuya, and Dr. Robert Bruno Mose, for their guidance, encouragement, assistance, and patience throughout the research. Their insightful inputs assisted in generating and producing high-quality research findings. I thank the University of Rwanda, Japan International Cooperation Agency (JICA) through the Africa –ai-Japan Project, and the German Academic Exchange Service (DAAD) for funding this research. I would also like to acknowledge the support of Mr Kimani Joseph for helping in formatting and organizing this thesis. In addition, I wish to appreciate Mr. Emmanuel Bisengimana for his help during the experiments. Finally, my sincere gratitude to my family for their understanding, continuous encouragement and unconditional love.

TABLE OF CONTENTS

LIST OF TABLES

LIST OF FIGURES

LIST OF APPENDICES

LIST OF ABBREVIATIONS

ABS	Acrylonitrile Butadiene Styrene
AM	Additive Manufacturing
ANOVA	Analysis of Variance
ASTM	American Society for Testing and Materials
CAD	Computer Aided Design
CF/PA12	Carbon Fiber Polyamide 12
DMLS	Direct Melting Laser Sintering
DoE	Design of Experiment
EBM	Electron Beam Melting
FDM	Fused Deposition Modelling
FEA	Finite Element Analysis
FEM	Finite Element Method
GA	Genetic Algorithm
GRA	Grey Relational Analysis
GRG	Grey Relational Grade
LOM	Laminated Object Manufacturing
PEEK	Polyether Ether Ketone
PBF	Powder Bed Fusion
PLA	Polylactic Acid
RS	Residual Stress
SEM	Scanning Electron Microscope
S/N	Signal to Noise
SLA	Stereolithography
SLS	Selective Laser Sintering
SLM	Selective Laser Melting

.stl	Standard Tessellation Language
UoN	University of Nairobi

LIST OF SYMBOLS

$\boldsymbol{\alpha}$	Coefficient of thermal expansion
$\boldsymbol{\bar{a}_{jk}}$	Calibration matrix for isotropic stresses
$\boldsymbol{\bar{b}_{jk}}$	Calibration matrix for shear stresses
$\boldsymbol{\beta}$	Direction of maximum principal stress (degrees)
$\boldsymbol{c_p}$	Specific heat of the printed material
$\boldsymbol{h}$	Convective heat coefficient
$\boldsymbol{k}$	Thermal conductivity
$\boldsymbol{q}$	Heat generation rate
$\boldsymbol{\{\epsilon_t\}}$	Thermal strains
$\boldsymbol{\rho}$	Density of the printed material
$\boldsymbol{\{\sigma\}}$	Thermal stresses (MPa)
$\boldsymbol{t}$	Time (seconds)
$\boldsymbol{T_c}$	Building chamber temperature (°C)
$\boldsymbol{\sigma_{max}}$	Maximum principal stress (MPa)
$\boldsymbol{\sigma_{min}}$	Minimum principal stress (MPa)

ABSTRACT

One of the most applied additive manufacturing processes for fabricating functional parts from composite polymers is fused filament fabrication. Carbon fiber-reinforced composites have been widely used for many applications, especially in medical implants. Due to their better stiffness and strength-to-weight ratio compared to metallic materials. Although fused fabrication filament is now a well-established additive manufacturing process for producing parts from these materials. However, it is still limited in its applicability in the industry due to inherent problems, such as significant residual stresses. Residual stresses negatively affect the mechanical properties and dimensional accuracy of additively built products. The effect of residual stresses cannot be corrected by post-processing like heat treatment. As a result, determining input process parameter combinations that result in minimal residual stresses is crucial. In this study, Digimat-AM 2020 software was used in prediction of residual stresses, deflection and build time for different process parameters. In fused filament fabrication process, printing temperature, layer height, and print speed are very critical to mechanical properties. These parameters were varied based on the literature and material manufacturer. Minitab 2018 software was used to determine the influence of process parameters on the mechanical properties of fused filament fabrication of CF/PA12 composite hip joint implant. Experiments were done to validate the results. The grey relational Taguchi method was used to obtain the optimal process parameters. The significance of the process parameters on the part characteristics was determined using an analysis of variance. Taguchi's results showed that the optimal factor setting levels required for minimizing part deflection, residual stresses, and printing time differed. However, Grey relation analysis showed that optimal factors were: a printing temperature (255°C), a layer thickness (0.3 mm), and a print speed (50 mm/s). From the results, printing temperature had the strongest influence on the part characteristics. Experimental results showed a near convergence of the observed deflection, residual stresses, and printing time values with a percentage difference of 8.34 %, 2.5 %, and 4.61 %, compared to simulated results. The surface roughness of the 3D printed hip implant were: 1.51 μm, 1.5 μm, and 1.61 μm. These values were within the acceptable range of below 2 μm for better bone-to-implant contact. From the tensile test, the average values of ultimate strength, compressive strength, Young's modulus, and percentage elongation of the printed CF/PA12 hip joint implant were 71.48 MPa, 135.8 MPa, 7.54 GPa, and 1.86 %, respectively. In addition, the fatigue life for all investigated loadings was greater than or equal to 10^5 cycles. These results were within the acceptable range of cortical bone and hip implant performance properties. The fused filament fabrication method was found to work well with CF/ PA12 composite, making it possible to produce hip implants with acceptable mechanical integrity.

Other medical trial tests were recommended for further study.

CHAPTER ONE

INTRODUCTION

This chapter presents a detailed background of the additive manufacturing process. Different additive manufacturing techniques, advantages, applications, challenges, and materials have been presented. In addition, clarifications on the problem and objectives of this study has been provided.

1.1 Background

Three-dimensional (3D) printing or additive manufacturing (AM) technique can be defined as a manufacturing technology that generates 3D solid objects from digital information (Banjanin et al., 2018). Contrary to the conventional subtractive manufacturing processes, in 3D printing, an object is manufactured by feedstock material layer by layer and fusing. The additive manufacturing starts with preparing a 3D computer-aided design (CAD) model of the part. The 3D CAD file is then converted to a standard tessellation language (.stl) file, which is used to break down the geometrical representation of the object into a group of triangular facets. The .stl file is used by a specific slicing software to virtually slice the model into very thin layers which are equal to the building layer thickness.

The slicer program allows the manufacturer to set process parameters depending on the part material, required product size, and surface finish. The data is then sent to a 3D printer where the printing materials are loaded, melted and fused to create a 3D product. The finished product is removed from the machine and taken through several post-processing techniques such as cleaning the part, removing supports, depowdering, post-curing, infiltration of resin or wax, and draining excessive resin.

3D printing has several advantages, such as fabricating parts with complex geometrical shapes within a short period without incurring an extra expense in tooling, reducing part count, handling time, ability to change the design easily and quickly, and capability to minimize material waste (Attaran, 2017; Kumbhar & Mulay, 2018; Mansour & Hague, 2003). Additive manufacturing has found application in developing fully functional components for aerospace, automotive, and medical applications Tran, Nguyen, Ngo, and Nguyen (2017). This technique has been used to fabricate components using different materials such as metals, ceramics, polymers, and composites (Hegab, 2016).

Recently, additive manufacturing provides a great opportunity for the medical industry to rapidly-produce medical implants (Aimar, Palermo, & Innocenti, 2019). Custom medical scaffolds, hearing devices, and dental implants have all been created using 3D printing technology (Prasad et al., 2017). In this study, a custom-made hip implant for medical application was considered. Hip replacement is one of the most common and effective operations, with more than one million hip replacements performed each year worldwide (Polozov, Sufiiarov, & Borisov, 2016). Figure 1.1 (a) shows a natural hip joint covered with articular cartilage which acts to lubricate joint with synovial fluid, and thus providing a smooth motion. The cartilage in the hip joint gradually wears away over time, as illustrated in Figure 1.1 (b). The solution for the damaged hip is a hip replacement, as shown in Figure 1.1 (c) Kapadia (2018). In response to the growing demand for custom-made hip implants, additive manufacturing was investigated in this study to assist the production of the implants. The conventional manufacturing of customized hip implant is time consuming and costly. Therefore, it is expected that additive manufacturing will provide a quick and efficient method of producing this implant.

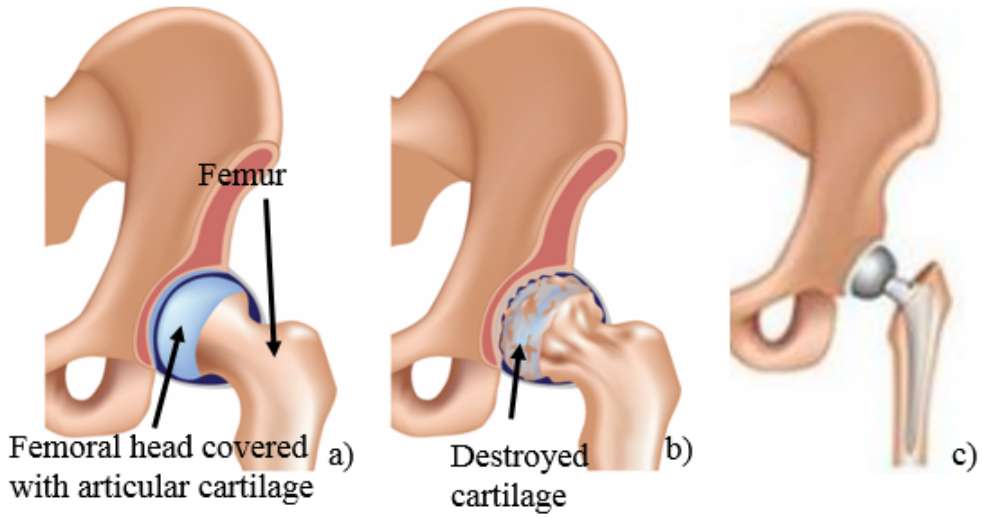

Figure 1.1: (a) Normal anatomy of hip joint, (b) damaged hip, and (c) hip implant

Despite its success, hip replacement is still associated with various problems relating to the implant's lifetime (Higuchi, Seki, Takegami, Komatsu, & Morita, 2018). One of the most serious issues is the release of wear particles from the implant's bearing surface Z. Xia et al. (2017). The accumulation of wear particles causes bone loss and aseptic implant loosening. Another issue is stress shielding which causes bone resorption when the implanted bone is subjected to mechanical loads lower than normal bone loading resulting in micro-movements at the bone-implant interface (Ridzwan, Shuib, Hassan, Shokri, & Mohammad Ibrahim, 2007)

These drawbacks are typically observed with metallic implants because they have higher stiffness and density properties than cortical bone (Dimitrievska, Whitfield, Hacking, & Bureau, 2009). Among biometals, stainless steel (316L), cobalt-chromium (CoCr) alloys, and titanium (Ti) alloys are the most widely used metals for hip replacement (Van Noort, 1987). The difference in stiffness between the implant and the femur produces bone resorption, weakening the host bone and causing the aseptic loosening of the implant (D. Wang, Dou, & Yang, 2018). Biocompatible and biostable composite polymers are replacing metallic materials

in making implant devices (Teo et al., 2016). The materials have high corrosion resistance, reliable mechanical properties, and similar stiffness to human bones (Teo et al., 2016).

Different additive manufacturing techniques including selective laser melting (SLM), selective laser sintering and fused filament fabrication (FFF) are available for fabricating medical implants (Katschnig & Holzer, 2018; Shahali, Jaggessar, & Yarlagadda, 2017). Both SLM and SLS only allow the production of complex-shaped individual implants from powdered metals and polymers (Shahali et al., 2017). Polymer composites have been developed and standardized as feedstock filaments for FFF process (Mostafa, Montemagno, & Qureshi, 2018). Due to the advantages of the use of polymer composites, FFF process has been selected as it is the only AM technique to fabricate composite filaments and reduces material waste compared to SLS.

1.2 Fused Filament Fabrication

Fused filament fabrication (FFF) has been used to produce biomedical components from thermoplastic polymer filaments (Buj-Corral, Domínguez-Fernández, & Durán-Llucià, 2019; Mathew, Domínguez-Robles, Larrañeta, & Lamprou, 2019).

Different thermoplastics such as ultra-high molecular weight polyethylene (UHMWPE), polyether ether ketone (PEEK), and nylon, as well as polymer composites have been developed for fused filament fabrication implants (Wickramasinghe, Do, & Tran, 2020). However, FFF products have low dimensional precision, poor mechanical characteristics, high residual stresses, and noticeable surface roughness (Hanon, Zsidai, & Ma, 2021; Mohan, Senthil, Vinodh, & Jayanth, 2017). This quality characteristcs have been attributed to suboptimal FFF process parameter settings provided by the user (Christiyan, Chandrasekhar, & Venkateswarlu, 2016).

Several FFF process parameters influence the quality characteristics of FFF printed parts (Morales, Fleck, & Rhoads, 2018). These factors include layer thickness, build orientation, raster angle, print speed, infill density, air gap, and nozzle temperature (Chavan, Anwar, & R, 2017; Mutua, 2018). The meaning of some FFF process parameters shown in Figure 1.2 O. A. Mohamed, Masood, and Bhowmik (2016a); Rayegani and Onwubolu (2014) are define as:

1. Raster angle is defined as the angle formed by the printing platform's x-axis and the nozzle's path during printing.

2. Layer thickness refers to the height of the deposited layer in AM process.

3. Air gap is the space between two consecutive rasters.

4. Build orientation is another important FFF process parameter which refers to the way the printed part is oriented in a print bed with respect to x, y, and z axes.

5. Raster width is the width of the deposited material, and it is determined by the diameter of the extrusion nozzle. Print speed is the distance traveled by the nozzle along the x-y plane per unit time during extrusion.

6. Extrusion temperature refers to the temperature at which material is extruded from the nozzle during FFF process.

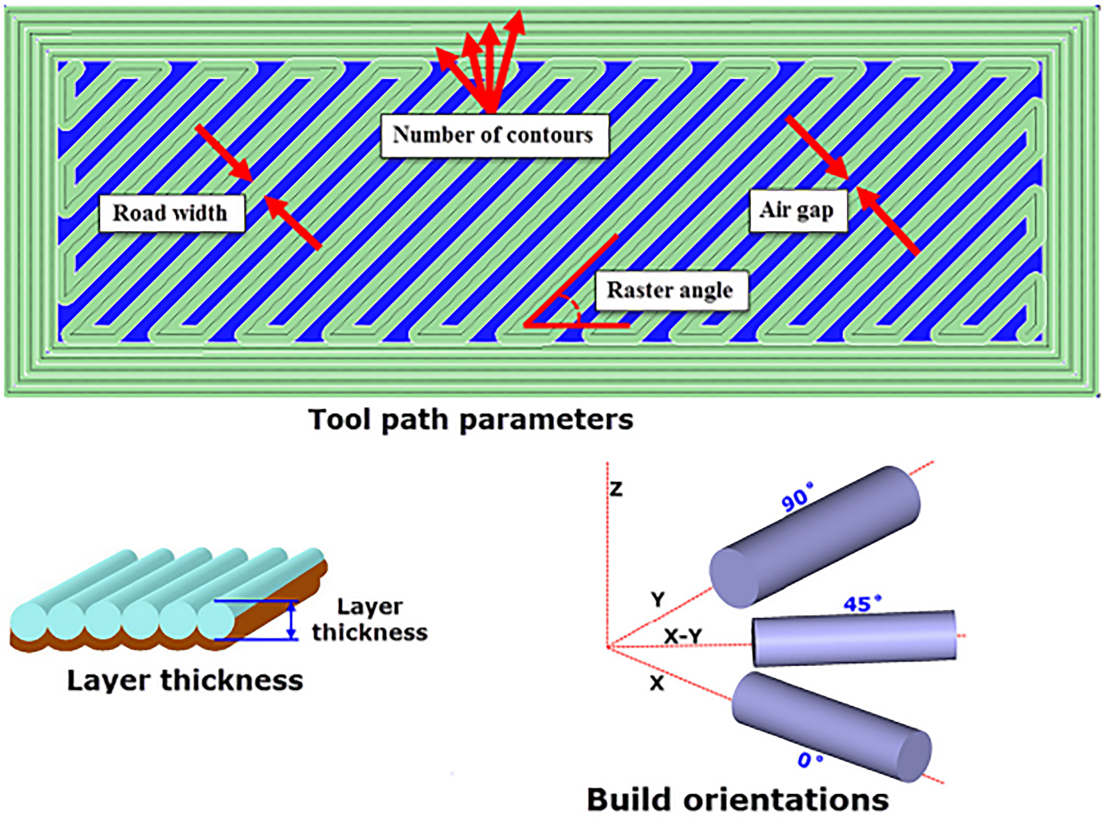

Figure 1.2: FDM process parameters

The printing parameter affect part quality such as mechanical properties, dimensional accuracy, and surface roughness. Apart from part characteristics, minimizing build time is reducing production cost (Mostafa et al., 2018). Build time is also affected by FFF process parameters, and it can be reduced by selecting the optimum combination of process parameters (Pavan Kumar & Regalla, 2012). Optimizing the FFF process parameters can improve both mechanical properties and build time for the 3D printed parts (Rodríguez-Panes, Claver, & Camacho, 2018).

Many studies on FFF printing materials focus on two commonly available polymers: acrylonitrile butadiene styrene (ABS) and biocompatible polylactic acid (PLA) (Rahim, Abdullah, Akil, Mohamad, & Rajion, 2017). However, these materials do not possess properties such as biocompatibility, tensile strength, flexural

strength, and durability required for medical implants (S. Kumar, Kannan, & Sankaranarayanan, 2014; Othman, Fadhil, & Hind, 2018). Recent manufacturing advancements have enabled the production of biocompatible and fatigue-resistant carbon fiber reinforced plastics for implants having properties similar to human bone (Haleem & Javaid, 2019; Han et al., 2019). These composites include carbon fiber/Ultra-high molecular weight polyethylene (CF/UHMWPE), carbon fiber/PEEK, and carbon fiber/PA12. Carbon fiber /UHMWPE and carbon fiber/PEEK have been widely studied for bone replacement (Brockett, Carbone, Fisher, & Jennings, 2017). Palaniappan *et al.* (Palaniappan et al., 2020) demonstrated that CF/UHMWPE composite releases wear debris, which may start osteolysis, causing implant loosening and bone degeneration. Carbon fiber/PEEK has a relatively high melting point of around 343 °C as compared to other polymer composites which makes it difficult to process with FFFF. Carbon fiber-reinforced nylon 12 (CF/PA12) is the latest developed composite material for biomedical application. This material has good biocompatibility, low cost, good mechanical qualities, and low melting temperature (Dimitrievska et al., 2009; Nyiranzeyimana, Mutua, Mose, & Mbuya, 2022).

1.3 Residual Stresses and Effects of Process Parameters on AM parts

During the AM, thermal energy of the deposited material is redistributed into the part through conduction and is consumed by lateral convection cooling (Y. Zhang & Chou, 2006a). Different regions of the AM part experience repetitive heating and cooling cycles (Mukherjee, Zhang, & DebRoy, 2017a). The variation in thermal gradient between subsequent layers results in residual stresses in the printed part, hence affect the quality of the final product such as mechanical properties and dimensional accuracy (Y. Zhang & Shapiro, 2017).

The residual stresses developed during processing may also cause localized distortion and/or micro cracks, resulting in weak bonding and consequently impact negatively the part's strengths (Mercelis & Kruth, 2006). Furthermore, when compared to a stress-free state, large residual stresses can limit the load resistance of the parts. Studies showed that residual stresses are sensitive to the processing parameters as they affect layer-to-layer bonding process (Mercelis & Kruth, 2006; A. S. Wu, Brown, Kumar, Gallegos, & King, 2014). Residual stresses are undesirable in the AM process. Residual stresses effects can be reduced by optimizing the process parameters in the AM process.

Additive manufacturing parts are prone to the porosities that affect tensile and fatigue strength, as they act us damage initiation (Al-Maharma, Patil, & Markert, 2020). These defects are linked to process parameters like infill density and layer thickness. Porosity decreases with an increase infill density causing high part strength and elastic modulus (Abeykoon, Sri-Amphorn, & Fernando, 2020). Research has suggested that the undesirable pores can be mitigated by properly configuring the process parameter levels (du Plessis, 2019; Kasperovich, Haubrich, Gussone, & Requena, 2016).

1.4 Problem Statement

Additively manufactured parts tend to be far inferior to conventionally manufactured ones in terms of mechanical properties such as tensile strength, compressive strength, and ductility (Jatti, Jatti, & Patel, 2019). The process parameters generally affect the printed parts' quality and build time. During the FFF building process, each layer of material cools down by conduction and convection before the next layer of melted filament is deposited on top of the previous layer, which makes the material solidified. The bonding process involves the local remelting of the previously deposited material and fusing it with the new layer. Remelting and fast cooling may induce non-uniform thermal gradients (Casavola, Cazzato, Moramarco,

& Pappalettera, 2017b). Improper process parameter selection result in prolonged printing time. These extended printing time contribute to high thermal gradients. As a consequence, residual stresses are developed in the build parts. These unbalanced stresses cause part deflection and compromised mechanical properties of the printed parts (Nyiranzeyimana, Mutua, Mose, & Mbuya, 2021). These residual stresses effects are unaffected by post-processing methods like heat treatment and are increased by improper setting of FFF process parameters (W. Zhang et al., 2019). To reduce residual stresses; different printing parameters such as the nozzle temperature, component positioning on the build plate, layer height, printing speed, and infill density need to be optimized (Mugwagwa, Yadroitsev, & Matope, 2019). Although research on the impact of FFF process parameters on the most common polymers, such as ABS and PLA has been carried out (Deng, Zeng, Peng, Yan, & Ke, 2018; W. Wu et al., 2015), there has been little research on the optimization of FFF process parameters on polymer composites for medical implants. The mechanical performance of the implants are crucial for most joint arthroplasty and must meet specific criteria for high load-bearing applications. Therefore, it is necessary to optimize FFF process parameters to achieve high quality AM parts of CF/PA12 hip joint implant.

1.5 Objectives

The main objective of this study is to determine the optimum process parameters for FFF CF/PA12 hip joint implant. To achieve this objective, the following specific objectives were accomplished:

1. To design a hip joint implant and determine the optimum processing parameters for 3D printing through simulation.
2. To print a hip joint implant and carry out mechanical tests of the printed hip joint implant.

3. To evaluate the performance of the designed hip implant by comparing the simulated and experimental results.

4. To compare the mechanical properties of the 3D printed hip joint implant prototype with those of the actual bone to be replaced.

1.6 Justification

Additive manufacturing is advanced manufacturing technology that reduces production costs and minimizes production time compared to injection molding and casting(Caminero et al., 2019). Fused filament fabrication, stereolithography (SLA), selective laser melting, and selective laser sintering are the current AM dominant processes used in the manufacture of medical implants (Zhu, Liu, Cai, & Wu, 2017). Selective laser melting and SLS work on metal and polymer-based powder as a starting material (Jia, Sun, Wang, Wu, & Wang, 2021). Among AM technique, fused filament deposition is the leading additive manufacturing technology used for fabricating plastic filament materials directly from CAD data. However, the quality of a 3D printed product is affected by improper setting of FFF processing parameters. Considering the significant economic benefits of using 3D printing, optimizing the AM process parameters is important. This approach will improve the 3D printed products. This will allow direct use of the 3D printed products with prolonged service. Metal implants are still plagued by biomechanical mismatches in elastic modulus between implant and host tissue (Bougherara, Bureau, & Yahia, 2010). To reduce stress shielding, efforts have been undertaken to develop low matching stiffness materials (Bougherara et al., 2010). Among these new materials, CF/PA12 provide sufficient corrosion resistance and good biocompatibility (Campbell, Bureau, & Yahia, 2008). Although, CF/PA12 composite has been developed for the implants, its processabity with FFF technique is still limited.

1.7 Thesis Structure

This thesis is divided into five chapters. The first chapter covers the background, current problem, objectives, and justification. Chapter two outlines the review of research that has been done carried out on the hip implant and materials used for the hip implants. The effect of FFF process parameters on part quality, optimization methods for FDM process parameters, residual stresses in 3D printed parts, and numerical simulation of the FFF process are also provided in chapter two. Chapter three describes the methodology that has been used to achieve the objectives of the research. Chapter four presents and discusses the results obtained from simulations and experiments. The conclusions of this research are presented in chapter five, along with recommendations for additional research to be conducted in order to further improve hip implant.

CHAPTER TWO

LITERATURE REVIEW

2.1 Introduction

Three-dimensional printing technology has become popular in the medical field due to its cost-effectiveness and production flexibility. It is used to fabricate customized devices for patients. Due to the growing demand for patient-specific medical items, 3D printing is expected to assist the production. The capacity of 3D printing to produce quickly using only a CAD model enables on-demand fabrication, allowing the in-house manufacture of medical devices.

Three-dimensional printing, in particular fused filament deposition allows the creation of complex-shaped individual implants from carbon fiber reinforced polymer composites with good biocompatibility, superior stiffness and high strength-to-weight ratio compared to metallic materials (Han et al., 2019). The properties of fused filament deposition parts are generally affected by process parameters. Poor selection of the process parameters results in substantial residual stresses leading to lower mechanical strength and dimensional inaccuracy Casavola et al. (2017b).

This chapter presents different additive manufacturing techniques, hip joint implant materials and research works on hip joint implants. The effect of FFF process parameters on part quality, optimization methods for FFF process parameters, residual stresses in 3D printed parts and numerical simulation of FFF process are also reviewed. Summary of gaps that need to be addressed in further research are presented in this chapter.

2.2 Additive Manufacturing Techniques

In 2012, the American society for testing and materials (ASTM) (*ASTM F2792-12a "Standard Terminology for Additive Manufacturing Technologies"*, 2012) categorized AM into seven techniques: Vat Photopolymerization, Material Jetting, Binder Jetting, Material Extrusion, Powder Bed Fusion, Direct Energy Deposition, and Sheet Lamination. Each of these techniques is discussed in the following subsection.

2.2.1 Vat Photopolymerization

Vat photopolymerization is one of the 3D printing techniques that uses liquid photopolymer resin, out of which the model is fabricated layer by layer. An ultraviolet (UV) light is used to cure or harden the resin where required. Once the first layer is formed, the platform moves the object being manufactured downward. After chemically hardening the resin onto a build platform, a new layer is cured. This process continues to build the part from the bottom until it is finished and removed (Aduba et al., 2019). Figure 2.1 shows the basic working principle of vat photopolymer. The process however requires support for overhanging features. Post-processing is also necessary to improve dimensional accuracy and mechanical properties. Stereolithography (SLA) is an example of vat photopolymerization that uses ultraviolet light to cure photopolymeric resins. Nonetheless, materials selection for vat photopolymerization is limited to photopolymers. Secondly, only photopolymer materials are used in this process due to their ability to change properties when exposed to ultraviolet light (W. L. Wang, Cheah, Fuh, & Lu, 1996).

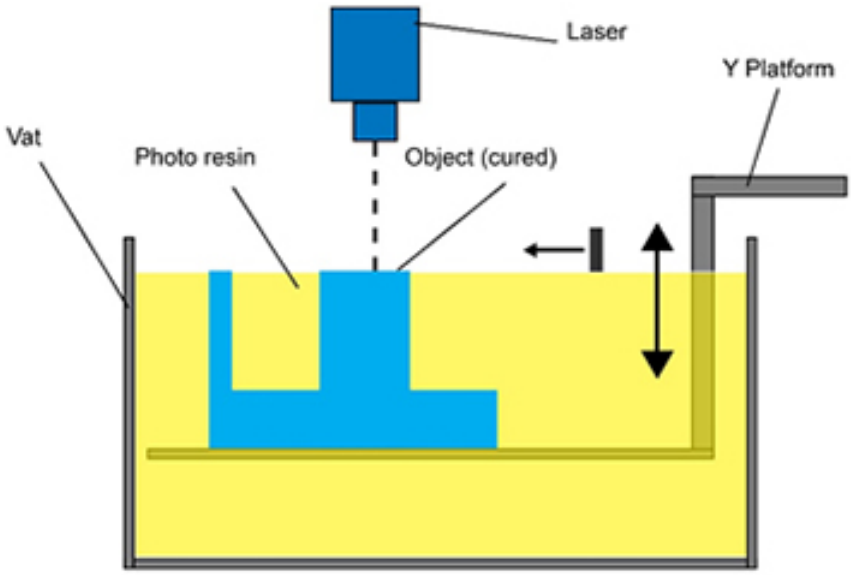

Figure 2.1: Principle of vat photopolymer (Dancel, 2019; Monzón et al., 2017)

2.2.2 Material Jetting Process

In the material jetting process, droplets of the liquid base material are deposited layer by layer to develop a 3D object (Tyagi, Yadav, & Deshmukh, 2021). Material is jetted from a heated print head using either a continuous or drop-on-demand (DOD) approach. The droplets of the material are deposited onto a build platform or surface, and a thermal or piezoelectric energy source is used to heat the print head, as shown in Figure 2.2 (Barclift; & Williams, 2019). Post-processing of produced parts, such as support removal or curing using ultraviolet light, is usually required (Monzón et al., 2017), since the raw material is usually deposited in drops. Polymers and waxes are suitable and commonly used materials due to their viscous nature and ability to form droplets (Elkaseer et al., 2022). This process provides a good surface finish, but the mechanical properties of the manufactured parts are low (Tyagi et al., 2021).

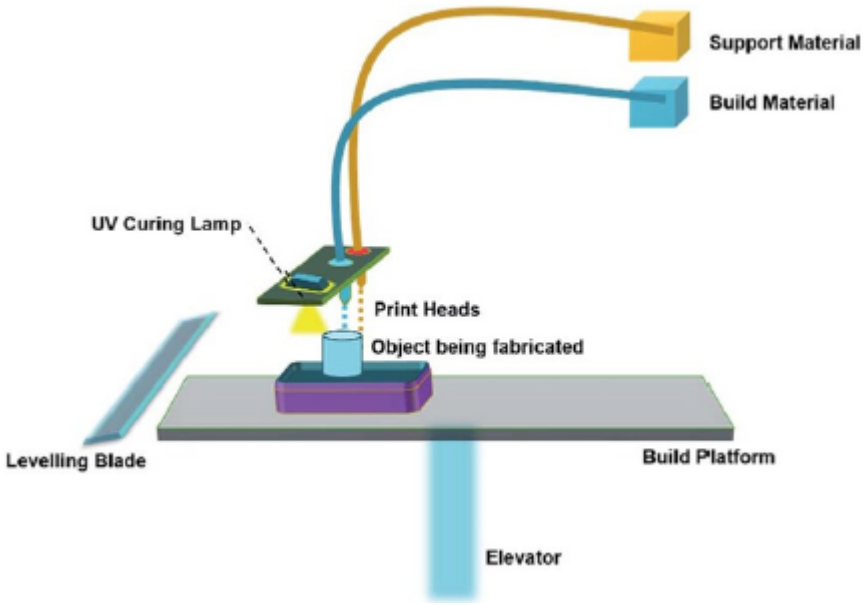

Figure 2.2: Material jetting process

2.2.3 Binder Jetting Process

The binder jetting process uses a liquid binding agent which is selectively deposited to join powder particles (Mostafaei et al., 2021). Layers of material are bonded together to form a 3D object. In this process, the powder material is first deposited into a build platform after which a print head then drops the binder into the powder to form a layer (Mostafaei et al., 2021). A platform then moves down to a distance that is equal to the layer height and another layer of powder is spread while the binder is added again (Mostafaei et al., 2021). This process continues until the desired product is achieved. Figure 2.3 illustrates the basic working principle of binder jetting process (Y. Wang, Xu, Wu, & Bai, 2020). Binder Jetting is capable of printing a variety of materials such as metals, plastics, ceramics and sand. Post-processing of the produced part such as curing, sintering and sometimes infiltration with another material to improve the surface finish and mechanical properties may be required (Kumbhar & Mulay, 2018; Mirzababaei & Pasebani, 2019). This process does not need any additional support structures since the powder supports the part that is

being produced (Lecis, Beltrami, & Mariani, 2021).

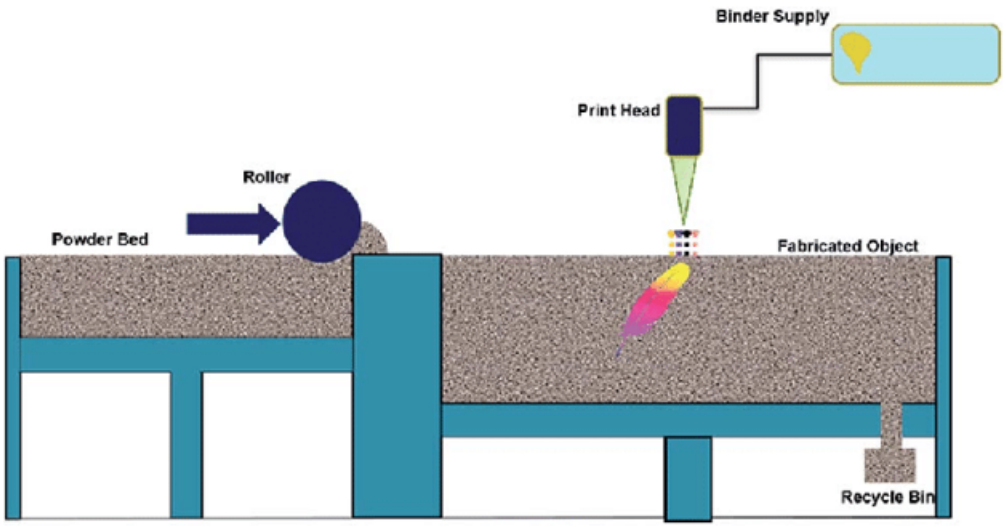

Figure 2.3: Binder jetting process

2.2.4 Extrusion Process

The extrusion process is another technique of AM. In this process, a thermoplastic filament is melted using a heater element at a temperature above its melting point and then pushed through a nozzle of a predetermined diameter as shown in Figure 2.4 (Dancel, 2019). As the nozzle moves in the X-Y direction, the molten thermoplastic filament is deposited layer by layer in the horizontal direction on the heated platform (O. A. Mohamed, Masood, & Bhowmik, 2016b). The platform's temperature is set low to solidify the thermoplastic quickly. Once the first layer is formed, the nozzle starts printing the second layer on top of the preceding layer, and the process continues until the 3D object is completely built (O. A. Mohamed, Masood, & Bhowmik, 2016b). This method is suitable for applications that use thermoplastic materials. Example of such extrusion process is fused deposition modelling (FDM) or fused filament fabrication (FFF). The process is cheaper, but the surface quality of the final product is poorer (Geng et al., 2019).

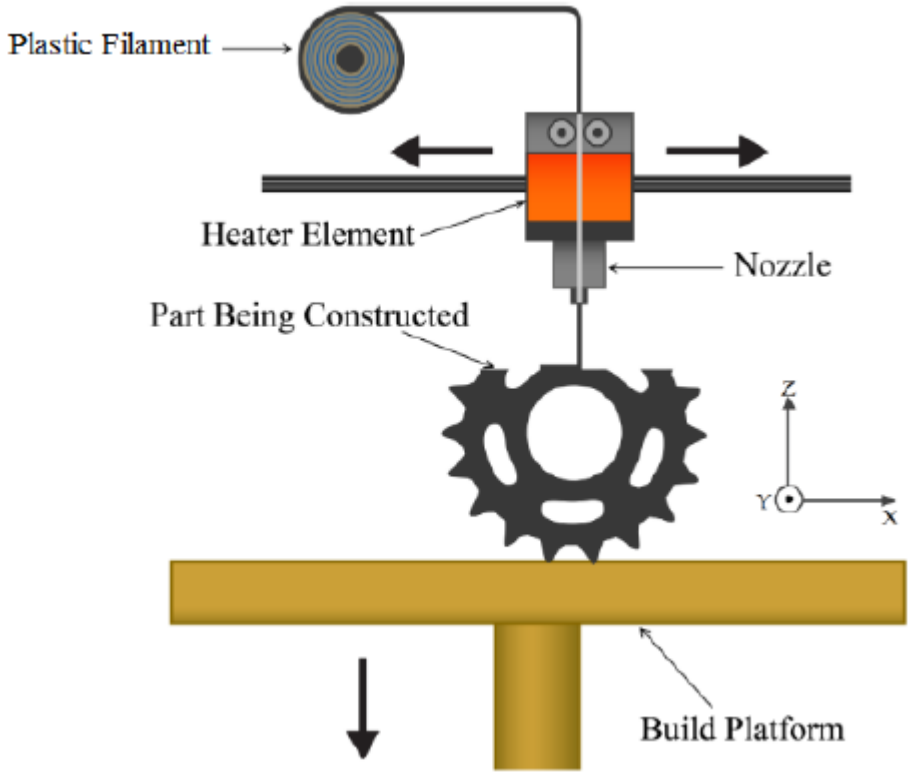

Figure 2.4: Principle of extrusion process

2.2.5 Powder Bed Fusion

The powder bed fusion (PBF) reates a 3D part layer by layer using powder in which the powder is sintered or melted using a heat source such as a laser or an electron beam (Megahed, Mindt, N'Dri, Duan, & Desmaison, 2016). In this process, the powder material is spread over the build platform, and a heat source is used to fuse the first layer of the part. A new layer of powder is spread on the previous layer using a roller. Both the previous and the new layers are then fused. This process is repeated until the 3D part is completed (Bhavar et al., 2017; Udroiu, 2012). Figure 2.5 shows the basic working principle of the powder bed fusion process (Dancel, 2019; Dutta & Sam Froes, 2015). The loose and unfused powder remains positioned to support the part that is being fabricated, which is to be removed during post-processing. Materials ranging from plastics to metals are printable using this

technique. Powder bed fusion processes include direct metal laser sintering (DMLS), electron beam melting (EBM), selective heat sintering (SHS), selective laser melting (SLM) and selective laser sintering (SLS) (Udroiu, 2012).

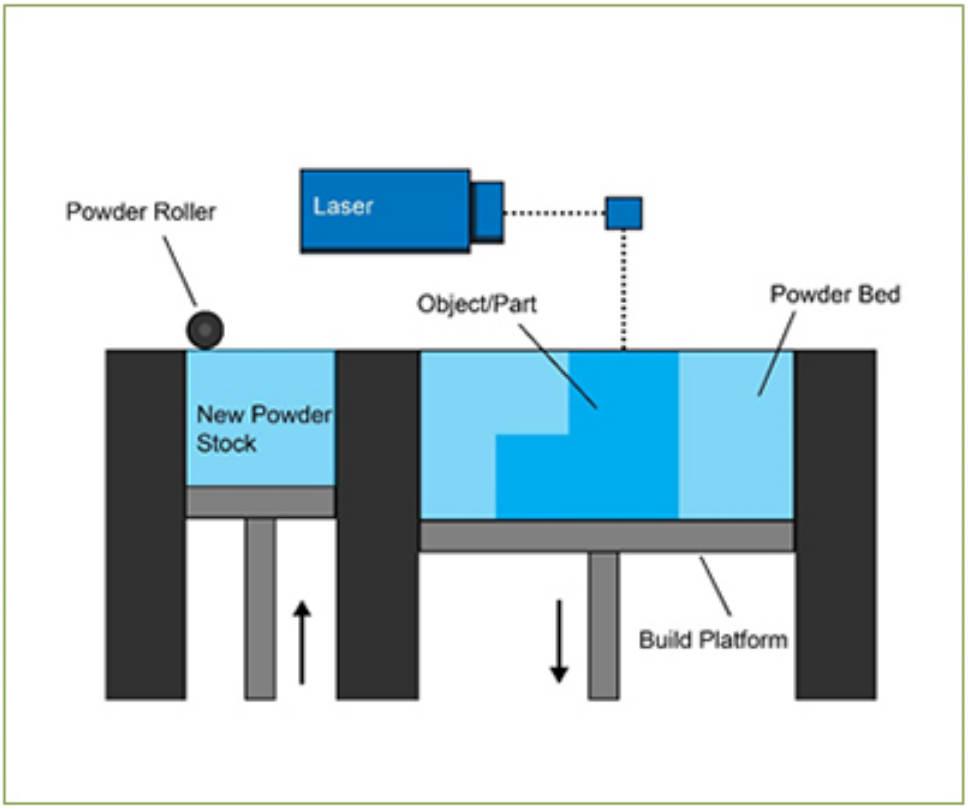

Figure 2.5: Principle of powder bed fusion process

2.2.6 Direct Energy Deposition

Direct energy deposition (DED) is another AM method that is used in the fabrication of 3D objects by utilizing a focused energy sources like a plasma arc, laser beam, and electron beam to melt the material as it is deposited by a nozzle in the form of wire or powder as shown in Figure 2.6 (Dancel, 2019). This technique is similar to both the powder bed fusion and material extrusion techniques. As opposed to the powder bed fusion techniques where material is melted while being deposited, DED melts the material predeposited on the build platform (Lim, Oh, Lee, & Kim, 2021).

The deposition can be done from different angles by using 4 or 5-axis machines. Direct energy deposition is the most suitable AM technique for re-fabricating and renewing aerospace and automotive components Dass and Moridi (2019); Saboori et al. (2019). Many AM technologies involved in this category include direct light fabrication (DLF), electron beam direct manufacturing (EBDM), direct metal deposition (DMD), direct laser deposition (DLD), and laser engineered net shaping (LENS) (Dass & Moridi, 2019).

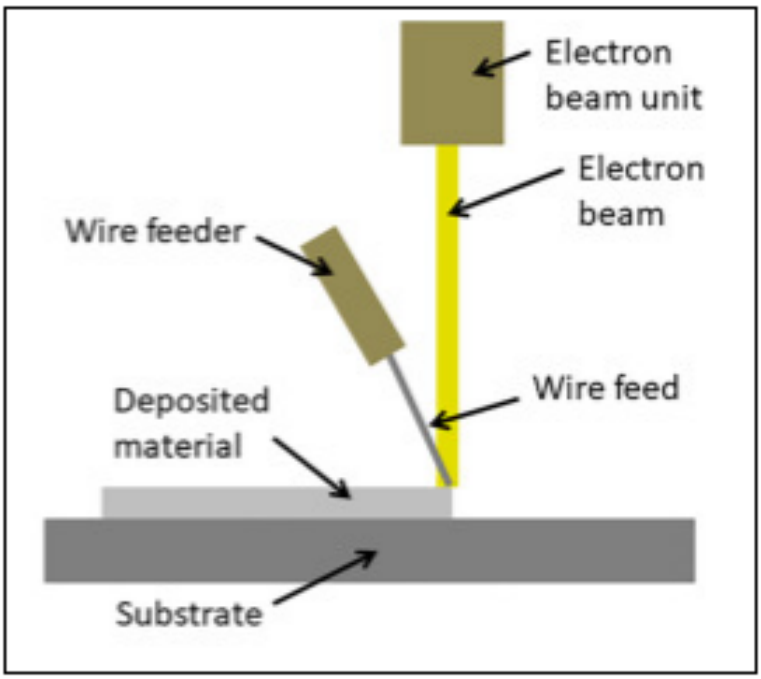

Figure 2.6: Principle of direct energy deposition process

2.2.7 Sheet Lamination

Sheet lamination is another additive manufacturing process where sheets of material such as paper or metal foil are bonded together using a heated roller to form a 3D part (Dancel, 2019; Pilipović, Šercer, & Raos, 2011). In this process, a sheet material is put on the build platform, and a bonding agent is placed on the material. The manufacturing machine adds layer and then bonded using pressure. A laser

beam then cuts the unwanted material to the desired shape (Ramya & Vanapalli, 2016). This process is repeated until the product is completed. Sheet lamination is a less accurate AM technique used by manufacturers to print non-functional prototypes and other basic designs out of easily handled materials (Pilipović et al., 2011). Sheet lamination technique includes ultrasonic additive manufacturing (UAM), laminated object manufacture (LOM), and selective deposition lamination (SDL). Laminating technology can be used to produce complicated products at low temperatures compared to powder bed fusion and direct energy deposition processes (Pilipović et al., 2011).

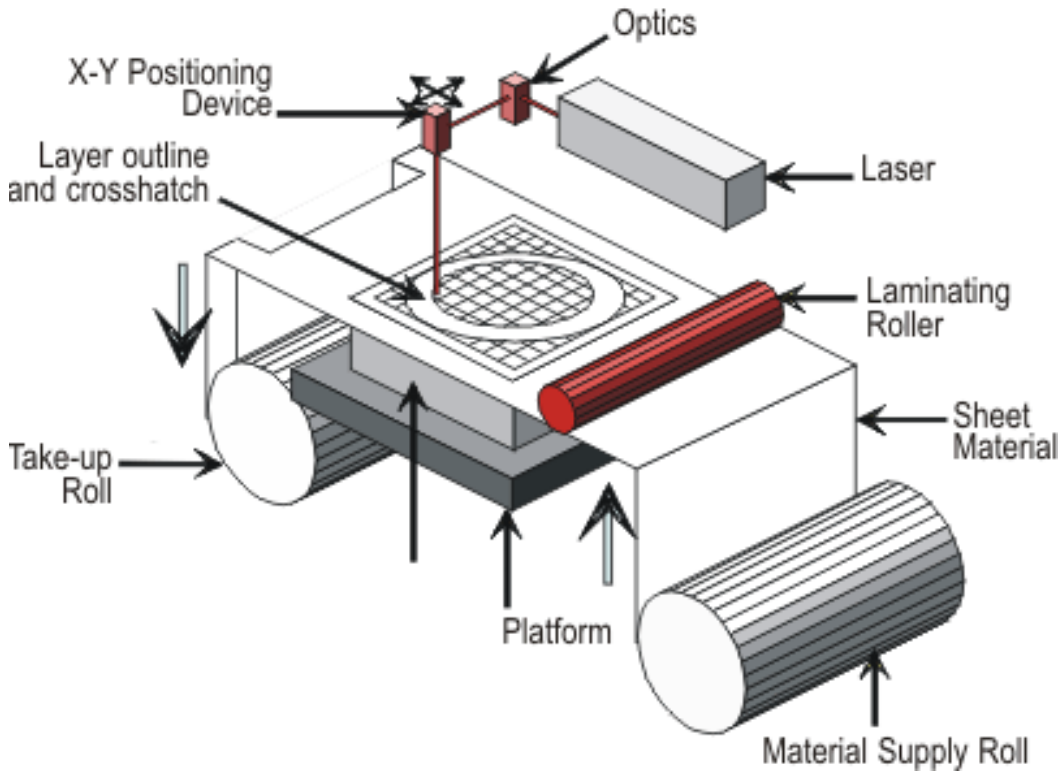

Figure 2.7: Principle of sheet lamination process

2.2.8 Summary of Additive Manufacturing Techniques

Based on the different kinds of input materials, 3D printing technology can be categorized as solid, liquid, or powder, as shown in Figure 2.8.

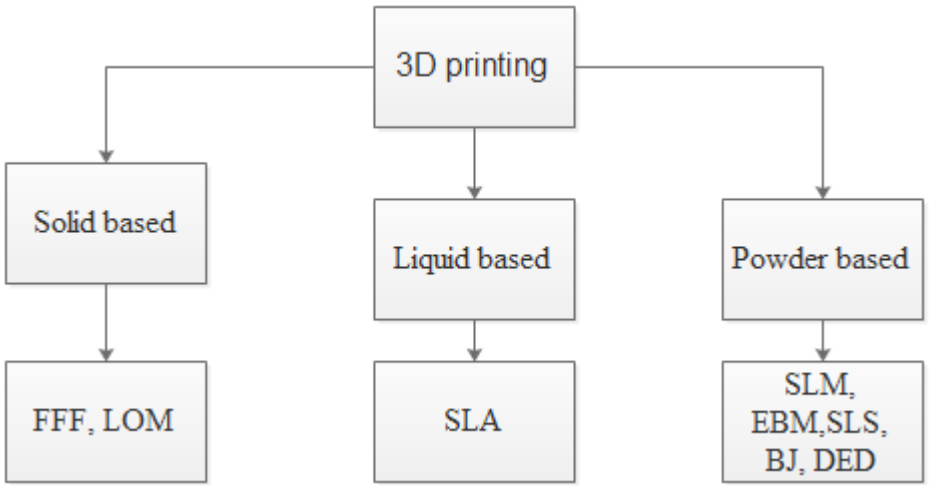

Figure 2.8: Summary of 3D printing based on input materials

All these AM techniques apply a similar working principle in which the object is built by adding material layer by layer. The main differences between the AM processes are the deposition methods and the materials used. Out of AM techniques, fused filament fabrication or fused deposition modelling is widely adopted for thermoplastic polymers. Thi is due to its simplicity, relatively low cost, low material waste and reduced risk of material contamination or degradation.

2.3 Hip Implant

A hip implant is used to replace a damaged or broken hip joint in order to relieve pain and restore joint function in the human body (Oshkour, Osman, Bayat, Afshar, & Berto, 2014). According to Palaniappan *et al.* (Palaniappan et al., 2020), hip surgery is becoming more regular in younger and elderly people, necessitating the need to improve implant production and survival rate. Hip implants are expected to last at least 15 years; however, due to a variety of issues, they tend to have a short lifespan and require surgical reviews (Aherwar, K Singh, & Patnaik, 2015). One of the most common reasons for surgical review is aseptic loosening caused by stress shielding (Bougherara, Bureau, Campbell, Vadean, & Yahia, 2007). Stress shielding is the

bone loss phenomenon at implant and bone interfaces (Arabnejad, Johnston, Tanzer, & Pasini, 2017). Studies have repeatedly confirmed that the mismatch between the high stiffness implant materials and low stiffness femur bone can cause stress shielding causing bone loss and finally aseptic loosening of the implant (Arabnejad et al., 2017; Limmahakhun, 2017). This complication experiences pain and instability of the implant. Figure 2.9 shows the aseptic loosening of metal implant with the loosening width greater than 2 mm at the bone–implant interface, which is a sign of the implant failure (Apostu, Lucaciu, Berce, Lucaciu, & Cosma, 2018).

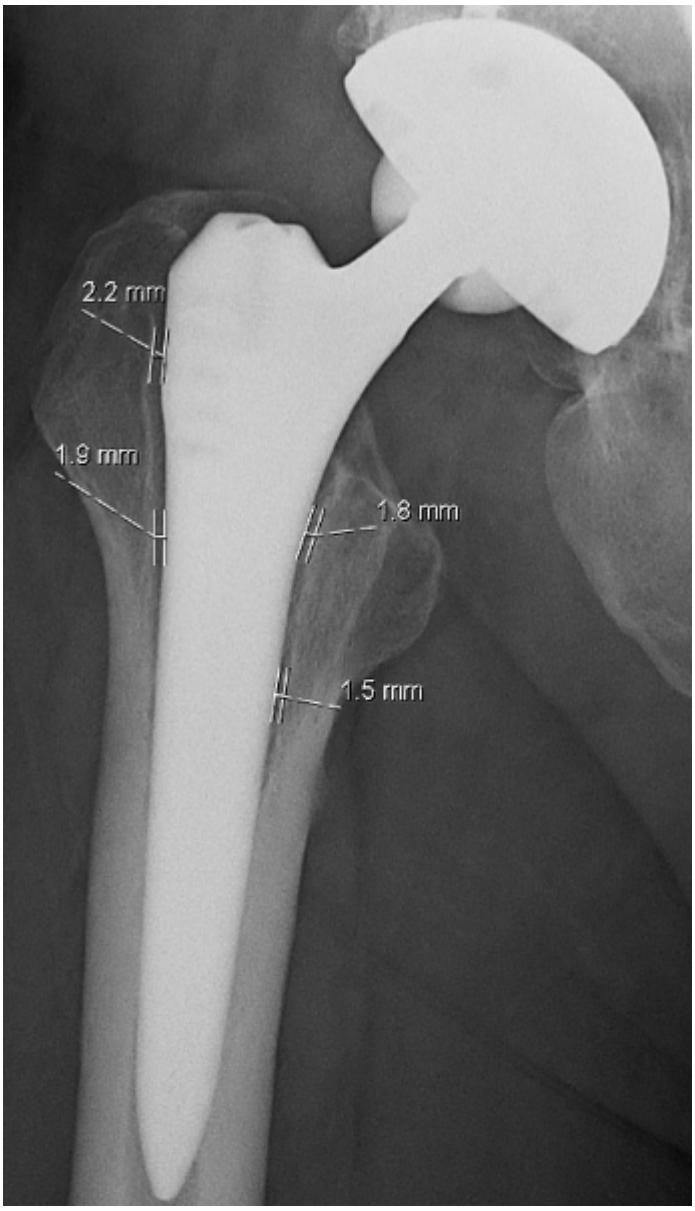

Figure 2.9: X-ray image of bone resorption

To improve oseointegration, research have been suggested to select porous implants with pore size of approximately 600 μm for titanium material (Apostu et al., 2018). Aseptic loosening is also caused by osteolysis of wear debris at the articular joint and micromotions at the bone-implant contact (Bougherara et al., 2010). The wear particles cause macrophages to secrete pro-inflammatory cytokines, osteoblasts

and fibroblasts to produce proresorptive cytokines. Also, osteoclastogenesis to be stimulated, and osteolysis to occur which then increase over time, resulting in implant loosening (Cordova et al., 2014). The source of wear particles can be either metals or polymers (Palaniappan et al., 2020).

2.4 Medical Implant Materials

2.4.1 Introduction

Any material used in developing a hip prosthesis must be compatible with the host environment within the human body. Such compatible materials are known as biomaterials. The human body is well-designed to protect itself from external objects and is aggressive in doing so. As a result, only highly inert materials are appropriate for implants as they are chemically and physiologically safe and will not decompose. Nevertheless, most materials used are not entirely inert to serve as hip implant replacements (Prasad et al., 2017).

2.4.2 Biometals

Metallic implants for treating and replacing bone fractures have been selected based on their material properties (Ibrahim, Sarhan, Yusuf, & Hamdi, 2017). Stainless steel (SUS 316L), cobalt-chromium (CoCr) alloys, Titanium (Ti), and Ti alloys are the most commonly used biomaterials (Kamachi Mudali, Sridhar, & Baldev, 2003). These bimetals have superior mechanical and good biocompatibility properties (Kamachi Mudali et al., 2003). When metals and alloys are considered, susceptibility of the material to corrosion and the effect of corrosion on the tissue are critical aspects of biocompatibility (Kamachi Mudali et al., 2003).

2.4.2.1 Stainless Steel

Before the introduction of stainless steel in the biomedical industry, implants were fabricated from pure metals, which often showed low corrosion resistance and poor mechanical strength (Ansari, Ali, & Rana, 2015). The problem was addressed by introducing an alloy of stainless steel (SUS 316L) (Taqriban, Ismail, Jamari, & Bayuseno, 2021). This alloy contains 18wt% Cr and 8wt% Ni, making it stronger and more resistant to corrosion (Walczak, Shahgaldi, & Heatley, 1998). The addition of molybdenum, as well as the reduction of carbon from 0.08 to 0.03 wt% also improved its corrosion resistance (Walczak et al., 1998). There is however fear that Stainless Steel SUS 316L may corrode inside the body under a high- stressed oxygen-depleted environment (Manivasagam, Dhinasekaran, & Rajamanickam, 2010).

2.4.2.2 Cobalt Chromium

Cobalt-chromium (CoCr) material consists of chromium, cobalt, and other metals such as molybdenum and nickel. It is an alloy with high strength, wear, and corrosion resistance, making it biocompatible. Cobalt–chromium alloys have been used as orthopedic implant materials (Ogawa, Tohma, Ohgushi, Takakura, & Tanaka, 2012). Research has found that these alloys have good corrosion resistance, but have low ductility that requires improvement Shi, Northwood, and Cao (1994).

2.4.2.3 Titanium Alloys

Titanium has also been used for medical implants. One of the major advantages of titanium is its high strength-to- weight ratio. Increased use of titanium and its alloys as biomaterials comes from their superior biocompatibility and excellent corrosion resistance compared to stainless steel and cobalt-chromium; because of the thin surface oxide layer (Semlitsch, 1987). They have good mechanical properties, including elastic modulus and low density (Semlitsch, 1987).

Senalp *et al.* (Senalp, Kayabasi, & Kurtaran, 2007) compared the performance of the hip joint made of Ti–6Al–4V and cobalt–chromium metal materials. The results showed that the best stem shape for fatigue under static loading was made of Ti–6Al–4V material.

However, a critical problem associated with Ti alloys is stress shielding that occurs at the contact of Ti and bone during load transfer which results in loss of the surrounding bone (Bougherara et al., 2007). This stress shielding problems of an implant can be avoided by replacing high stiff metallic materials with low stiff materials (Bougherara et al., 2007). Because of the problems observed in biometals, biopolymers have been recently explored as alternative materials for bone replacement (Han et al., 2019).

2.4.3 Biopolymers

Biopolymers have found a wide range of applications, especially in medical fields (Rebelo, Fernandes, & Fangueiro, 2017). Biocompatibility, biodegradability, and non-cytotoxicity have made these materials promising candidates for medical implant materials (Díez-Pascual, 2019; Rebelo et al., 2017). Biopolymers with high stiffness and strength are used for orthopaedic surgery. In orthopaedic applications, common polymers used are polyethylene (PE), polyurethane (PU), polypropylene (PP), polyethylene terephthalate (PET), polyvinyl chloride (PVC), polyethylene glycol (PEG), polycaprolactone (PCL), polylactic acid (PLA), polytetrafloroethylene (PTFE), polymethyl methacrylate (PMMA), ultra-high molecular weight polyethylene (UHMWPE), PEEK, and nylon (Nag & Banerjee, 2012). Many of these materials are used for implants with low or non load bearing applications due to their low mechanical properties to support or subject to high mechanical loads (Ghalme, Mankar, & Bhalerao, 2016). Compared to high load-bearing implants, the low load implant materials have less strength and modulus of elasticity but good ductility.

Among these biopolymers, UHMWPE, PE, PCL, and PLA have been explored for hip joint implants due to their high mechanical performances (Garcia-Gonzalez et al., 2017).

Chethan *et al* (Chethan, Shyamasunder Bhat, Zuber, & Satish Shenoy, 2019) carried out finite element analysis of different hip implant designs along with femurs under compressive loading conditions using UHMWPE material. The results showed that all considered hip implant designs had exhibited the von Mises stresses less than its yielded strength. This indicated that hip implants designed using UHMWPE material were safe against failure under compressive loadings. However, fatigue analysis for UHMWPE hip implant was limited.

Zameer and Haneef (Zameer & Haneef, 2015) used UHMWPE composite to estimate the artificial hip joint failure. The results of compressive loading analysis showed that the maximum stresses were concentrated on the neck of the hip joint compared to the bottom of the femur. The stress distribution derived from compressive analysis results were within permissible limits (less than material yield strength).

Palaniappan *et al.* (Palaniappan et al., 2020) compared the performance of compared the performance of UHMWPE, PLA and PU for hip joint implant. The ANSYS results showed that PU and PLA had high wear resistance properties compared with UHWMPE. The wear resistance of PU and PLA made them suitable for the internal component materials. However, they were not desirable for high loading applications due to their low mechanical properties. Wear from UHMWPE is a worry because the wear particles can trigger a biological response, resulting in bone resorption, aseptic loosening, and implant failure (Pietrzak, 2019).

These unreinforced polymers have poor mechanical properties such as low stiffness and high ductility. Therefore, the materials are undesirable for high loading applications (Rahim et al., 2017). Corrosion resistance, reliable mechanical

properties, and sound processing characteristics of thermoplastic polymer composites have made them viable alternatives to metallic materials and unreinforced polymers with a broader range of bone-matching properties. Carbon fiber reinforced polymer composites are made up polymer matrix and carbon fiber reinforcements (Ozkan, Gok, & Karaoglanli, 2020). The polymer acts as a matrix, holding and protecting the fibers, and also transferring the load to reinforcement. Carbon fibers support the load by giving excellent strength and high stiffness to the material (Ozkan et al., 2020).

Recent manufacturing advancements have enabled the production of fatigue-resistant carbon fiber nylon 12 (CF/PA12) composites for implants with stiffness characteristics similar to the human femur (7-20 GPa) (Dimitrievska et al., 2009). Biocompatibility of this material has been demonstrated in the laboratory for hip joint replacement Aherwar et al. (2015). It was confirmed that CF/PA12 composite is a more suitable material for the hip implant than metals (Dimitrievska et al., 2009).

Several studies have been carried out to evaluate the performance of CF/PA12 total hip prostheses. Campbell *et al.* (Campbell et al., 2008) manufactured CF/ PA12 prosthesis by injection molding. The compressive strength and modulus of CF/PA12 composite polymer were investigated. Molded CF/PA12 composite strength performance was found to match the cortical bone of the femur. The results also showed that the molded CF/PA12 had excellent fatigue resistance, making it a new candidate material for complete hip prostheses.

Bougherara *et al.* (Bougherara et al., 2010) conducted a comparative study of CF/PA12 and Titanium hip stems by predicting the bone density redistributions in the femoral bone before and after complete hip replacement using the finite element method. Numerical simulations of bone remodeling revealed that the CF/PA12 composite stem creates a superior bone density pattern than the Ti-based

stem, indicating the composite stem's efficiency in minimizing stress-induced bone resorption.

Avval *et al.* (Tavakkoli Avval, Samiezadeh, Klika, & Bougherara, 2015) considered the coupling effect between mechanical loading and bone biochemistry to predict long-term bone density distribution around the CF/PA12 total hip arthroplasty stem. The results were then compared to those obtained in femurs implanted with titanium alloy and cobalt–chrome–molybdenum implants. The CF/PA12 hip implant was superior to metallic hip implants in terms of providing a more uniform density across the bone and causing less stress shielding, resulting in reduced post-operative bone loss.

To further demonstrate the capability of CF/PA12 as a promising material for hip joints, Chergui *et al.* (Chergui, Ameddah, & Mazouz, 2018) used the finite element approach to evaluate the failure of a CF/PA12 hip implant under compressive and dynamic loadings. The results showed that a hip resurfacing prosthesis comprising entirely of CF/PA12 composite was resistant to fatigue failure. The highest stresses obtained were; 10.63 MPa and 37.08 MPa under compressive and dynamic loadings, respectively. These stress results were lower than the material yield stress of 63.4 MPa, indicating that the CF/PA12 composite hip resurfacing prosthesis was safe against failure.

The finite element method has also been applied to analyze and compare the biomechanical performances of a hybrid CF/PA12 composite-metal resurfacing implant and the conventional metallic hip resurfacing implants (Bougherara & Bureau, 2008). Compared to conventional metallic hip resurfacing implants, the hybrid composite metal hip resurfacing showed the ability to reduce stress shielding, conserve bone stock, and prevent bone fracture.

Since the hip implant acts as a substitute for the femur, it should have similar

mechanical properties to that of the femur. The mechanical properties of the femur are shown in Table 2.1.

Table 2.1: General mechanical characteristics of different materials and living tissues (Campbell et al., 2008; Ghalme et al., 2016; C. Liao & Li, 2020)

Material Or Tissue	Density (g/cm^3)	Modulus (GPa)	Ultimate Strength (MPa)	Poisson's ratio
Cancellous bone	0.03–0.12	0.04–1.0	1.0–7.0	0.01–0.35
Cortical bone	1.6–2.0	7–20	50- 150	0.28–0.45
Titanium alloys	4.4–4.7	105	780–1050	0.33
Stainless steel alloys	7.9	210	230–1150	0.27–0.30

From the Table 2.1, it is noted that, Titanium and stainless steel have higher density compared with that of cortical bone. The densities of the implant material and host tissue (cortical bone) should almost be similar for better osseointegration. As the bone becomes less dense, the hip implant begins to experience micromotion, which grows over time and causes implant loosening.

2.5 Effect of FFF Process Parameters

Many industrial techniques have and still continue to use traditional manufacturing methods to produce polymer products (Wickramasinghe et al., 2020). Compared to traditional manufacturing, additive manufacturing techniques such as SLS and FFF have shown an innovative way to simplify processing of high performance polymers (Wickramasinghe et al., 2020). In order to reshape the polymers, FFF has been reported to undergo different settings of variables, including layer thickness, print speed, raster angle, and printing temperature (Katschnig & Holzer, 2018). Recent research has focused on the process parameters since they negatively impact the mechanical properties, dimensional accuracy, and surface finish of components made using the FFF technique (Rarani, Ezati, Sadeghi, & Badrossamay, 2020).

Ning *et al.* (Ning, Cong, Hu, & Wang, 2017) investigated the impact of raster angle, infill speed, nozzle temperature, and layer thickness on the tensile properties of FFF manufactured carbon fiber composite parts. The results suggested that the optimal parameters to increase tensile strength, the Young's modulus, and yield strength were raster angle of 0°/90°, infill speed of 25 mm/s, nozzle temperature of 220°C, and layer thickness of 0.15 mm. In addition, a layer thickness of 0.25 mm showed high toughness and ductility of the manufactured parts. The part's strength, Young's modulus and stiffness were affected by the filling technique because of the degree of bonding between layers. The stronger interbonding between the adjacent layers resulted in high mechanical properties. The optimal settings obtained were only restricted to CF/ABS products.

Wu *et al.* (W. Wu et al., 2015) investigated the influence of layer thickness and raster angle on the mechanical properties of 3D printed parts. Parts were printed at three different levels of layer height (200, 300, and 400 μm) and three levels of raster angles (0°/90°, 30°/-60°, and 45°/-45°). According to the research, layer height was more significant than raster angle. The optimal mechanical properties were obtained at a layer thickness of 300 μm and a raster angle of 0°/90°. This was probably caused by the reasonable nozzle temperature that significantly improved bonding between the raster and layers, leading to stronger fusion. However, the interaction effects between these parameters were not considered.

Deng *et al.* (Deng et al., 2018) studied the optimization of mechanical properties for PEEK via fused filament fabrication. The influences of three different printing temperatures (350, 360, and 370 °C) and layer thicknesses (0.20, 0.25, and 0.30 mm) as well as printing speeds (20, 40, and 60 mm/s) were investigated. They deduced that printing temperature, layer thickness, and printing speed influence tensile properties. The optimal process parameter combination for the tensile strength was; a printing speed of 60 mm/s, a layer thickness of 0.25 mm, and a printing temperature of 370°C. The optimal combination for the percentage elongation was;

a printing speed of 60 mm/s, a layer thickness of 0.2 mm, and a printing temperature of 360°C.

Build orientation has been seen to significanty affect the mechanical properties of the printed part, especially the tensile strength and ductility (Qamar Tanveer, Mishra, Mishra, & Sharma, 2022). Figure 2.10 (Caminero et al., 2019) shows the different build orientations that impact mechanical properties during the FDM process. The parts printed on-edge show the highest tensile strength, followed by the flat print orientation. The parts printed in upright orientation to the printing direction are significantly weaker (Caminero et al., 2019).

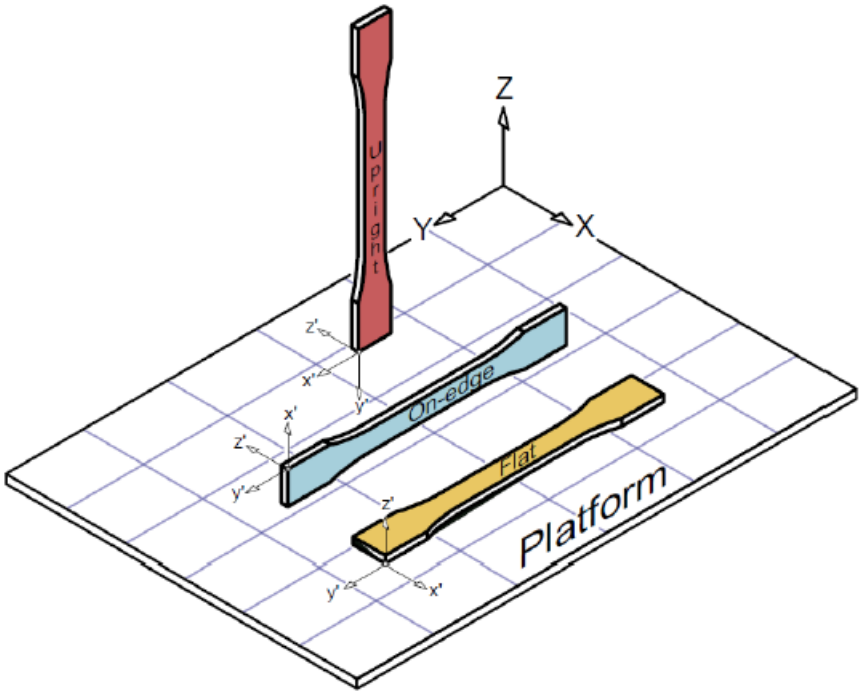

Figure 2.10: Build orientations during FFF process

Another factor that contributes a significant role to the mechanical properties of the printed material is the infill density which refers to the amount of material printed inside the object. Infill density in FFF should be appropriately selected to achieve the best properties of the part. If an object is printed with 100 % infill, it will

be entirely solid inside. The higher the infill percentage, the heavier and stronger the object becomes; however, the filament takes more time to print. Alvarez *et al.* (Alvarez C., Lagos C., & Aizpun, 2016) showed that 100 % infill resulted in higher tensile strength. A high-density setting gives a higher resistance to failure resulting in higher loading levels and an increase in hardness, yield, and fracture strength.

Toro *et al.* (Verdejo et al., 2019) investigated the influence of infill density, layer thickness and infill pattern on the flexural and bending strengths of 3D printed CF/PA12. The best results were obtained at 0.4 mm nozzle diameter, 0.2 mm layer height, concentric pattern, and an infill density of 100 %.

Alani *et al.* (Fadhil Alani, Basil Ali, Fadhil Abbas, & Mohammad Othman, 2018) noted that a layer thickness of 0.3 mm resulted in higher tensile strength. A layer thickness of 0.1 mm led to many layers, resulting in a high temperature gradient of the printed part. The larger number of layers increased the strength by increasing the fusion between the successive layers. This, however, also decreased the strength since the increased temperature gradient causing distortion of the printed part. This is a fact that a high number of layers increase the number of heating and cooling cycles subjected to the printed part. Hence causing residual stresses within the part. Alani *et al.* (Fadhil Alani et al., 2018) reported that increasing the layer thickness from 0.1 mm to 0.3 mm improves the mechanical properties. However, the time required to print the sample decreased with an increased layer thickness.

Printing speed is another process parameter that affected the printed parts' surface finish and mechanical properties (Ouhsti, Haddadi, Mellal, & Belhouideg, 2018). A high-speed causes poor surface finish, causing defect formation within surface. A low-speed setting results in better mechanical properties and minimal defects on the surface of the FFF fabricated parts (Ouhsti et al., 2018).

Raster angle has been observed to affect the mechanical properties of the printed

parts. Ezoji *et al.* (Ezoji, Razavi-nouri, & Rezadoust, 2016) showed that the tensile strength of the fabricated parts decreased with an increase in the raster angle. The parts printed at 0°/90° showed the highest tensile strength compared to 45°/-45°and 30°/60°. This was due to the alignment of polymer molecules along 0° and 90° direction of deposition that resulted in better coalescence between consecutive filaments.

Figure 2.11 shows SEM micrographs of tensile specimen fracture interfaces with five raster orientations (Ziemian, Sharma, & Ziemi, 2012). From the Figure 2.11 (a, b, and d), the specimens ruptured along the layers and formed smooth fractured surfaces, indicating that the raster angles of 0°, 30°, and 60° do not allow the material to resist the tensile load. The specimens failed due to poor interfacial adhesion between the layers. However, the specimens made with the raster angles of 45° and 90° had rough fractured surfaces, as shown in Figure 2.11 (c) and (e). These specimens were due to material failing during tensile loading, resulting in higher tensile strength (Ziemian et al., 2012) .

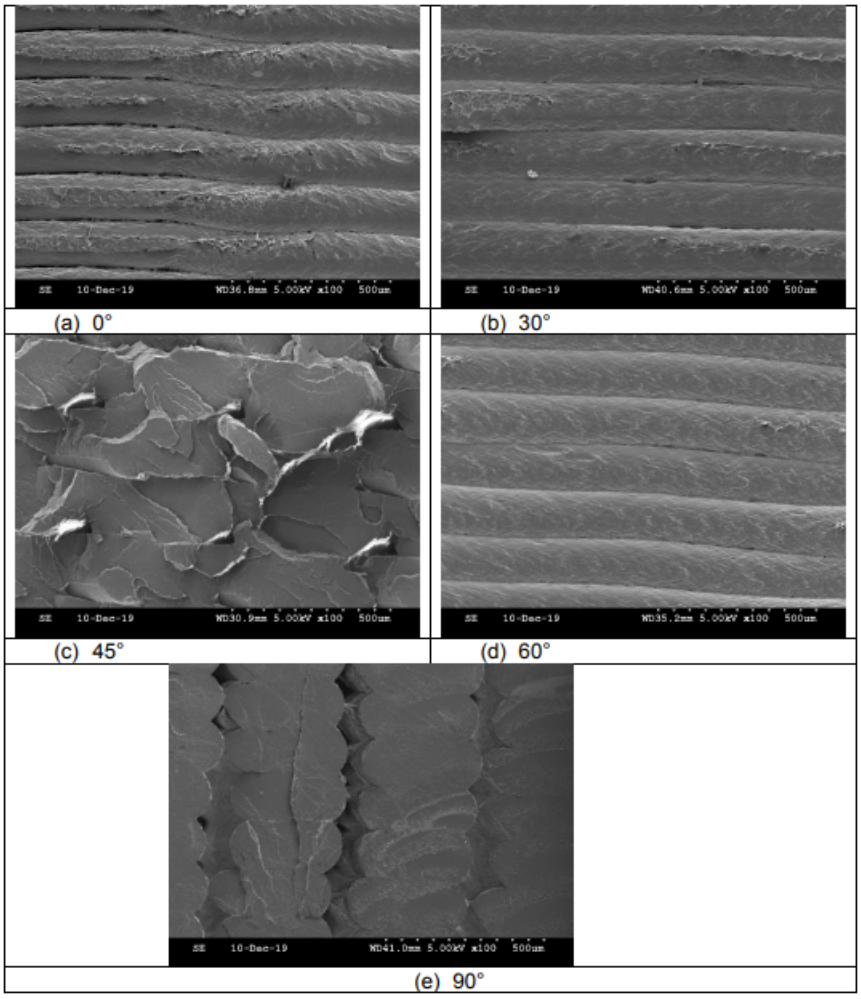

Figure 2.11: SEM micrographs of tensile specimen fracture interfaces with five raster orientations

Tensile strength has been affected by nozzle temperature due to the formation of bonds between extruded filaments. Zekavat et al. (Zekavat, Jansson, Larsson, & Pejryd, 2019) investigated the effect of nozzle temperatures ranging from 180 to 260°C for PLA parts, and the results showed that the specimen printed at lower temperatures of ($\leq$ 220°C) had relatively lower tensile strengths. The specimen printed at higher temperature depicted higher tensile strength because of the excellent bond between the extruded filaments.

Most of the researchers concentrated on the two most common materials in FFF

which are PLA and ABS. For instance, Corapi *et al.* (Corapi, Morettini, Pascoletti, & Zitelli, 2019) used PLA material to investigate the mechanical strength and percentage elongation of FFF parts. Christiyan et al. (Christiyan et al., 2016) studied the influence of layer thickness and print speed on mechanical properties, including tensile and flexural strengths of ABS parts. The results showed that low printing speed, and low layer thickness resulted in high tensile and flexural strengths.

Attoye *et al.* (Attoye, Malekipour, & El-Mounayri, 2019) investigated the effect of several process parameters, including nozzle temperature, printing speed, and print orientation on Young's modulus, yield strength, and ultimate strength of the final part for PLA and ABS. The results revealed that the mechanical properties of PLA were better than those of ABS. The results also concluded that the parts printed in the Y-axis orientation presented the best mechanical properties in PLA, whilethe X-axis orientation is the best orientation for printing parts with ABS.

Rajpurohit and Dave (Rajpurohit & Dave, 2018) studied the impact of raster angle, layer height, and raster width on the tensile strength of PLA. The highest tensile strength was obtained at a raster angle of 0° and low value of layer height. Mohamed *et al.* (O. A. Mohamed, Masood, Bhowmik, Nikzad, & Azadmanjiri, 2016) used ABS to study the impact of six FFF process parameters: layer thickness, air gap, raster angle, build orientation, road width (diameter of the extrusion nozzle), and the number of contours on the dynamic mechanical properties (storage modulus, loss modulus and mechanical damping) of the FFF parts. The analysis of variance (ANOVA) results showed that layer thickness, air gap, and number of contours have the largest impact on dynamic mechanical properties. The optimal parameters for maximum dynamic mechanical properties were found; layer thickness of 0.330 mm, air gap of 0.0 mm, raster angle of 0.0°, build orientation of 0.0°, road width of 0.457 mm, and 10 contours.

Kovan *et al.* (Kovan, Tezel, Camurlu, & Topal, 2018) investigated the impact of layer

thickness and printing orientation angles on the modulus of elasticity and tensile strength of the 3D printed CF/PLA. The results showed that the optimum process parameter levels for highest tensile strength and modulus of elasticity were; a printing orientation of 90° and a layer thickness of 0.4 mm.

2.6 Summary of FFF Process Parameters

High product quality can be achieved by selecting a layer thickness in the range of 0.1 to 0.3 mm because it increases part strength and reduces the surface roughness of the printed parts. Besides layer thickness, optimum values of print speed, raster angle, build orientation, and printing temperature are essential to achieve superior mechanical properties. Most of the research carried out so far has focused on a few materials like ABS, PLA, and PEEK. However, according to the literature, the influence of parameters differs depending on the material utilized. Investigating novel materials could help overcome the FFF technique's material constraint. As a result, further research into the impact of parameters on potential materials is required. There is also limited literature on using the finite element method to assess the effect of FFF process parameters for printing of CF/PA12 for medical implants. Carbon fiber-reinforced polyamide 12 is a recently developed composite material for medical implants with excellent biocompatibility, low cost, and reasonably good mechanical properties.

2.7 Optimization of Process Parameters

Researchers have attempted to improve the quality of fused deposition modelled parts by optimizing the process parameters. The optimization methods include Taguchi method (Nancharaiah, 2011), I-optimality criterion (O. A. Mohamed, Masood, & Bhowmik, 2016c), fuzzy logic (Padhi et al., 2017), response surface methodology (Kasim, Harun, Hafiz, Mohamed, & Mohamad, 2019), artificial neural network

(Yadav, Chhabra, Kumar Garg, Ahlawat, & Phogat, 2020), and genetic algorithm (Fountas & Vaxevanidis, 2021). This section discusses the various optimization methods that have been used for the optimization of FFF process parameters.

Nancharaiah (Nancharaiah, 2011) studied layer thickness, air gap and raster angle optimization on build time using the Taguchi method. The results showed that layer thickness and air gap largely influence the build time. The effect of raster angle, the interaction between layer thickness and raster angle, air gap and raster angle on build time were insignificant. With ANOVA, it was found that the contributions of layer thickness and air gap on build time were 66.57 % and 30.77 %, respectively. Based on signal to noise (S/N) ratio, the optimum parameters for processing time were: 0.33 mm layer thickness, 0.02 mm air gap, and 45°/-45° raster angle. However, build time was not major output performance for the process optimization.

Mohamed *et al.* (O. A. Mohamed, Masood, & Bhowmik, 2016c) studied the effect of five process parameters for dimensional accuracy using the I-optimality criterion. The results showed that the best parameter settings for dimensional accuracy were: layer thickness of 0.127 mm; air gap of 0.342 mm; raster angle of 88.918°; build orientation of 89.122°; road width of 0.462 mm, and one contour. The mathematical model was developed to restrict the relationship between input parameters and dimensional accuracy of parts manufactured with ABS. However, evaluation of the mechanical integrity is limited.

Padhi *et al.* (Padhi et al., 2017) optimized FDM process parameters for dimensional accuracy using fuzzy logic and the Taguchi method. The optimum process parameters for minimum changes in length, width, and thickness were layer thickness of 0.178 mm, orientation of 0°, raster angle of 0°/90°, raster width of 0.456 mm, and air gap of 0.008 mm.

Kasim *et al.* (Kasim et al., 2019) optimized the process parameters for dimensional

accuracy and surface roughness using a response surface methodology. The results showed that the optimum parameters that minimized both responses were layer thickness of 0.18 mm, and part angle of 67.38°.

Yadav *et al.* (Yadav et al., 2020) optimized extrusion temperature and infill densities using the artificial neural network method for tensile strength. The analysis showed that the tensile strength was affected by nozzle temperature and infill density. Nozzle temperature was more significant for tensile strength than infill density; high nozzle temperature increased the tensile strength of the printed parts. The optimum levels for tensile strength were: extrusion temperature of 225°C and infill density of 40 %. However, this results can be used for light weight structures since highest tensile strength is achieved at 100 % infill density. This work was limited to two parameters, which were not enough to determine the strength of the product.

Srivastava and Rathee (Srivastava & Rathee, 2018) used the Taguchi method to optimize of layer height, contour width, raster width, and air gap on build material volume. The results showed that the optimum parameter settings for build volume were: 0.177 mm layer thickness, -0.1 mm overlap, 0.64 mm contour width and 0.56 mm raster width.

These techniques are all suitable for the optimization of FFF process parameter levels. However, Taguchi is the most preferred method due to its capability to conduct experiments with the fewest possible trials at minimum cost (Alafaghani & Qattawi, 2018; Aslani, Chaidas, Kechagias, Kyratsis, & Salonitis, 2020). The Taguchi method is based on the reduction of variability in the outputs compared with other techniques which are based on averaging resultants (Rarani et al., 2020; Wankhede, Jagetiya, Joshi, & Chaudhari, 2020).

2.8 Residual Stresses in FFF Parts

In the FFF process, the material is first molten above its melting temperature and then extruded through the nozzle moving on a build platform. When the first layer of the part is deposited on the substrate, convective heat exchange is developed between the first layer and the surroundings, whereas conductive heat exchange is achieved between the layer and the substrate. Conduction and convection are the most prominent heat transfer modes and result in the change in the geometrical model (Costa, Duarte, & Covas, 2014). The heating and successful cooling processes cause the semi-molten filament becoming solidified, and these processes are characterized by non-uniform thermal gradients, which cause residual stresses in the printed part (Ferreira & Quelho de Macedo, 2017).

Residual stresses that occur within the part can be classified according to the type of manufacturing process used (Mukherjee, Zhang, & DebRoy, 2017b). These stresses are classified as: chemical and thermal stresses (Zaroog, Yap, Ken, Noorlina, & Manap, 2014).

Mechanical residual stresses result from the manufacturing processes that generate non-uniform plastic deformation. These stresses are induced in the part produced by the material forming processes, including forging, rolling, bending, extrusion, and drawing.

Chemical residual stresses occur due to the material phase transformation and precipitation processes (Zaroog et al., 2014). Examples of such residual stresses include the stresses that accumulate during the chemical surface treatments, coatings, precipitation hardening in alloys, and polymerization in plastics.

Thermal residual stresses are generated in the parts due to the non-uniform heating or cooling operations. Effects of the residual stresses within the part can either

be beneficial or harmful depending on the stress distribution in relation to the component and whether the stresses are compressive or tensile (Da Silva et al., 2016). For instance, tensile residual stresses tend to promote the initiation and growth of cracks in fatigue failure processes while compressive residual stresses tend to delay the fatigue crack initiation and growth, resulting in prolonged fatigue life (Madireddy, Li, Liu, & Sealy, 2019). Surface tensile residual stresses are undesirable due to their negative impact on the part's mechanical properties (Saphronov, Khmyrov, & Gusarov, 2015). It has been reported residual stresses are detrimental and can contribute to the failure of the manufactured part because they promote cracking (Saphronov et al., 2015). They may increase the damage rate during fatigue and creep degradation. They may also reduce the resistance to loads by contributing to the failure by brittle fracture or cause other forms of damage such as shape change or crack propagation on the surface of the part (Xing, Ouyang, Li, & Liu, 2018).

During fused filament fabrication, the interlayer filament bonding is obtained by reheating the previously deposited layer, causing thermal variation (Y. Zhang & Chou, 2006b). Hence, producing thermal residual stresses between the layers, which cause warping and part distortion (Y. Zhang & Chou, 2006b).

Researchers have studied the influence of FFF process parameters on the residual stresses. For instance, Bähr et al. (Bähr & Westkämper, 2018) investigated the effect of layer deposition on the residual stress within the printed parts. The experimental results showed that by building up a part in layers, thermal energy was supplied from the top surface. The earlier printed layers had already cooled down through conduction and convection. A non-uniform thermal gradient creates residual stresses within the part. The shrinking of the last printed layer results in the development of tensile stresses transmitted within the component causing warping. It has been shown that $0°/90°$ raster angles relieve residual stresses in the printed parts, while 80 mm/s printing speed increases the residual stresses (Casavola, Cazzato, Moramarco, & Pappalettera, 2017a). In addition, a high number of layers increases the number

of heating and cooling cycles resulting in the accumulation of the residual stresses within the 3D printed part (Bähr & Westkämper, 2018).

Zhang *et al.* (W. Zhang et al., 2019) studied the effect of printing speed and raster angle on residual stresses within the printed parts. The results showed that lower raster angles relieved the residual stresses in the printed parts, while higher printing speeds increased the residual stresses.

Kantaros and Karalekas (Kantaros & Karalekas, 2013) studied the residual strains in ABS parts fabricated by FDM using the fiber Bragg grating method. The results showed that the residual stresses and strains built up during the fabrication process. Their magnitudes are primarily influenced by the selected process parameters, such as the layer thickness and deposition orientation.

Casavola *et al.* (Casavola et al., 2017b) measured residual stresses in fused deposition modelled parts using the drilling method with electronic speckle pattern interferometry. The results confirmed that controlling residual stress in the manufactured part is advantageous in reducing warping effects and premature failure. Analysis of input FFF process revealed that appropriate settings of process parameters relieved accumulated residual stresses. Therefore, there is a correlation between input process parameters and residual stresses. A small variation in raster angle resulted in variation of the accumulated residual stresses. The best raster angle to minimize residual stresses in the printing parts was $0°/90°$. Variation in layer thickness also experienced to inversely introduce the accumulated residual stresses.

Motivated by the preceding literature, the influence of raster angle, print speed and layer thickness relieved residual stresses in the printed part. The proper settings of these parameters resulted in minimizing residual stresses. Therefore, causing high part strength and good dimensional accuracy.

2.9 Numerical Simulation of Fused Filament Fabrication

The aim of simulating the process parameters of the printed part is to predict the quality of the product before manufacturing the prototype part for experimental tests. In general, simulation of the FFF process parameters is necessary to predict the residual stresses, part distortion, and the mechanical properties of the final product, which are related to the thermal field evolution.

Studies have used FEM to simulate the FFF process parameters on filament deposition. For instance, Verma *et al.* (Verma, Vishnoi, Sukhotskiy, & Furlani, 2018) reported that the temperature of a single layer decreases faster once deposited on the substrate. For high printing speeds, the cooling rate of the deposition is low.

Xia *et al.* (H. Xia, Lu, Dabiri, & Tryggvason, 2018) used the finite element method to predict temperature evolution between two filaments deposited at different extrusion temperatures. Figure 2.12 shows the temperature distribution of the printed filaments (H. Xia et al., 2018). The temperature gradient illustrated that the bottom filament was reheated by the heat from the hot top filament and the reheated area was more prominent for the higher nozzle temperatures. Moreover, better bonding was achieved at high melting points. Therefore, the nozzle temperature affects the filament deposition since it provides bonding strength between layers. Inappropriate setting of nozzle temperature negatively impacts part quality.

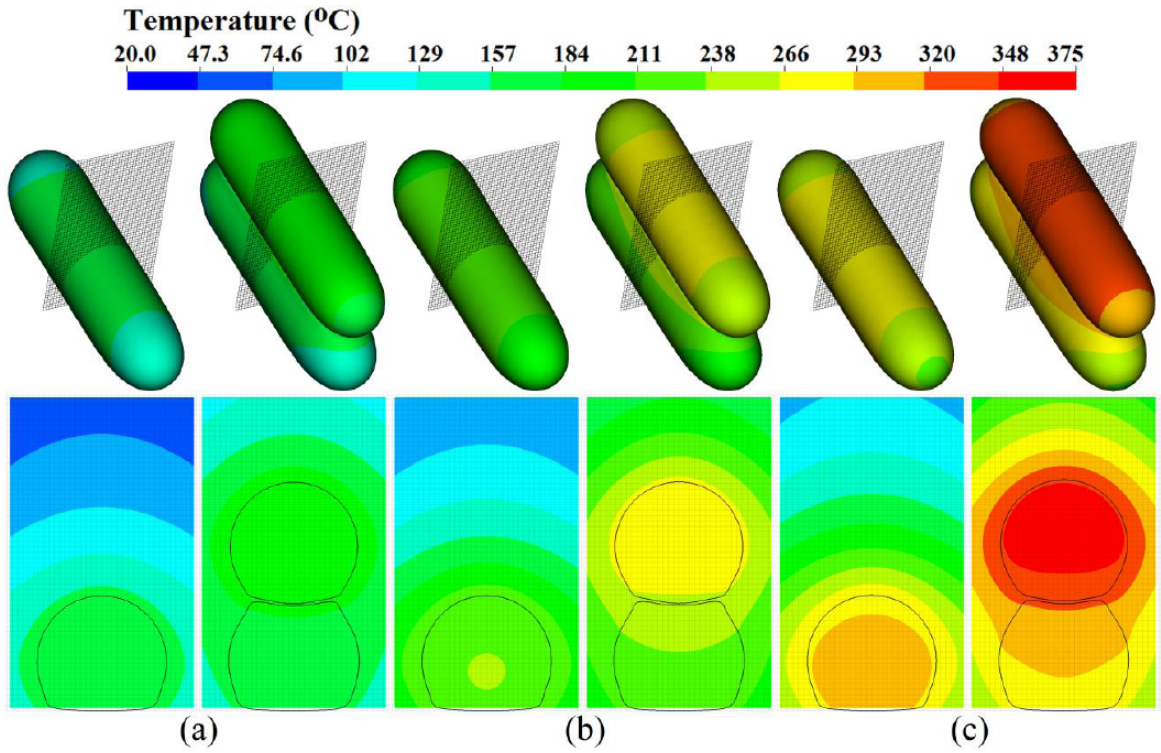

Figure 2.12: Temperature evolution between two filaments deposited at different nozzle temperatures

Zhang and Chou (Y. Zhang & Chou, 2006b) used finite element analysis to simulate the fused filament fabrication process parameters. They developed an FEA model using the element activation function to determine the stress distribution at different process parameter combinations and the effects of the tool path. The simulation results show that tool-path patterns had a significant effect on part deflection due to the residual stresses accumulated during deposition. Therefore, FFF parts were sensitive to tool-path patterns.

Nickel et al. (Nickel, Barnett, & Prinz, 2001) investigated the effect of deposition patterns on the resulting stresses and deflections. Finite element simulation of the deposition processes showed that the deposition pattern significantly affected the part stresses and deflections. A short rasters yielded low deflections, causing minimal residual stresses. However, a raster pattern of 90° yielded the lowest deflections

compared with short rasters.

Based on the above literature, FFF involves transient thermal analysis. This covers the cooling behavior caused by convective heat exchange with the environment and post-deposition contact with the platform. The boundary conditions are illustrated in Figure 2.13 (H. Xia et al., 2018). Therefore, the FFF computations are based on thermal transient governing equation which is presented in detail in the Methodology Section 3.2.7.

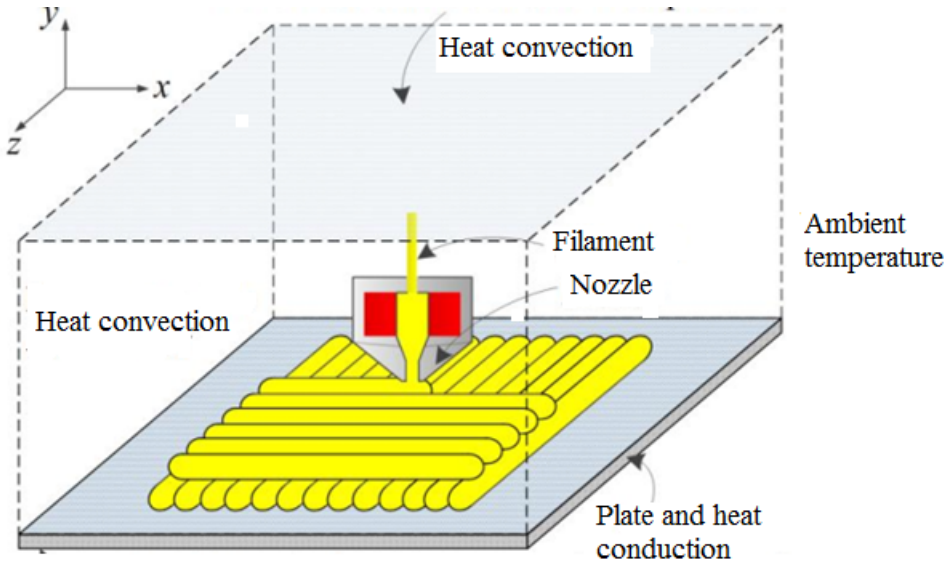

Figure 2.13: Transient thermal boundary conditions

2.10 Summary of Literature

The literature review has shown that metallic materials have reduced life span when used hip implants due to wear of the implants. Mismatch in stiffness between the metallic hip implants and the host tissue (femur bone) cause loosening of the implants. Carbon fiber nylon 12 composite was found to replace metallic materials for implants with stiffness characteristics similar to the human femur. Fused filament fabrication process parameters significantly affect the mechanical properties of 3D printed parts. Parameter have effect on the quality of the printed part. This

chapter has also presented the optimization methods of FFF process parameters. Research work on various optimization techniques indicated that the Taguchi method is the effective and efficient technique for industrial applications. This technique allows fewer experiments to be conducted with minimal number of trials. Residual stresses in the FFF parts is undesirable, they cause deformation resulting in poor mechanical properties. The literature showed that FFF process parameters including infill density, raster angle, infill pattern, deposition orientation printing temperature layer thickness, and print speed had an impact on the mechanical properties of the ABS and PLA parts. The printing temperature, layer thickness and print speed were found to be the major factors to negatively affect the printed part. There is adequate literature on the optimization of infill density, raster angle, infill pattern, and deposition orientation on the part quality of ABS and PLA parts. However, the overall combination of printing temperature, layer thickness and print speed on the mechanical properties of CF/PA12 is still unknown. This study considered the optimization of overall combination of printing temperature, layer thickness and print speed on mechanical properties of fabricated biocompatible CF/PA12 hip implant. Table 2.2 summarizes the previous works related to the CF/PA12 hip joint implant. The influence of FFF process parameters on the two common polymers are also shown in the Table 2.2.

Table 2.2: Summary of selected literature

Author	Research area	Benefits	Gaps
Campbell *et al.* (2008)	Manufactured hip implant using CF/PA12 composite material through injection molding and investigated its compressive strength	• The compressive strength of the molded CF/PA12 hip implant fell within the compressive strength range for the cortical bone of the femur.	• Tensile properties were not investigated • AM was not applied
Avval *et al.* (2015)	Predicted periprosthetic bone remodeling and contrasted with the presence of CF/PA12, CoCrMo, and Ti alloy	• The CF/PA12 composite stem produces a more uniform density change across the bone and causes less stress shielding.	• AM was not applied
Chergui *et al.* (2018)	Made a comparison between titanium alloy and CF/PA12 composite hip stems	• The femoral bone implanted with a composite structure could withstand more load than one implanted with Titanium	• AM was not applied
Toro *et al.* (2020)	Influence of layer height, infill density of the FFF process on the mechanical properties of a CF/PA12	• Optimal levels were: 0.2 mm layer height, the concentric pattern and the 100% infill density.	• No application • Only trial and error method was adopted
Ezoji 2017	Influence of raster angle on the tensile strength of fused deposition modelled PLA parts	• The highest tensile strength obtained at 0° and 90°	• Optimization approach was not considered
Alvarez *et al.* (2016)	Influence of infill percentage on the mechanical properties of fused deposition modelled ABS parts	• The results showed that 100% infill will result in higher tensile strength. A high density setting gives a higher resistance to failure	• Used trial and error method • Only infill density was investigated

From the literature review, the following gaps were identified:

1. From the literature, it is obvious that CF/PA12 has good characteristics for use in the production of hip implants. However, most studies have focused on the production of the CF/PA12 hip implant using traditional procedures like injection molding. However, there is scanty information on the production of CF/PA12 hip joint implant using 3D printing.

2. The influence of fused filament fabrication process parameters on part qualities has been explored using a trial and error method. This method is time

consuming and costly. The use of super processing computers equipped with FEA modules has opened a new era in manufacturing processes. However, there is limited study in the integration of finite element method in 3D printing to assess the effect of printing process parameters on printed part qualities.

3. Although the optimization of the most common polymers, like ABS and PLA has been carried out, there has been little research on optimizing of FFF process parameters for the manufacture CF/PA12 hip joint implants.

4. The mechanical performance of the 3D printed materials is crucial as they must meet the requirement for load-bearing applications. Research has been carried out to determine the quality of 3D printed for the most common materials with no directing industrial application. However, there is scanty information on predicting the performance of 3D printed CF/PA12 hip joint implants for medical application.

This research will address all the gaps mentioned above.

CHAPTER THREE

METHODOLOGY

This chapter introduces the material and methods used to achieve each specific objective. The design of experimental (DoE) method provided a suitable way to establish the relationship between FFF process parameters and the output characteristics of 3D printed parts. The experimental procedures and analysis techniques are also provided.

3.1 Validation

Validation was conducted as a pre-study for simulation tests, which form a major part of this study. It is through validation studies that the accuracy of the simulation findings were determined. This provided a basis for further simulations in this work. A similar approach was used in other researches (Kosaraju, Anne, & Popuri, 2013; Obiko, Mwema, & Bodunrin, 2021). Validation involved comparing simulation and experimental findings. Experimental results were obtained from literature in the work of Casavola *et al.* (Casavola et al., 2017b). These researchers studied a 3D printed rectangular body of length 80 mm, with 40 mm and height 7 mm. It was made of ABS plastic. The input parameters were as shown in Table 3.1. The experimental work gave a maximum residual stress of 6 MPa. To validate the experimental work by Casavola *et al.* (Casavola et al., 2017b), the geometry tested was designed using Solidworks 2018 and simulated using Digimat AM while employing the same input parameters. The geometry studied is shown in Figure 3.1. A mesh sensitivity study was conducted alongside validation study to determine the most suitable mesh size in terms of computational resources and accuracy of results. The mesh size was varied from 0.5 to 2 mm in increments of 0.5 as seen in another

study (Simiyu, Mutua, Muiruri, & Ikua, 2023). The respective number of elements, computation time and residual stresses were noted for comparison purposes.

Table 3.1: Preliminary process parameters

Factor	Level
Air gap (mm)	0
Layer thickness (mm)	0.2
Bead width (mm)	0.67
Number of contour lines	3
Bed temperature (°C)	90
Nozzle temperature(°C)	215
Infill orientation	30°/-30°

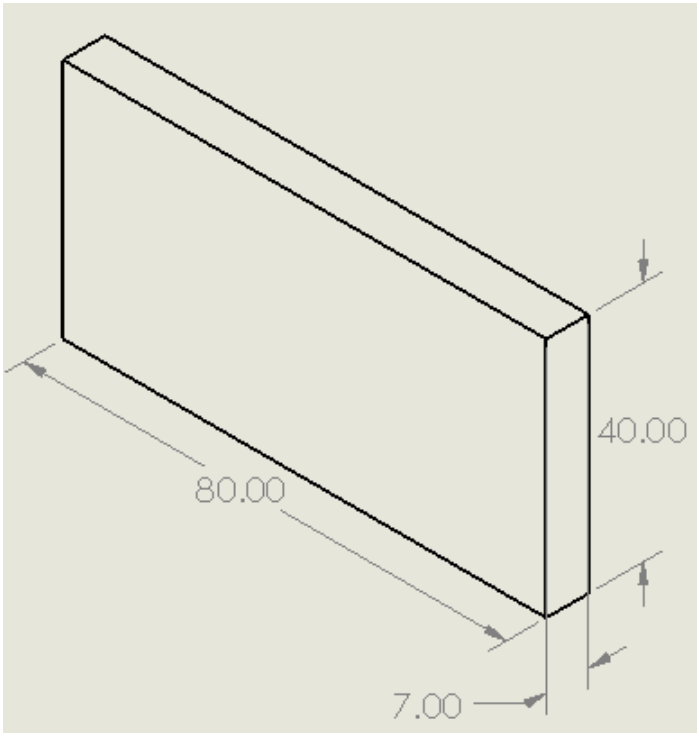

Figure 3.1: Rectangular model for validation

3.2 Methodology for Objective One

3.2.1 Material

The selection of the printing material is influenced by its characteristics that are appropriate for the intended application. Polymer composites were the first choice for better fit materials hip replacements. The most promising biocompatible polymer composites to replace metals for implants are carbon fiber/Ultra-high molecular weight polyethylene (CF/UHMWPE), CF/PEEK and CF/PA12 (Ghalme et al., 2016). They have high wear resistance and excellent mechanical properties (Ghalme et al., 2016). It is interesting to note that the CF/PA12 is the newest composite with relatively lower melting temperature than the other composites providing it a major advantage. Although CF/PA12 offers potential for a good tribological material, the performance abilities of this material after 3D printing is not yet established. This research evaluated the processability of CF/PA12 with FFF technique. Therefore, the material used in this study was carbon fiber nylon 12 filament with 1.75 mm of diameter produced by Fiberlogy, Poland. The content of fiber was 15 wt %, as it was previously proved by Jansson and Pejryd, and Liao et al (Jansson & Pejryd, 2015; G. Liao et al., 2017) that, the optimal amount of short carbon fibers added in the nylon 12 matrix was from 10 wt% to 20 wt%. This resulted in increasing the mechanical properties of the printed parts due to the better bonding between fibers and matrix (Wickramasinghe et al., 2020). However, fiber content above this amount led to severe porosities in the printed parts, resulting in poor mechanical strengths (Wickramasinghe et al., 2020). The carbon fibers in the nylon 12 matrix are illustrated in Figure 3.2. The PA12 with 15 wt % CF filament has recommended processing temperature of 255°C to 275°C (Fiberlogy, 2021).

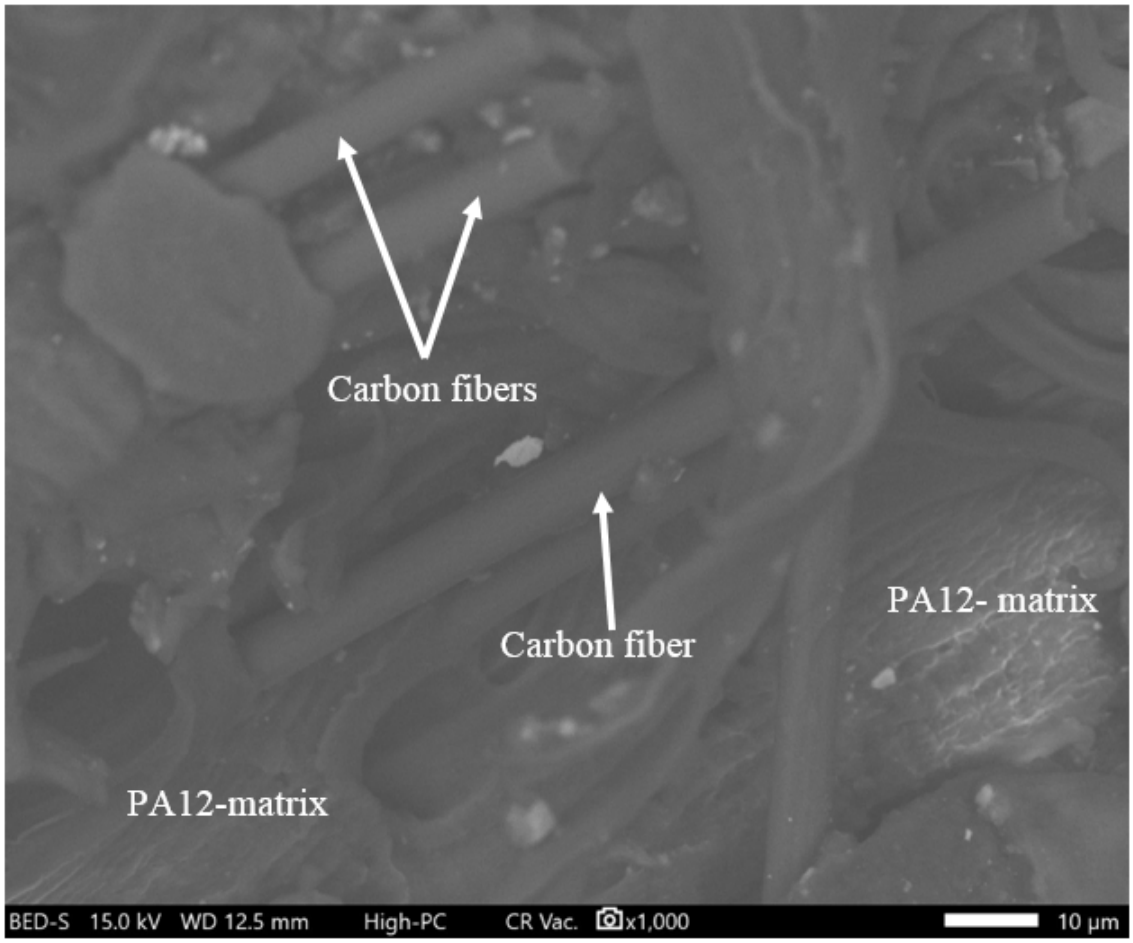

Figure 3.2: SEM image of 75 wt% nylon 12 with 15 wt% of carbon fibers

3.2.2 Geometric Model of Hip Joint Implant

As proposed in the literature that CF/PA12 composite is an appropriate material for hip implant, a 3D model of a hip joint implant was created for use in the FFF process, as shown in Figure 3.3. The 3D model was built based on measurements reported in the literature (Chethan et al., 2019; P. Kumar, Ahuja, & Singh, 2016) and confirmed by direct measurements of an actual/ full scale hip joint in the human anatomy department laboratory at Jomo Kenyatta University of Agriculture and Technology (JKUAT). Solidworks was used to create this model and saved as a standard tessellated language (.stl) file. The .stl file was used by Ultimaker Cura

4.8.0 printing control software for the pre-processing of the CAD model in order to properly prepare the geometry by generating the G-code file in readiness for the manufacturing process.

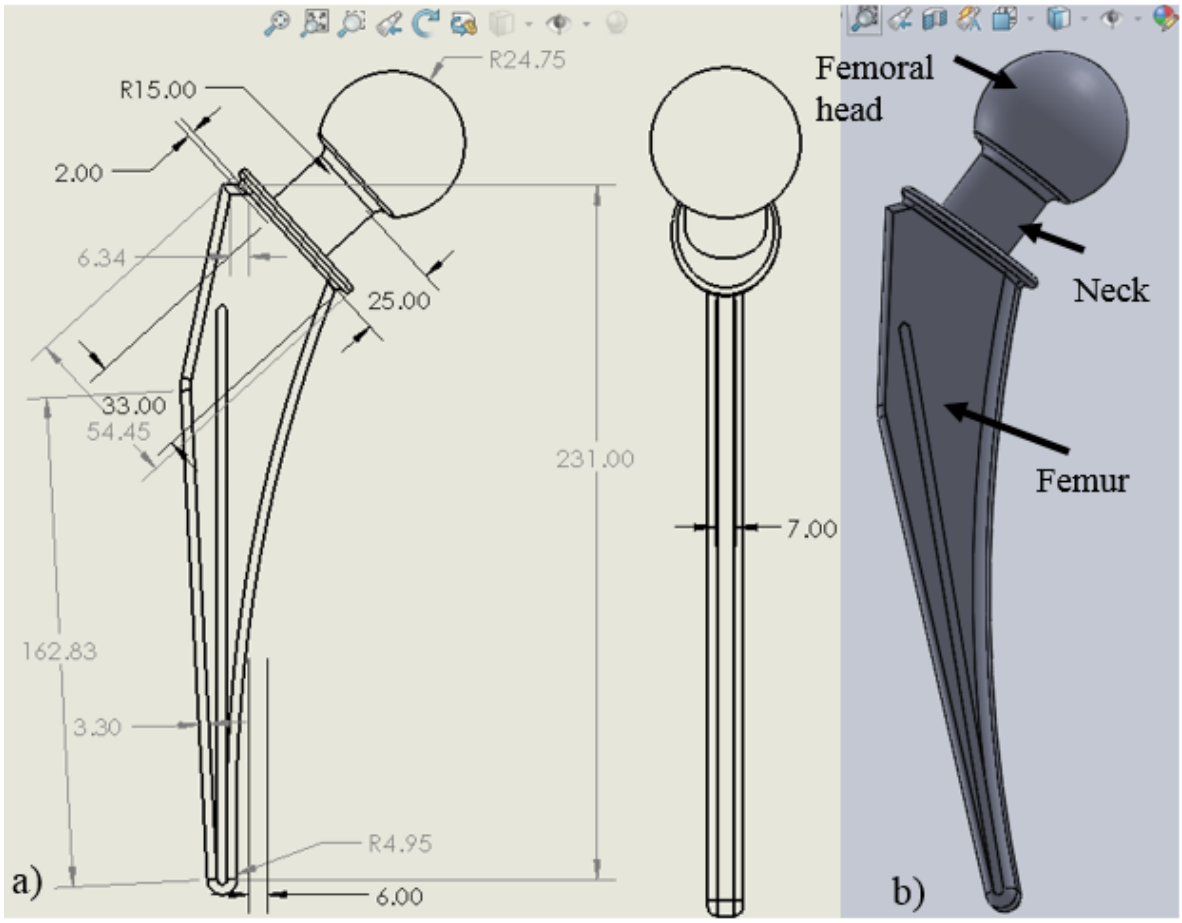

Figure 3.3: (a) 2D and (b) 3D model of the hip joint implant (dimensions in mm)

3.2.3 Control Process Parameters

The quality of FFF manufactured parts primarily depends on the process parameters and their levels. These parameters include printing temperature, layer thickness, print speed, bed temperature, chamber temperature, infill orientation and infill percentage. In this study, the control parameters investigated were printing temperature (A), layer thickness (B), and print speed (C). Printing temperature was

selected since it was a major factor that determines the viscosity of the material, results in improving the bonding strength between layers. Additive manufacturing uses layer by layer technique, thus layer thickness was also crucial in variation of mechanical properties. Print speed was also another important factor that determines the surface quality of the parts. These parameters are essential for improving the mechanical properties of the manufactured parts. However, their effect on deflection, residual stresses and printing time is still unknown. The three selected process parameters and their levels were as presented in Table 3.2. The selection of the printing temperature levels was based on the permissible low and high levels recommended by the material manufacturer (Fiberlogy, 2021). The maximum printing temperature was set at 275 °C, while, the minimum printing temperature was set at 255 °C. If the set temperature is too low the melt becomes more viscous (not sufficiently molten and the material can be stuck inside the nozzle). Likewise, if the set temperature is too high the material becomes less viscous (molted more and hence affect the dimensional stability). As a result, the extruder temperature must be kept within the range in which the material can be semi-liquid. The temperature of extrusion depends on the material used.

The ranges of the layer thickness of 0.1 to 0.3 mm and speed of 30 to 50 mm/s were selected based on the literature (Rahim et al., 2017; Verdejo et al., 2019) and for a nozzle diameter of 0.4 mm. A layer height that is lower than 0.1 mm causes filament to be pushed back into the nozzle while a layer height that is higher than 0.3 mm makes nozzle difficult for layers to adhere to each other.

Table 3.2: Selection of control parameters and their levels

Parameters	**Symbol**	**Unit**	**Level 1**	**Level 2**	**Level 3**
Printing temperature	A	°C	255	265	275
Layer thickness	B	mm	0.1	0.2	0.3
Print speed	C	mm/s	30	40	50

Other FFF parameters were held at their optimum levels obtained from the

literature. These parameters are:

1. Infill percentage: 100 % (Bakir, Atik, & Özerinç, 2020)
2. Infill orientation: 0°/90° (Krajangsawasdi, Blok, Hamerton, & Longana, 2021; Qayyum et al., 2022)
3. Bed temperature: 100°C (Verdejo et al., 2019)
4. Chamber temperature: 60 °C (Shakeria, Benfriha, Zirak, Shirinbayan, & Shakeri, 2021)
5. Nozzle diameter: 0.4 mm (Buj-Corral et al., 2019)
6. Room temperature: 23°C

3.2.4 Design of Experiment

The design of experiment (DoE) that was used in this study was Taguchi's orthogonal array. Several researchers have used Taguchi's orthogonal array because it provides experiments with the minimum number of trials at a reasonable cost as compared to full factorial and surface response methodology(Pervez, Faizan, Zahid, Muhammad, & Yingjie, 2018). In order to draw statistically realistic conclusions using the Taguchi method, choosing a suitable orthogonal array is essential. Since three factors were considered, each one having three levels, the best experimental design was Taguchi's L_{27} orthogonal array (Satish, Girish, & Siddesh, 2019).

Part deflection, residual stresses, and build time were considered as the output responses. Table 3.3 shows orthogonal L_{27} array constructed using Minitab 2018 software. The effect of three parameters and their interactions were studied using L_{27} orthogonal array design.

Table 3.3: L_{27} Orthogonal array designed according to Taguchi method

Run order	Temperature (^{0}C)	Thickness (mm)	Speed (mm/s)
1	255	0.1	30
2	255	0.1	40
3	255	0.1	50
4	255	0.2	30
5	255	0.2	40
6	255	0.2	50
7	255	0.3	30
8	255	0.3	40
9	255	0.3	50
10	265	0.1	30
11	265	0.1	40
12	265	0.1	50
13	265	0.2	30
14	265	0.2	40
15	265	0.2	50
16	265	0.3	30
17	265	0.3	40
18	265	0.3	50
19	275	0.1	30
20	275	0.1	40
21	275	0.1	50
22	275	0.2	30
23	275	0.2	40
24	275	0.2	50
25	275	0.3	30
26	275	0.3	40
27	275	0.3	50

3.2.5 Finite Element Simulation

Digimat 2020 additive manufacturing software (e-Xstream engineering, Belgium) was used to predict residual stresses, part deflection (shrinkage), and build time during the manufacturing of the hip joint implant using the FDM process. Each set of manufacturing parameters was defined in the Ultimaker Cura 4.8.0 software for defining the toolpath and guiding the extruder nozzle along its path to print the part successfully. The results were saved as standard tessellated language and G-codes and

then imported into the Digimat 2020 AM software for simulation in order to study the effect of FDM process parameters on the output responses. The next step was to define manufacturing parameters as required by the Digimat 2020 AM software. The chamber temperature was set to 60 °C, and the extrusion temperature was adjusted from 255°C to 275°C, the same value used during the toolpath definition. A bead width (nozzle diameter) of 0.4 mm was chosen. The convection coefficient was set at 0.015 mW/(mm^2 °C) as recommended by the manufacturer of the Digimat 2020 AM software (E-Xstream, 2019) for the printing simulation setup. Figure 3.4 shows the process parameters set up on Digimat 2020 AM platform. PA12+15 wt % CF material was assigned to the hip implant model.

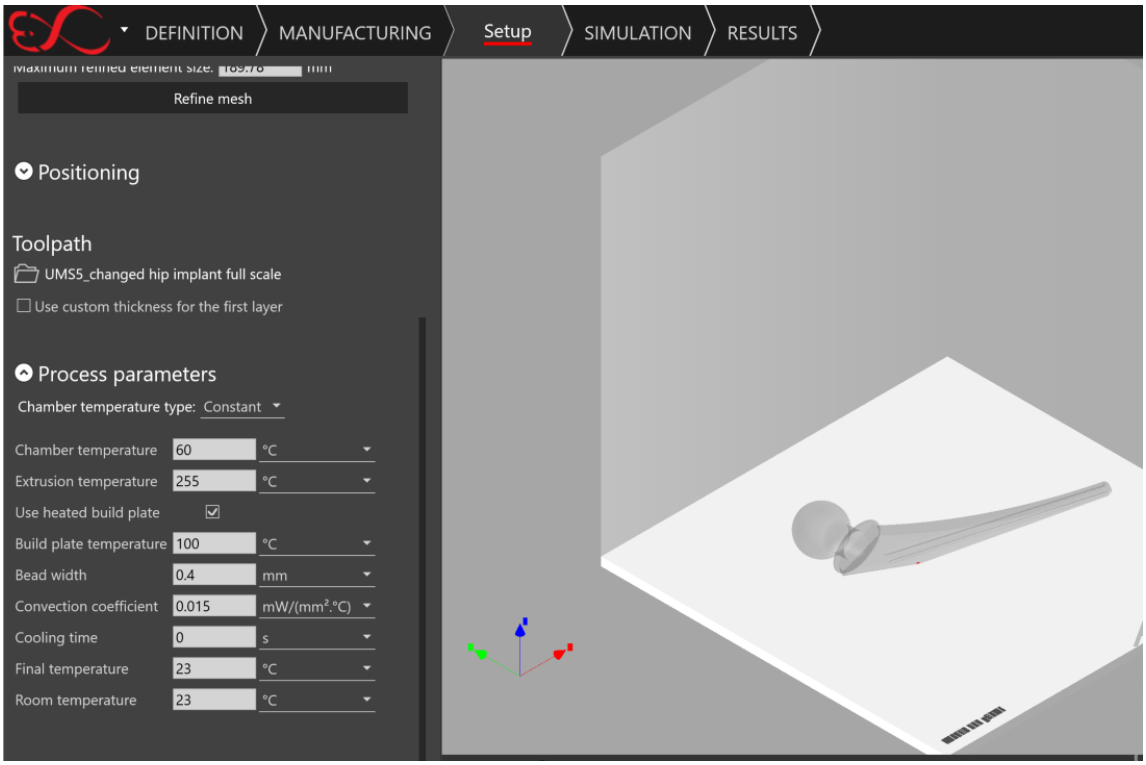

Figure 3.4: Toolpath and manufacturing set up for Digimat 2020 AM

3.2.6 Mesh Generation and Convergence

Tetrahedral, Polyhedral, and Trimmed meshing models are the three types of meshing strategies used to create a volume mesh. Polyhedral and trimmed take more time to generate meshes compared to tetrahedral. The FEA model was then meshed using converged tetrahedral mesh elements due to their capability to fit complex geometry while maintaining element quality and providing good mesh refinement and convergence. The purpose of the mesh convergence study is to ensure that the computed results are not affected by the changing size of the simulation mesh. Mesh convergence of the computed results was studied by comparing results from three different mesh structures with mesh sizes and the number of elements, as summarized in Tables 3.4 and 3.5. A similar approach has been used by other studies (Gebrehiwot, Espinosa Leal, Eickhoff, & Rechenberg, 2021; Rashid et al., 2023).

Table 3.4: Mesh convergence for residusal stress

Mesh Type	Mesh Size (mm)	No. of Elements	Residual Stresses (MPa)	% Difference	Computational time
Coarse	2	21,089	27.32	35	1h
Coarse	1.5	46,264	29.01	31	1h42min
Base	1	136,345	41.75	-	2h
Fine	0.5	1,090,664	40.36	3.3	5h

Table 3.5: Mesh convergence for deflection

Mesh Type	Mesh Size (mm)	Number of Elements	Deflection (mm)	Percentage Difference	Computational time
Coarse	2	21,089	3.933	24	1h
Coarse	1.5	46,264	3.817	20	1h42min
Base	1	136,345	3.175	-	2h
Fine	0.5	1,090,664	3.142	1.7	5h

The results observed about 35 % and 24 % difference in residual stress values and deflection was observed between the coarse and base meshes. A 3.3 % and 1.7 % difference between the base and fine meshes. However, the mesh size had an insignificant variation on build time. This was due as the mesh size varied the build

time remained constant. The 3.3 % and 1.7 % difference between the base and fine meshes indicated that the base mesh yielded a satisfactory mesh converged solution state and was chosen for generating acceptable results in this study. In addition, the computation time of 1 mm base mesh size was 2.5 times that of a mesh size of 0.5 mm. Therefore, a base mesh size of 1 was considered to avoid higher computational time for the analysis. The total number of elements in the component model was 136,345 voxels. These elements were kept constant for all simulations. The meshed geometry of the hip implant is shown in Figure 3.5.

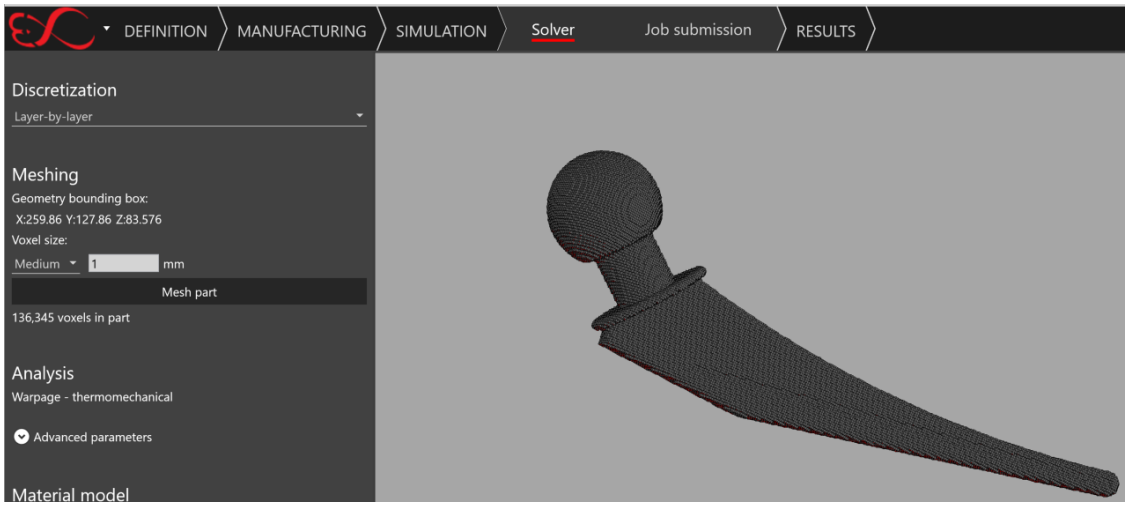

Figure 3.5: Finite element mesh of the hip joint implant

3.2.7 Thermal Modeling Governing Equations

In the FDM process, the filament material was extruded at temperature above melting temperature (T_f) of the printing material and deposited on the base plate with a temperature T_p. Due to temperature gradients, the deposited materials exchanged thermal energy with the previously deposited material and the surrounding air in the chamber. As the cooling process was transient, the transient thermal problem was based on energy conservation. The governing equation of the thermal energy conservation was 3D transient heat conduction and heat generation (Y. Zhang & Chou, 2006b) given by:

$$\rho c_p \frac{\partial T}{\partial t} = \nabla.(k\nabla T) + q \tag{3.1}$$

Where ρ is the density of the printed material, c_p is the specific heat of the printed material, ∇T is the spatial gradient of the temperature, t is the time, k is the thermal conductivity and q is the heat generation rate. Equation 3.1 can be rewritten as:

$$\rho c_p \frac{\partial T}{\partial t} = k\nabla^2 T + q \tag{3.2}$$

where
$\nabla^2 = \frac{\partial^2}{\partial x^2} + \frac{\partial^2}{\partial y^2} + \frac{\partial^2}{\partial z^2}$

3.2.8 Boundary Conditions

In the linear thermal analysis, a constant temperature T_p was set at the bottom surface where the part was in contact with the build platform. Convective boundary conditions were set along the other outer surfaces, appropriately imposing convective heat coefficient and the chamber temperature. The heat loss through convection is given in Equation 3.3.

$$q_c = h(T - T_c) \tag{3.3}$$

where h is the convective heat coefficient which is the approximate global convection exchanges happening inside the printer as a result of the printer setup. The convection heat coefficient was set to 0.015 mW/(mm^2 °C) as recommended for the printing setup and the material selected. T_c is the building chamber temperature and was set to 60°C.

Each new activated geometry was set to a temperature equal to that of the temperature of the extrusion nozzle (T_f). During the printing process, the geometries

that have already been printed lose heat to the 3D printer chamber by natural convection, as shown in equation 3.3. In the FDM process, heat transfer is primarily controlled by both conduction and convection (Y. Zhang & Chou, 2006b). The magnitude of the heat transfer coefficient determines the significance of heat exchanges with the environment via radiation. Heat lost by radiation must be ignored when the convective heat coefficient is greater than or equal to 0.006 mW/(mm^2 °C) (Costa et al., 2014). Heat loss by radiation was therefore not considered since the convective heat coefficient was greater than 0.006 mW/(mm^2 °C). The setting of boundary conditions was as presented in Figure 3.4. The layer-by-layer structural simulation was finally run to simulate the manufacturing process, and a thermo-mechanical analysis was done.

3.2.9 Equations for Residual Stresses and Strains

The temperature gradient obtained during the thermal analysis was used to determine the thermal stresses and strains. Both accumulated residual stresses and strains were highly sensitive to the temperature distribution within the deposited layers at T(l,t), where l is any point at a time instant t. When the deposited layer was reheated, there was a temperature difference which caused the accumulation of thermal stresses and strains in the material. Thermal strain is represented by Equation 3.4.

$$\{\epsilon_t\} = \alpha(T - T_R) \tag{3.4}$$

where $\{\epsilon_t\}$ refers to thermal strains, α is the coefficient of thermal expansion, T is the solid model temperature and T_R is the reference temperature at the surface of the previous layer.

Thermal residual stresses were obtained according to Equation 3.5.

$$\{\sigma\} = [E]\{\epsilon_t\} \tag{3.5}$$

where E is the Young's modulus and $\{\sigma\}$ are the thermal stresses. The digimat 2020 AM software evaluated the results after printing, cooling process, and support removal.

3.2.10 Taguchi Optimization Method

The Taguchi technique uses the concept of signal-to-noise (S/N) ratio as a performance output characteristics in order to evaluate the processing parameters. The S/N ratio is a logarithmic function of the target output used as the optimization's objective function. The S/N ratio is the ratio of the mean (signal) to the standard deviation (noise). This ratio establishes the optimum parameter level for a robust response. Depending on the objective function, there are three types of S/N ratios: the lower the better [Equation 3.6], the higher the better [Equation 3.7], and the nominal the better [Equation 3.8] and as shown in Equations 3.6, 3.7, and 3.8 (G. Dong, Wijaya, Tang, & Zhao, 2018; Sharma, Kumar, Singh, & Rawat, 2021; Sumalatha, Malleswara Rao, & Supraja Reddy, 2021).

$$\frac{S}{N} = -10 \log \sum_{n=1}^{n} \frac{Y_i^2}{n} \tag{3.6}$$

$$\frac{S}{N} = -10 \log \sum_{n=1}^{n} \frac{\frac{1}{Y_i^2}}{n} \tag{3.7}$$

$$\frac{S}{N} = 10 \log \frac{\bar{Y}^2}{s^2} \tag{3.8}$$

where Y_i is the responses, n is the number of responses for each combination,$\bar{Y}$ is the

average of data observed and s^2 is the variance (average of the squared differences observed values from the mean).

The idea was to maximize the S/N ratio by minimizing the effect of the noise (variability in the output). For a response of residual stresses, part deflection, and build time, the lower-the better quality characteristic was considered.

3.2.11 Grey Relational Analysis (GRA)

The primary Taguchi method for determining the optimum process parameters emphasizes only a single performance characteristic (Kuo, Yang, & Huang, 2008). However, multiple response characteristics must be identified in many cases simultaneously. Taguchi Grey Relational Analysis (GRA) was adopted since it is an appropriate and advanced form of Taguchi that optimizes two or more responses simultaneously (C. C. Wang, Lin, & Hu, 2007).

GRA combines all response characteristics into a single value called Grey Relation Grades (GRGs) that can be used as the single quality characteristic in the optimization technique. In this study, residual stresses, part deflection, and build time were optimized using grey relational analysis. GRA uses the following steps:

The first step in GRA is normalizing the raw data to a range of 0-1. Residual stresses, part deflection, and build time responses are normalized using the following equation 3.9 (Aslani et al., 2020) since they correspond to the lower-the-better quality:

$$X_i(k) = \frac{max\ y_i(k) - y_i(k)}{max\ y_i(k) - min\ y_i(k)} \tag{3.9}$$

where X_i is the normalized value of the original data $y_i(k)$ and $max\ y_i(k)$, $min\ y_i(k)$ denote the maximum and minimum of $y_i(k)$ respectively.

Grey relational coefficient is generated in order to connect the desired and actual

normalized data as follows:

$$\xi_i(k) = \frac{\Delta_{min} + \Psi\Delta_{max}}{\Delta_{0i}(k) + \Psi\Delta_{max}} \tag{3.10}$$

where

$$\Delta_{0i}(k) = ||X_0(k) - X_i(k)|| \tag{3.11}$$

$\Delta_{0i}(k)$ is the deviation sequence for the reference sequence X_0 (k) and comparable sequence $X_i(k)$, Ψ is the distinguishing coefficient where $0 < \Psi < 1$, and Ψ is usually kept as 0.5.

Δ_{min} is the smallest value of $\Delta_{0i}(k)$

Δ_{max} is the highest value of $\Delta_{0i}(k)$

Finally, grey relational grade (γ_i) is computed by averaging values of grey relational coefficients. where

$$\gamma_i = \frac{1}{n}\sum_{n=1}^{n} \xi_i(k) \tag{3.12}$$

The optimization of the grey relational grade is equivalent to the optimization of all the quality responses considered in this study. The parameter combination with the highest GRG from Equation 3.12 is the optimal condition for combined process parameters to manufacture hip joint implant.

3.2.12 Analysis of Variance

Analysis of variance (ANOVA) was applied to the results using Minitab 2018 software. It uses a p-value that tests the significance of input parameters and their interactions with the response characteristics. The percentage contribution of each parameter and errors are also determined using ANOVA.

3.2.13 Optimization with Genetic Algorithm

A genetic algorithm (GA) code was also used in this research to confirm whether the optimum parameters obtained using the Grey Taguchi method are the same as using the GA code. The GA code was set to obtain the highest possible grey relational grade. The Equation 3.13 obtained from the relationship between the process parameters and gray relational grade was used as the GA's objective function and maximized. The objective function was derived from simulations. For optimization to be conducted using GA, the constraints were set as shown in Table 3.6. Appendix A shows genetic algorithm code used in optimizing the objective function.

$$Y = 3.915 - 0.020X_1 + 1.927X_2 + 0.014X_3 \tag{3.13}$$

Where Y is the GRG, X_1 is the printing temperature (°C), X_2 is the layer thickness (mm), and X_3 is the print speed (mm/s).

Table 3.6: Constraints used in GA

Input parameter	Lower Limit	Upper Limit
Printing temperature (°C)	255	275
Layer thickness (mm)	0.1	0.3
Printing speed (mm/s)	30	50

Regression analysis was performed in Minitab 2018 software to establish the relationship between the process parameters and the response according to the regression theory. A fitting mathematical model that can be used to predict the estimated output value was determined through Minitab 2018 software.

3.3 Methodology for Objective Two

3.3.1 Experimental Work

3.3.1.1 3D Printing

A computer model of the hip joint implant was manufactured using the optimum levels of process parameters obtained through grey relational analysis and confirmed using GA. The same optimum simulation G-code file was fed to the fusion 3D 410 printing machine (Fusion 3 3D printer, USA) using a memory card. The fusion 3D 410 machine heated the PA12 with 15 wt % filament and extruded through a nozzle of diameter (0.4 ±0.08) mm to print the hip joint implant layer by layer as shown in Figure 3.6. Three hip joint implants were printed and build time during the manufacturing of each implant was monitored.

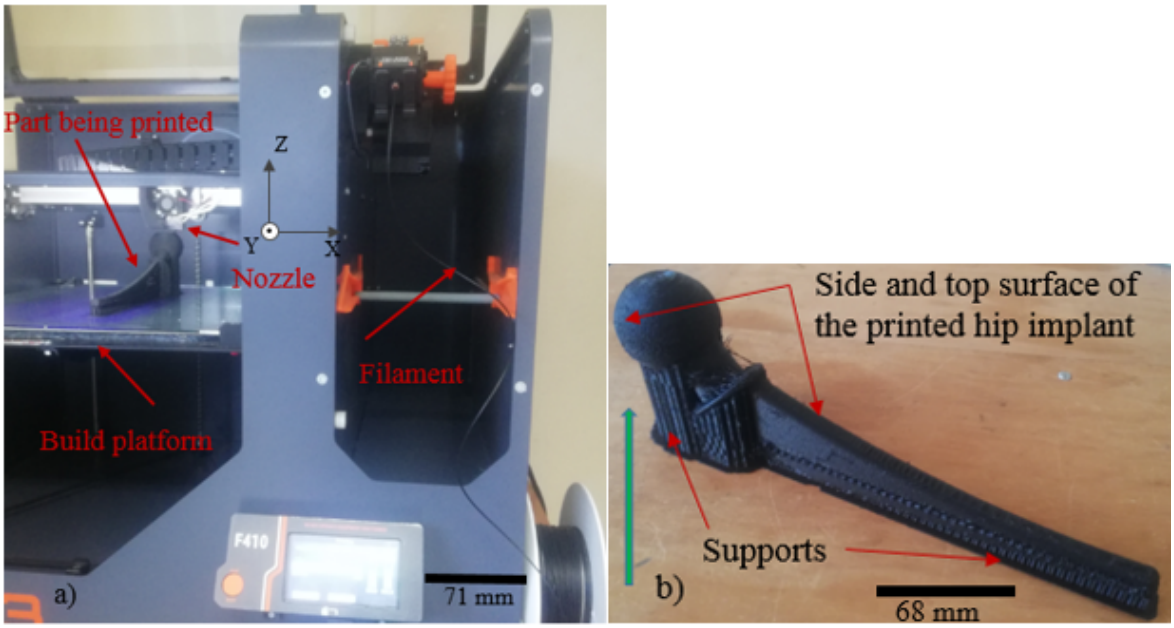

Figure 3.6: (a) 3D printing hip joint implant with fusion 3D 410 printer, (b) Printed hip joint implant before support removal. The green arrow indicates the building direction.

3.3.1.2 Part Deflection Measurement

Dimensional control of joint components is critical since it directly impacts their durability and, as a result, on the patients' quality of life. The evaluation of hip implant design typically involves geometry measurement and surface finish assessment. Geometrical measurement involves sphericity measurement for form evaluation. The final diameter of the spherical head of the 3D printed hip joint implants was measured using a Vernier caliper, as presented in Figure 3.7. The measurements were repeated three times for each sample, and the average taken. The part deflection was obtained by subtracting the final head diameter size from the initial head diameter size.

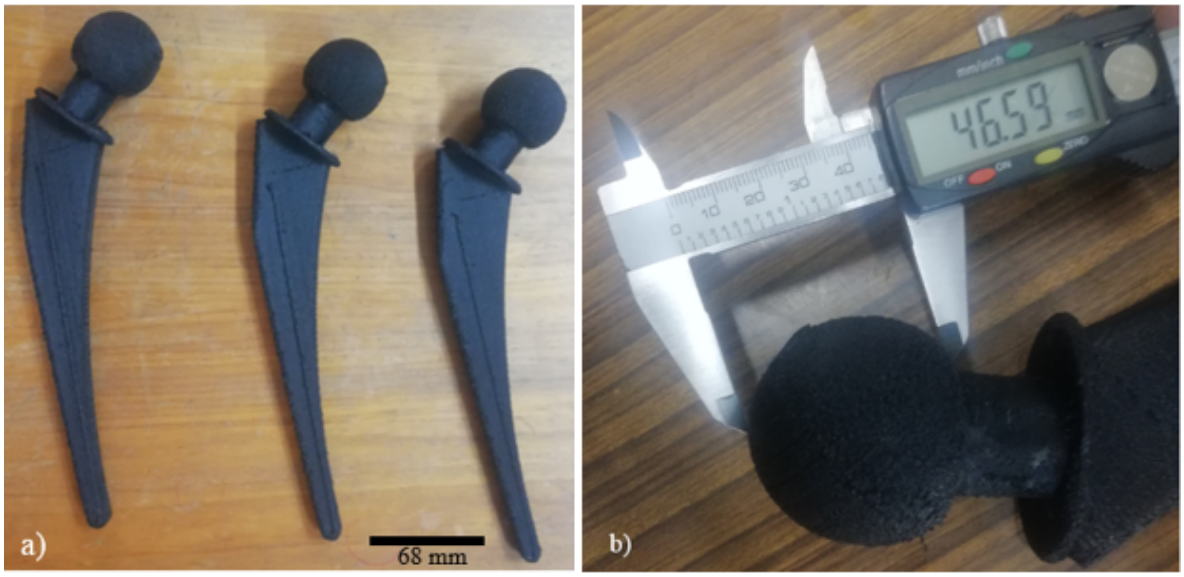

Figure 3.7: (a) 3D printed after the support removal, (b) Measuring of part after 3D printing.

3.3.1.3 Measurement of Residual Stresses

The specimen for residual stress measurement was cut from the implant's femoral head, where maximum residual stresses were obtained using the finite element method. Strain gauge rosettes were attached to the specimen using cyanoacrylate

adhesive. A drill was positioned at the center of the three strain rosettes using an optical microscope (Sint Technology, Italy), as shown in Figure 3.8. Holes were drilled in 20 depth increments (h) of 0.05 mm up to 1 mm depth according to the ASTM E837-13a (*ASTM E 837-13a: Standard Test Method for Determining Residual Stresses by the Hole-Drilling Strain-Gage Method*, 2013). Due to hole drilling, the locked up residual stresses were relieved and the corresponding strains on the surface were acquired on each depth using a Quantum X HBM digital strain gauge amplifier (Sint Technology, Italy). After completing the drilling test, the relaxed strains were imported into the EVAL 7 calculation software developed by Sint Technology, Italy for residual stress calculation.

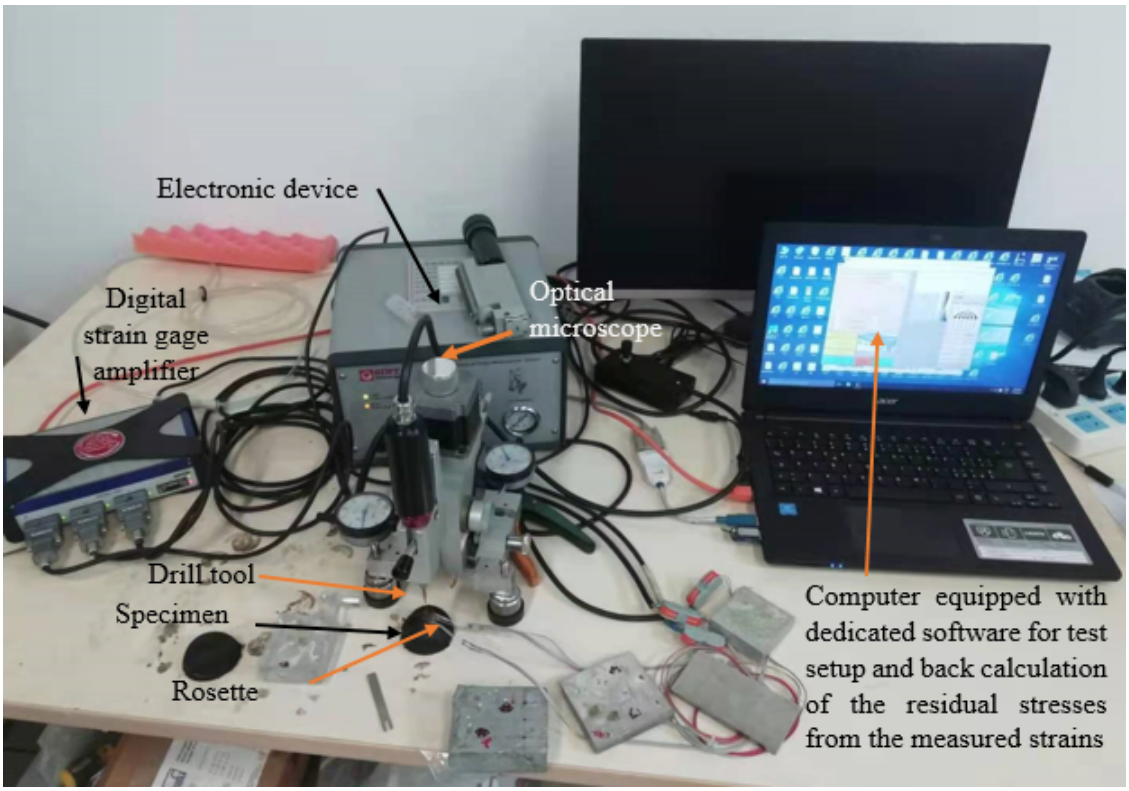

Figure 3.8: Residual stress measurement using Restan MTS3000

The calculation of non-uniform stresses was carried out according to the integral method (Schajer, 2017). The integral method is adequate for computing stress fields

when they are expected to vary considerably through the thickness. The integral approach requires different sets of coefficients to relate the surface strain changes to the residual stress present for each stress and hole depth combination. The ASTM E837-13a standard (*ASTM E 837-13a: Standard Test Method for Determining Residual Stresses by the Hole-Drilling Strain-Gage Method*, 2013) provides these calibration matrices derived by the integral method. The experimental set up was as shown in Figure 3.8. The maximum principal stresses (σ_{max}), minimum principal stresses (σ_{min}) and the orientation angle (β) from the x-axis (gage 1) to the maximum principal stresses for each hole depth were obtained as shown in Figure 3.9.

The sequence number of the hole depth steps is illustrated in Figure 3.9 where D_h is the hole diameter and D_{mg} is the strain gage diameter

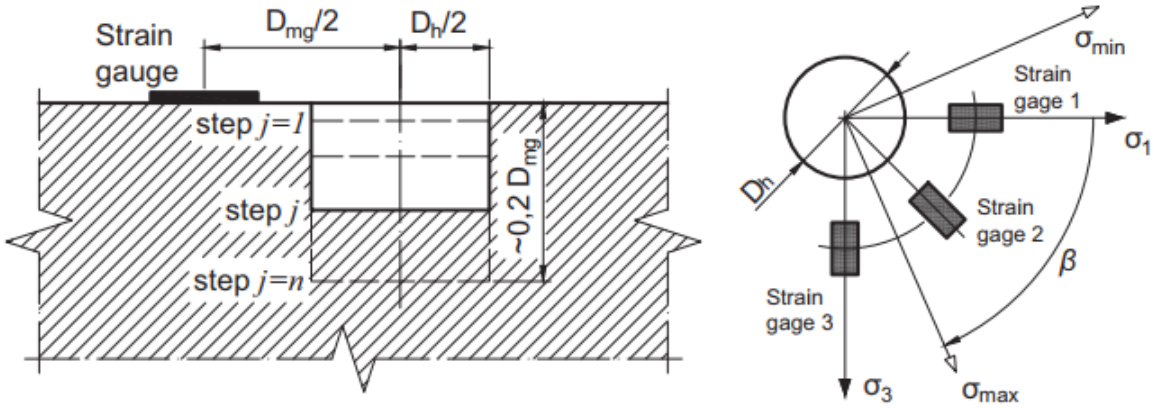

Figure 3.9: Gage placement, drilling hole location, and sequencing (Peral et al., 2017)

3.3.1.4 Relationship Between Strains and Stresses

Using the ASTM-E837 (*ASTM E 837-13a: Standard Test Method for Determining Residual Stresses by the Hole-Drilling Strain-Gage Method*, 2013), the following combination strain vectors can be computed for each set of measured strains, ϵ_1 , ϵ_2 and ϵ_3.

$$p_j = \frac{(\epsilon_3 + \epsilon_1)_j}{2} \tag{3.14}$$

$$q_j = \frac{(\epsilon_3 - \epsilon_1)_j}{2} \tag{3.15}$$

$$t_j = \frac{(\epsilon_3 + \epsilon_1 - 2\epsilon_2)_j}{2} \tag{3.16}$$

where p is the isotropic strain within the hole depth step, q is the 45° shear strain after the hole depth step, t is the $x - y$ shear strain after the hole depth step, and the subscript j refers to the number of hole depth steps so far corresponding to the successive sets of measured strains ϵ_1 , ϵ_2 and ϵ_3.

By calculating, the following matrix equations (where the bar accent indicates a matrix) using the integral approach, the residual stresses within each hole depth step can be estimated from the corresponding observed strains as presented by Equations 3.20 to 3.22

$$\bar{a}P = \frac{E}{1+v}p \tag{3.17}$$

$$\bar{b}Q = Eq \tag{3.18}$$

$$\bar{b}T = Et \tag{3.19}$$

In which

$$P_k = \frac{(\sigma_y)_k + (\sigma_x)_k}{2} \tag{3.20}$$

$$Q_k = \frac{(\sigma_y)_k - (\sigma_x)_k}{2} \tag{3.21}$$

$$T_k = (\tau_{xy})_k \tag{3.22}$$

Where k is the sequence number for hole depth steps, $\bar{a}$ and $\bar{b}$ are lower triangular calibration matrices of $\bar{a}_{jk}$, $\bar{b}_{jk}$ constants that correspond to the hole depth and type of rosette used. P_k is isotropic stress within hole depth step k, Q_k is the 45° shear stress within hole depth step k, T_k is the $x - y$ shear stress within hole depth step k, E is the material Young's modulus, v is the Poisson's ratio of the material, $(\sigma_y)_k$ is the normal y-stress within hole depth step k, $(\sigma_x)_k$ is the normal x-stress within hole depth step k, and $(\tau_{xy})_k$ is the shear xy-stress within hole depth step k.

The component $\bar{a}_{jk}$ represents strain relaxation due to a unitary isotropic stress within increment k (indicated by column number) of a hole of depth j (indicated by row number) as is illustrated in Figure 3.10, where a hole is drilled in three depth steps. The component $\bar{b}_{jk}$ has the same interpretation when considering shear stresses.

As the matrices $\bar{a}$ and $\bar{b}$ in the ASTM 837 (*ASTM E 837-13a: Standard Test Method for Determining Residual Stresses by the Hole-Drilling Strain-Gage Method*, 2013) are tabulated for nominal hole diameter D_0=2 mm, they can be adjusted to fit the measured hole diameter (D_h) as follows:

$$(\bar{a}_{jk})_{adjusted} = \bar{a}_{jk} * (\frac{D_0}{D_h})^2 \tag{3.23}$$

$$(\bar{b}_{jk})_{adjusted} = \bar{b}_{jk} * (\frac{D_0}{D_h})^2 \tag{3.24}$$

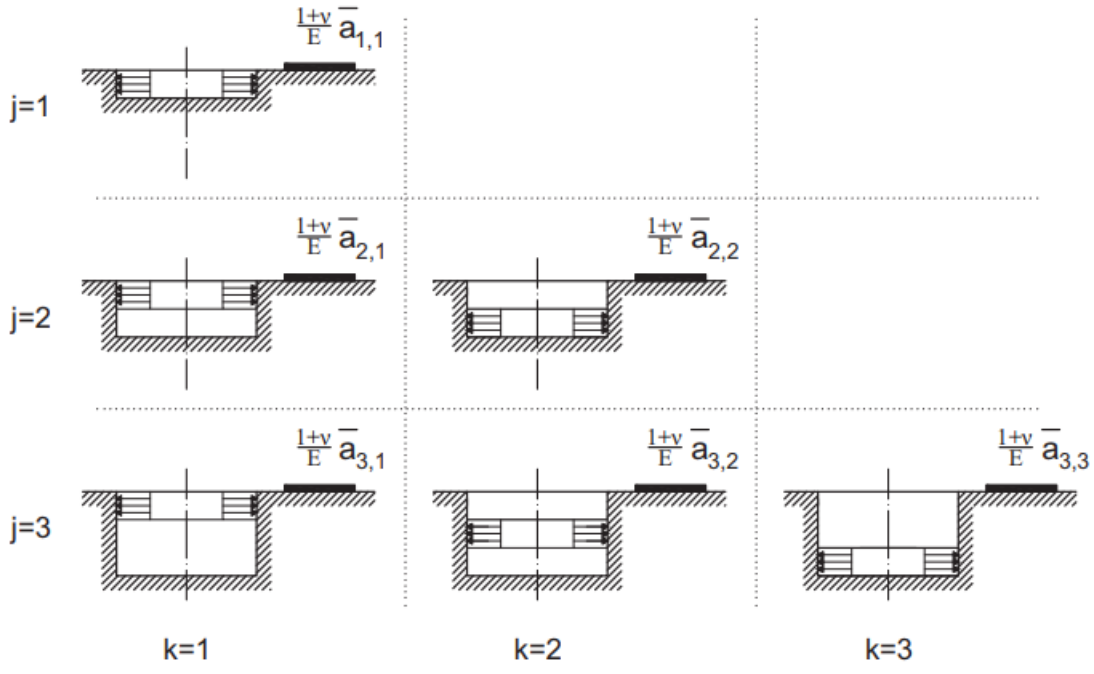

Figure 3.10: Physical interpretation of $\bar{a}_{jk}$ (Peral et al., 2017)

From Equations 3.25 to 3.27 (Schajer, 2017), can be used to compute the Cartesian stresses

$$(\sigma_x)_j = P_j - Q_j \tag{3.25}$$

$$(\sigma_y)_j = P_j + Q_j \tag{3.26}$$

$$(\tau_{xy})_j = T_j \tag{3.27}$$

Finally, the principal stresses and their direction as given by angle β measured clockwise from strain gauge one direction to the maximum principal stress direction are calculated using equations: 3.28 and 3.29

$$(\sigma_{max})_k, (\sigma_{min})_k = P_k \pm \sqrt{Q_k^2 + T_k^2} \tag{3.28}$$

$$\beta_k = \frac{1}{2} \tan^{-1}(\frac{-T_k}{-Q_k}) \tag{3.29}$$

where σ_{max}: maximum (more tensile) principal stress and σ_{min}: minimum (more compressive) principal stress

A positive value of β implies that σ_{max} lies in the clockwise from gage 1. A negative value of β implies that σ_{max} lies counter-clockwise from gage 1.

3.4 Methodology for Objective Three

3.4.1 Surface Roughness Measurement

Average surface roughness (Ra) is critical for reducing friction and wear on hip prostheses. The standard surface roughness tester of Mitutoyo SJ-301 (Mitutoyo, Tokyo) was used to record the roughness (Ra) as illustrated in Figure 3.11. The start key was pressed and the probe started traveling to a distance equal 0.8 mm, and then displayed the measured value (Aslani et al., 2020). Roughness values at five different points on the specimen were recorded, and their average was considered.

Three samples were taken from the femur, femur neck, and femoral head of the manufactured hip implant, as illustrated in Figure 3.12.

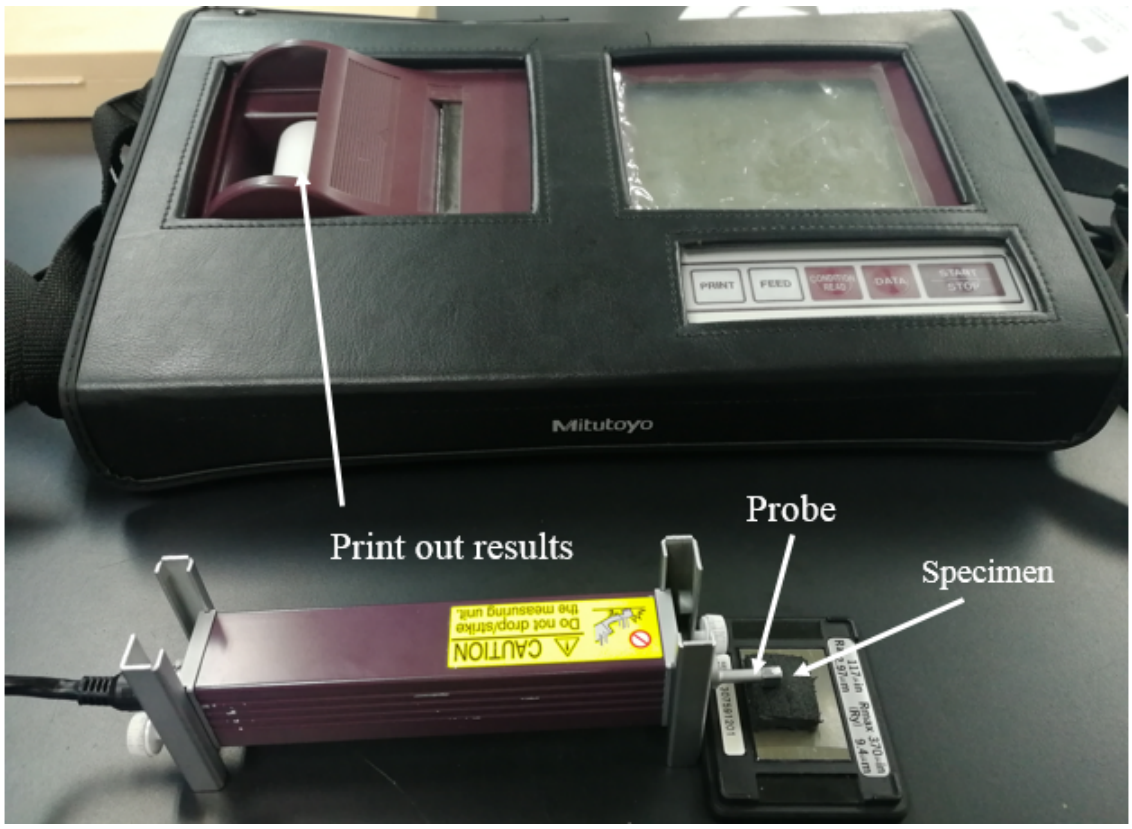

Figure 3.11: Measurement of surface roughness using Mitutoyo SJ-301

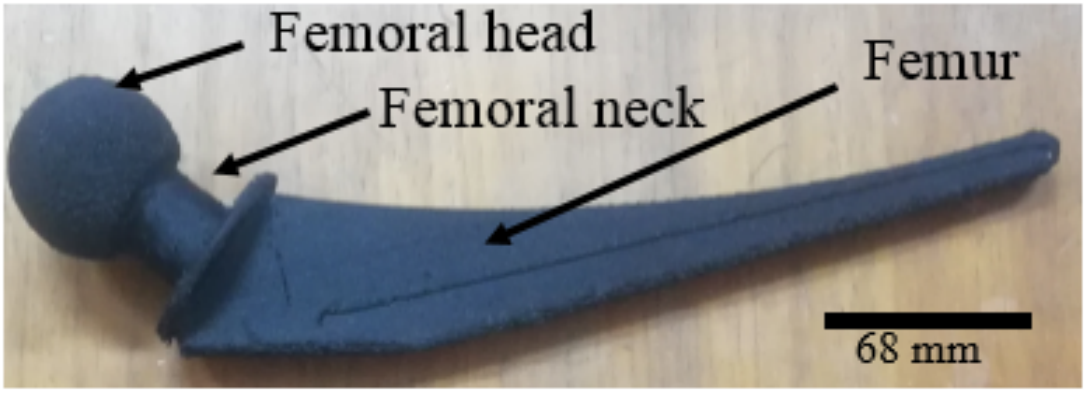

Figure 3.12: Surface measurement areas

3.4.2 Tensile Testing

The specimens for the tensile test were machined from the 3D printed hip joint according to ASTM D638-4 specifications (*ASTM D638-14: Standard Test Method for Tensile Properties of Plastics*, 2014). Figure 3.13 shows the dimensions of the tensile test specimen. The tensile testing was carried out using Tinius Olsen Universal Testing Machine (Tinius Olsen, USA) with a load cell of 10 kN and a continuous crosshead speed of 5 mm/min at room temperature. Five specimens were tested for tensile properties and their average taken into consideration. Horizon data acquisition software (Tinius Olsen, United States of America) connected to the tensile test machine was used to obtain the tensile strain–stress curves. The specimen clamping in the machine is presented in Figure 3.15. The fracture surface analysis was done using Scaning Electron Microscope (NeoScope JCM-7000, Jeol Ltd., Tokyo).

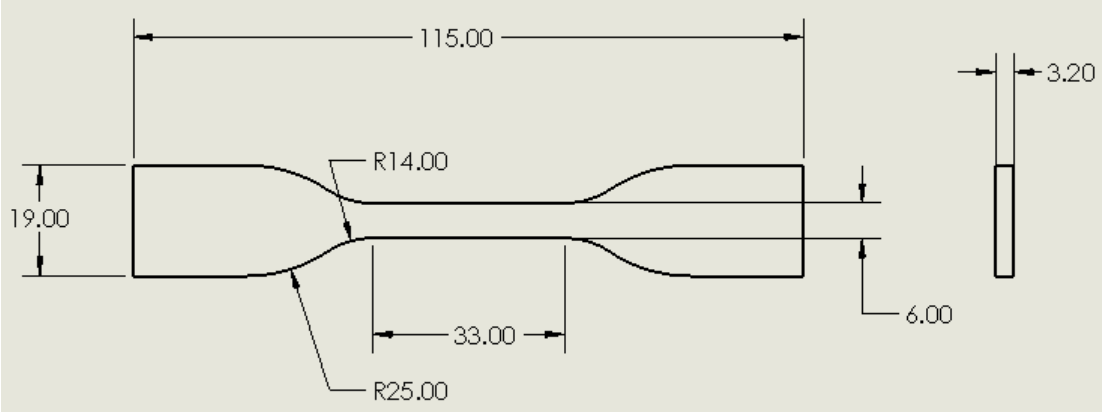

Figure 3.13: Dimension of tensile test specimen (mm).

Figure 3.14: Prepared tensile test specimen

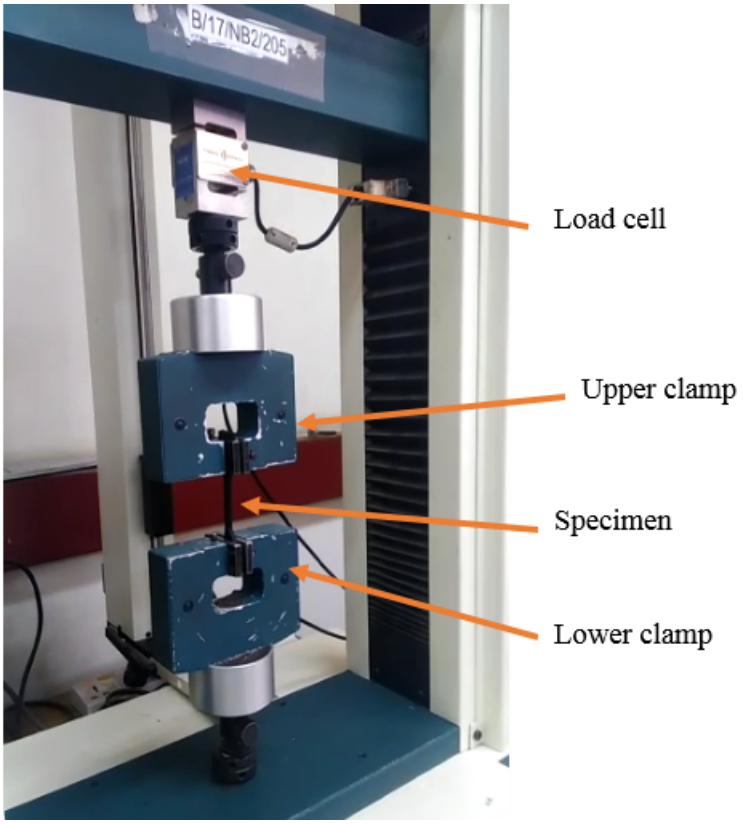

Figure 3.15: Experimental setup for tensile test

3.4.3 Compression Testing

The compression test specimens were prepared according to ASTM D695 (*ASTM D695-15: Standard Test Method for Compressive Properties of Rigid Plastics*, 2015), a standard procedure for testing the compressive properties of plastics. Figure 3.16 illustrates the dimensions of the compressive test specimen. The compressive tests were performed using Tinius Olsen Universal Testing machine (Tinius Olsen, USA). The machine was set at the test speed prescribed by ASTM D695 (*ASTM D695-15: Standard Test Method for Compressive Properties of Rigid Plastics*, 2015) i.e 5 mm/min, a load cell of 10kN, and two specimens were tested at room temperature. A desktop computer loaded with Horizon software (Tinius Olsen, USA) and connected to the compressive test machine was used to obtain the compressive strain–stress curves. Maximum compressive strengths were then obtained.

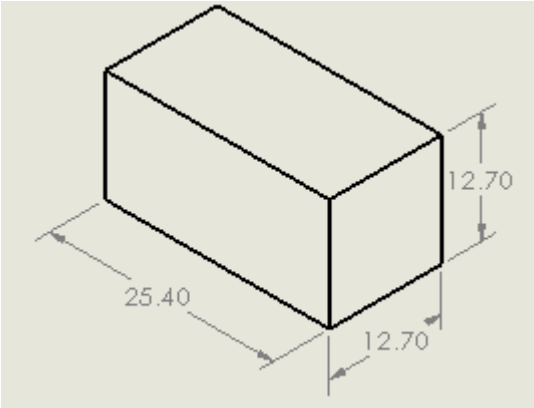

Figure 3.16: Dimensions of compression test specimen (mm)

3.4.4 Fatigue Testing

Cyclic fatigue testing was carried out on 3D printed CF/PA12 composite hip implant using the Servopulser fatigue testing machine (Shimadzu Servopulser EHF-L Series, Tokyo) shown in Figure 3.17 (a). Specimen dimensions and geometry were made according to ASTM D638-4 standard (*ASTM D638-14: Standard Test Method for*

Tensile Properties of Plastics, 2014) to investigate the fatigue properties in tension. Fatigue test was done at room temperature under repeated (tension–tension) cyclic loading at a frequency of 5 Hz, and a stress ratio of R=0. In order to evaluate the mechanical durability of the 3D printed composite, the specimens were subjected to four levels of maximum stress loading of 50, 60, 70, and 80 % of the pre-determined ultimate strength. Two specimens were tested for each fatigue load level. Cyclic fatigue testing ended when the specimen got ruptured. The specimen clamping in the machine is illustrated in Figure 3.17 (b).

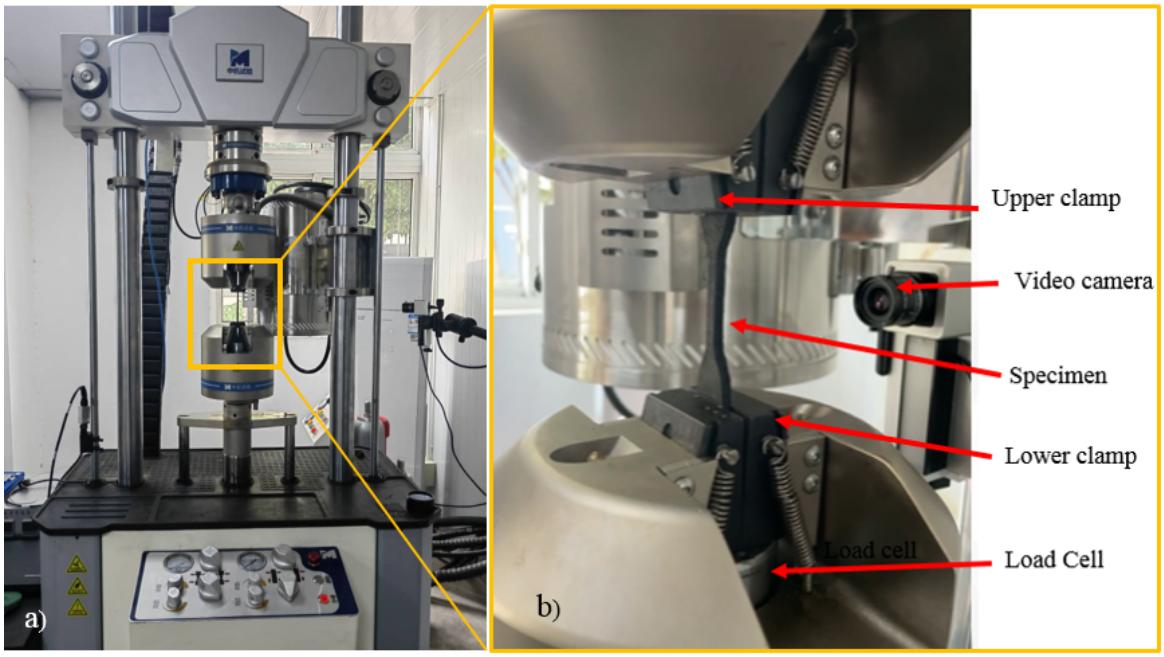

Figure 3.17: Experimental setup for fatigue test

CHAPTER FOUR

RESULTS AND DISCUSSION

4.1 Validation Results

The simulation findings are shown in Table 4.1. From the results, it can be seen that the computation time increases with decrease in mesh size while the inverse is true for number of elements. This is expected since the smaller the mesh size the more the elements and therefore the bigger the computation domain. The percentage deviation between experimental and simulation residual stresses was 6.38 %, 6.62 %, 40.43 % and 72.63 % for mesh sizes 0.5 mm, 1 mm, 1.5 mm, and 2 mm, respectively. A mesh size of 0.5 gave the least error between experimental and simulation results followed by a mesh size of 1 mm. However, a mesh size of 1 mm was chosen as the most appropriate because its computation time was approximately 2.5 times that of a mesh size of 0.5 mm. Further, the difference in results between these two was 0.2 % which was considered insignificant. In literature, errors below 10 % have been noted when experimental results are compared to simulation results (Gebrehiwot et al., 2021). Therefore, a mesh size of 1 mm gave the best combination in terms of accuracy of results and computation time and was selected for further simulations. The results of a mesh size of 1 mm is shown in Figure 4.1.

Table 4.1: Validation of simulation and experimental results

Mesh size (mm)	No. of Elements	Computational Time	RS (MPa)	Error between Simulated and Experimental results (%)
0.5	178,200	3h47min	6.383	6.383
1	22400	1h	6.397	6.617
1.5	7290	38 min	3.574	40.43
2	3200	20 min	1.642	72.63

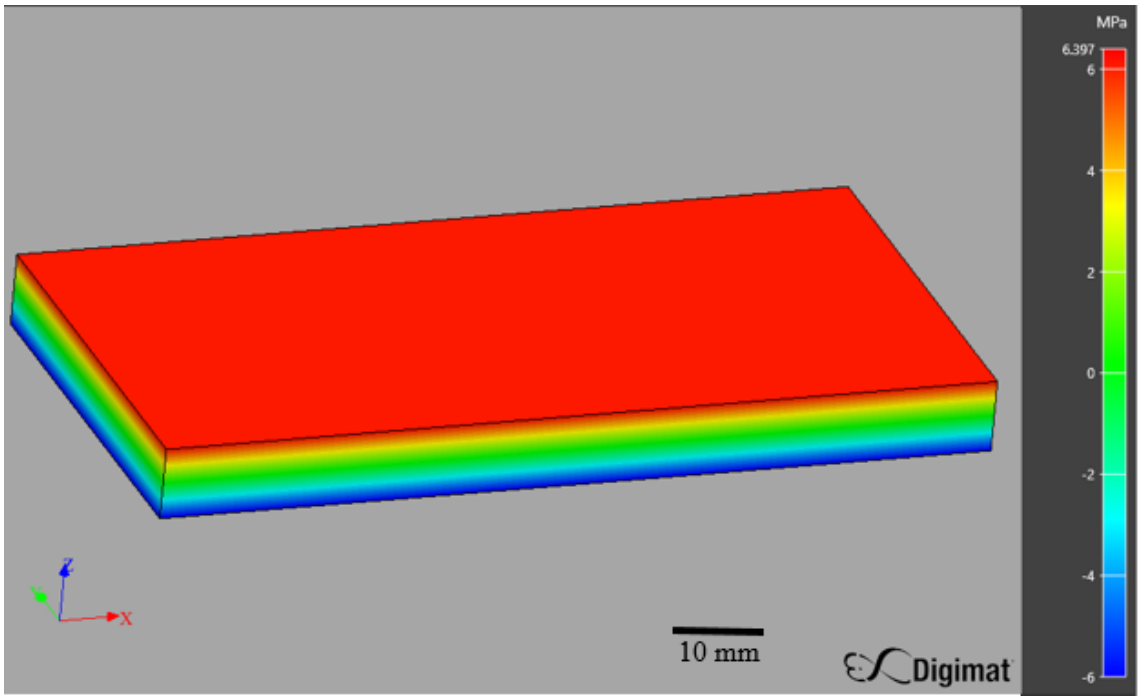

Figure 4.1: Preliminary residual stress results

4.2 Simulated Deflection and Residual Stress Results

Part deflection results of the hip implant model from the FFF process were as shown in Figure 4.2. Digimat 2020 AM numerical simulation software was able to accurately follow the actual printing process, account for all process variables, and enable the prediction of the part's deflection, residual stresses and build time. In the numerical simulation, cooling of the model through conduction and convection was factored in. Once the finite element analysis was performed, support structures were removed and results displayed.

The component, however, experienced significant shrinkage as the temperature dropped below the printing chamber's constant temperature of 60 °C. The term "part deflection" refers to the dimensional deviation of a component after it had

been printed, cooled, and the support removed. This provides crucial details about the exact dimension of the product after manufacturing. The accumulated part deflection is illustrated in Figure 4.2.

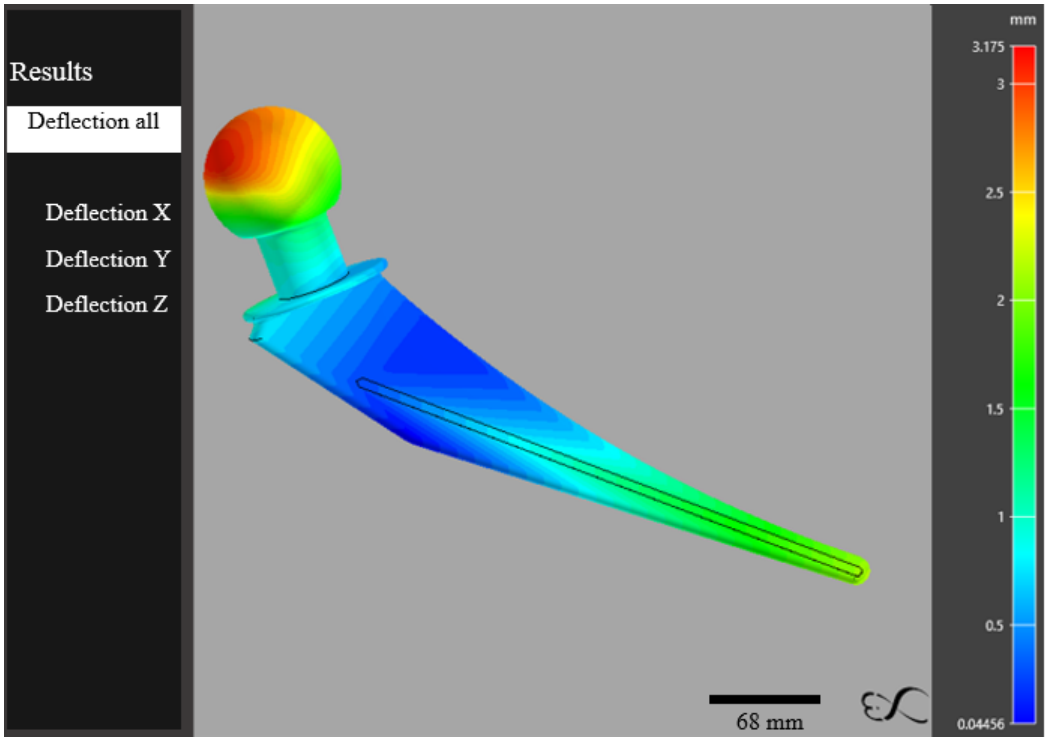

Figure 4.2: Simulated deflection results

From Figure 4.2, the highest deflection was observed at the head of the implant. A possible explanation for this observation could be the fact that the part was printed from the bottom to the top of the model, allowing layer-to-layer bonding to shrink from the bottom to the top. Residual stresses induced by uneven rapid heating and cooling cycles cause the bottom layers of the component were susceptible to localized contraction which was a major contributor to the observed part deflection. Similar results were observed by Zhang and Chou (Y. Zhang & Chou, 2006a), who argued that the bottom layers of the printed part were vulnerable to distortion during fabrication due to high residual stresses obtained in that specified region. The deflection results give important information about the actual geometry after

manufacturing. The absolute actual dimensions of the components in working condition is given by the sum of the deflection and the dimensions of the part before 3D printing.

Figure 4.3 shows the accumulated simulated residual stress results in the hip joint implant. Similar to the deflection results, the highest residual stresses were observed at the head of the hip implant. These residual stresses developed as a result of reheating and cooling of the deposited layers during the printing process. This information was used when developing the final structural model in order to achieve accurate results.

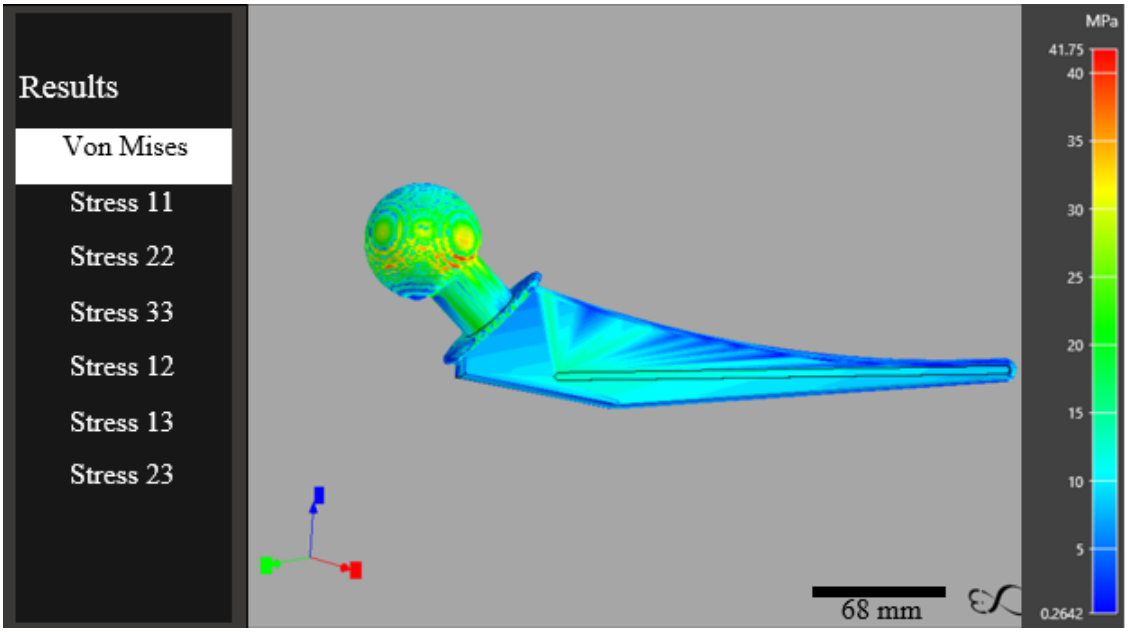

Figure 4.3: Simulated residual stress results

The influence of the specified FDM process parameters on the part deflection, residual stresses, and build time was studied according to Taguchi's L_{27} orthogonal array and are summarized in Table 4.2.

Table 4.2: Simulated results using Taguchi DoE

Run order	Printing temperature (°C)	Layer thickness(mm)	Print speed (mm/s)	Response Residual stresses (MPa)	Response Deflection (mm)	Response Build time (s)
1	255	0.1	30	49.86	3.474	145438
2	255	0.1	40	48.69	3.420	97805
3	255	0.1	50	47.59	3.368	74001
4	255	0.2	30	46.80	3.421	76738
5	255	0.2	40	44.87	3.318	51648
6	255	0.2	50	43.69	3.234	39108
7	255	0.3	30	45.23	3.393	55067
8	255	0.3	40	43.50	3.273	35156
9	255	0.3	50	41.75	3.175	28090
10	265	0.1	30	57.60	3.782	145438
11	265	0.1	40	56.18	3.722	97805
12	265	0.1	50	54.80	3.663	74001
13	265	0.2	30	53.87	3.728	74713
14	265	0.2	40	51.85	3.612	50269
15	265	0.2	50	50.56	3.521	38053
16	265	0.3	30	52.22	3.692	51871
17	265	0.3	40	50.24	3.558	34918
18	265	0.3	50	48.17	3.448	26446
19	275	0.1	30	65.62	4.103	145438
20	275	0.1	40	63.94	4.036	97805
21	275	0.1	50	62.33	3.969	74001
22	275	0.2	30	61.07	4.041	74713
23	275	0.2	40	59.09	3.914	50269
24	275	0.2	50	57.52	3.816	38053
25	275	0.3	30	59.54	4.002	51871
26	275	0.3	40	57.23	3.857	34918
27	275	0.3	50	54.70	3.738	26446

The results were then transformed into a signal-to-noise (S/N) ratio according to the "smaller the better quality" theorem, which prefers the least amounts of the part responses in this case the deflection, residual stresses, and build time. The S/N ratios were determined using Equation 3.6 and the results presented in Table 4.3. These results are discussed in the sections 4.1.1, 4.1.2 and 4.1.3.

Table 4.3: S/N Ratio for the transformed response results

Run order	Printing temperature (°C)	Layer thickness (mm)	Print speed (mm/s)	S/N, Residual stresses	S/N Deflection	S/N Build time
1	255	0.1	30	-33.9550	-10.8166	-103.2540
2	255	0.1	40	-33.7488	-10.6805	-99.8073
3	255	0.1	50	-33.5503	-10.5474	-97.3847
4	255	0.2	30	-33.4049	-10.6831	-97.7002
5	255	0.2	40	-33.0391	-10.4175	-94.2610
6	255	0.2	50	-32.8076	-10.1948	-91.8454
7	255	0.3	30	-33.1085	-10.6117	-94.8178
8	255	0.3	40	-32.7698	-10.2989	-90.9199
9	255	0.3	50	-32.4131	-10.0349	-88.9710
10	265	0.1	30	-35.2084	-11.5544	-103.2540
11	265	0.1	40	-34.9916	-11.4155	-99.8073
12	265	0.1	50	-34.7756	-11.2767	-97.3847
13	265	0.2	30	-34.6269	-11.4295	-97.4679
14	265	0.2	40	-34.2950	-11.1550	-94.0261
15	265	0.2	50	-34.0761	-10.9333	-91.6077
16	265	0.3	30	-34.3567	-11.3452	-94.2985
17	265	0.3	40	-34.0210	-11.0241	-90.8611
18	265	0.3	50	-33.6555	-10.7513	-88.4472
19	275	0.1	30	-36.3407	-12.2620	-103.2540
20	275	0.1	40	-36.1155	-12.1190	-99.8073
21	275	0.1	50	-35.8939	-11.9736	-97.3847
22	275	0.2	30	-35.7166	-12.1298	-97.4679
23	275	0.2	40	-35.4303	-11.8524	-94.0261
24	275	0.2	50	-35.1964	-11.6322	-91.6077
25	275	0.3	30	-35.4962	-12.0455	-94.2985
26	275	0.3	40	-35.1525	-11.7250	-90.8611
27	275	0.3	50	-34.7597	-11.4528	-88.4472

4.2.1 Effect of Process Parameters on Part Deflection

The response results for the S/N ratio analysis of the deflection is given in Table 4.4. These values were used to analyze the effect of the control parameters based on the delta statistics. The delta statistics were defined as the difference between the highest and the lowest values of the individual factors. Delta ranks were assigned based on these values where a higher delta value of 1.43 represented rank 1, the

second delta value of 0.45 represented rank 2, and the third delta value of 0.37 represented rank 3. The highest delta value represented the most influential factor on part deflection. According to the ranks obtained, printing temperature had the strongest effect on part deflection, with rank number 1, followed by the layer thickness and finally the print speed. This could be associated with printing temperature that significantly provide bonding between layers thereby, deflection. This could be associated with printing temperature that significantly provide bonding between layers thereby, deflection. Similar observation was made by Melo *et al.*(Vanaei et al., 2020), who observed that the changes in the nozzle temperature affected the material flow causing dimensional deviation.

Table 4.4: S/N Ratio results for the simulated part deflection

Level	**Printing temperature**	**Layer thickness**	**Print speed**
1	-10.48	-11.41	-11.43
2	-11.21	-11.16	-11.19
3	-11.91	-11.03	-10.98
Delta	1.43	0.37	0.45
Rank	1	3	2

The results in Table 4.4 were used to generate graphs for the effects of process parameters on the part deflection as shown in Figure 4.4.

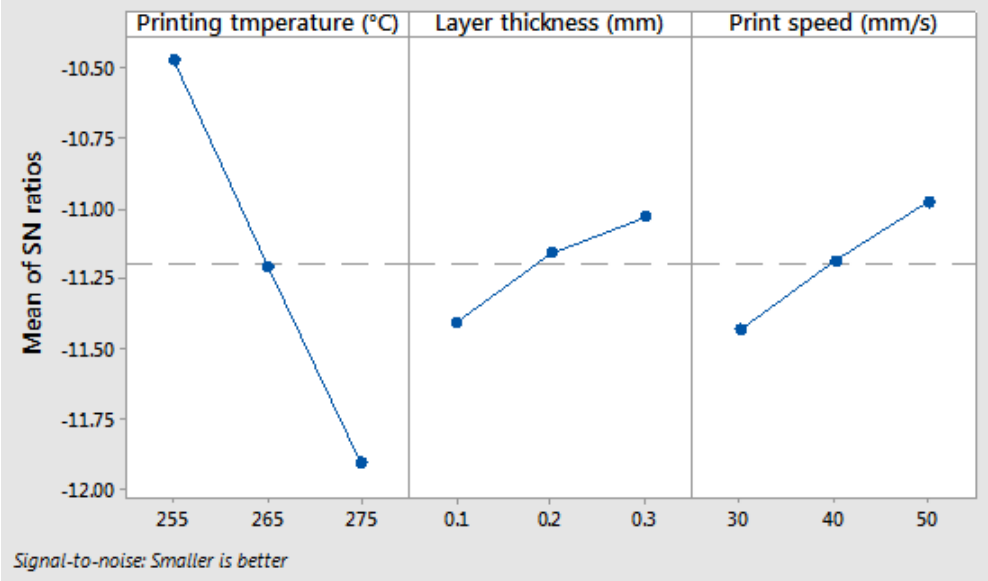

Figure 4.4: Effect of process parameters on part deflection

It is seen that part deflection decreased with decreasing printing temperature, increasing layer height, and increasing print speed. Increasing printing temperature was observed to increase part deflection. This is because when the printing temperature increases, the strength of the material deteriorates, and the softness increases leading to increased deflection.

Higher layer thicknesses were found to reduce part deflection due to the small heating and cooling cycles of subsequent layers with increasing layer thickness. Higher layer thickness resulted in fewer layers for model completion, leading to fewer heating and cooling cycles which resulted in low-temperature gradient and decreased part deflection. Similar observations have been reported by Santhakumar et al. (Santhakumar, Iqbal, & M.Prakash, 2017), who also noted reduced distortion effect and improved strength of the structure.

The print speed was inversely related to the part deflection. As the speed increased, the filament was extruded and deposited fast on the previously deposited layer before it cooled, resulting in low thermal gradient and hence minimal deflection. The higher

the printing speed, the lower the inter-layer cooling time. However, beyond the limiting print speed of 50 mm/s, increased vibration was experienced which led to poor surface finish of the printed part (Miazio, 2019).

From Table 4.4 and Figure 4.4, the first level of the printing temperature (255°C), the third level of layer thickness (0.3 mm), and the third level of print speed (50 mm/s) were the optimum process parameters required to minimize the part deflection in the printed hip joint implant.

From the ANOVA results presented in Table 4.5, printing temperature, layer thickness and print speed were found to have significant effect on the part deflection owing to their p-values which were less than 0.05. Table 4.4. Printing temperature had the highest effect on deflection with a contribution of 80.86%, followed by the print speed with 8.5%, and then the layer thickness with 5.94%. The interaction between parameters had no impact on the deflection because their percentage contribution was less than 1%. The percentage contribution informs about the effect of process parameters in order of impact. Therefore, a small change in printing temperature might result in a substantial change in deflection. Deflection may also be affected by a significant changes in print speed and layer thickness.

Table 4.5: ANOVA results for part deflection

Source	Degree of freedom	Sum of squares	Mean of squares	F-value	P-value	Contribution
A	2	0.1227	0.0613	765467.27	0.000	84.86%
B	2	0.0086	0.0043	53543.73	0.000	5.94%
C	2	0.0123	0.0061	76641.96	0.000	8.50%
A*B	4	0.0000	0.0000	9.75	0.004	0.00%
A*C	4	0.0000	0.0000	7.52	0.008	0.00%
B*C	4	0.0010	0.0003	3155.71	0.000	0.70%
Error	8	0.0000	0.0000			0.00%
Total	26	0.1446				100%

Where A is the printing temperature, B is the layer thickness, C is the print speed,

A*B is the interaction between the printing temperature and the layer thickness, A*C is the interaction of the printing temperature and the print speed, and B*C is the interaction of the layer thickness and the print speed.

4.2.2 Effect of Process Parameters on Residual Stresses

In the FFF process, the high-temperature gradients caused by the rapid heating and cooling cycles between subsequent layers were the main contributors to the induced residual stresses. The magnitude of the residual stresses in the printed part is related to the manufacturing process parameters. The impact of residual stresses is significant for the mechanical integrity of the manufactured parts. Understanding the effect of FFF process parameters on the residual stresses is, therefore, important to ascertain the mechanical behavior of FFFed parts. The process parameters had to be optimized to minimize these stresses in the printed part.

The response results for the S/N ratio analysis of the residual stress is given in Table 4.6. The printing temperature had the highest influence on the residual stress, with delta value of 2.37. The layer thickness was the second with delta value of 0.98, followed by the print speed, with delta value of 0.57.

Table 4.6: S/N results for simulated residual stress

Level	Printing temperature	Layer thickness	Print speed
1	-33.2	-34.95	-34.69
2	-34.45	-34.29	-34.4
3	-35.57	-33.97	-34.13
Delta	2.37	0.98	0.57
Rank	1	2	3

The S/N ratios results from Table 4.6 were used to generate graphs for the effect of process parameters on the residual stresses as shown in Figure 4.5.

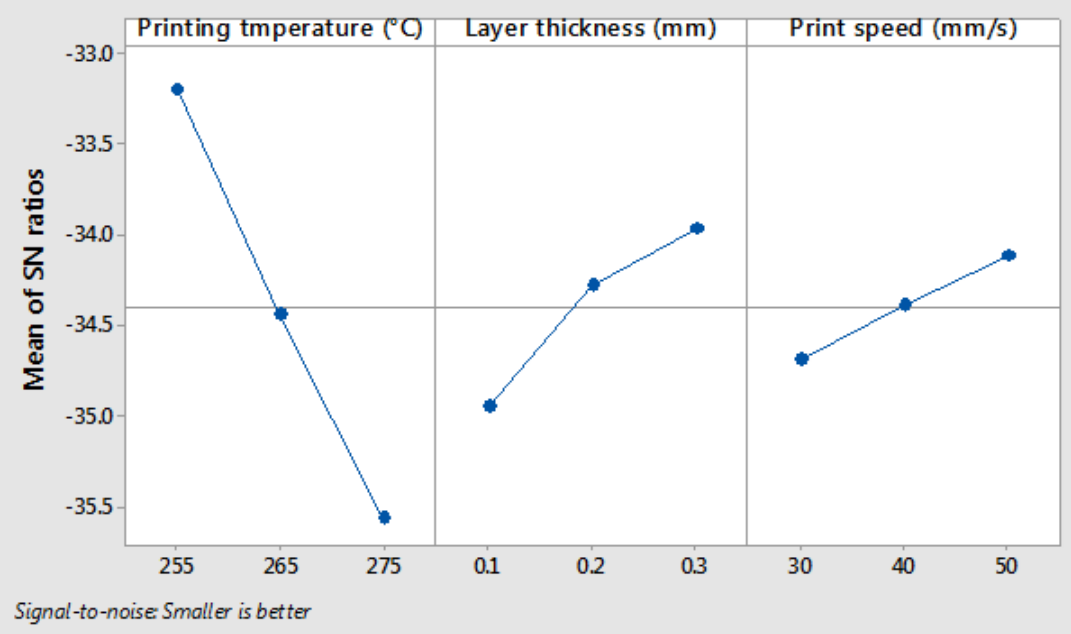

Figure 4.5: Effect of process parameters on residual stresses

It can be seen that the residual stress decreased with decreasing printing temperature, increasing layer thickness and increasing print speed. High printing temperature caused more accumulation of residual stress in the printed parts. The increased printing temperature cause more energy absorption at the contact of extruded filament, which caused a larger area of the deposited layer to be reheated and result in a high thermal gradient (Tang et al., 2020). Reducing printing temperature from 275 ^{0} C to 255 ^{0}, reduces the fluidity of the filament. Therefore, causing better bonding between layers leading to high part strength. Whereas increasing layer thickness reduced the residual stresses, the number of layers required to complete the model reduced, yielding a lower thermal gradient. Increasing print speed was observed to reduce the residual stresses since faster filament deposition enhanced reduced reheating area of the deposited filament. Thus, the overall cooling rate was reduced, resulting in minimized residual stresses in the printed part.

From Table 4.6 and Figure 4.5, the optimal condition was determined as: printing temperature of 255°C, layer thickness 0.3 mm, and print speed of 50 mm/s. These

values were the optimum process parameters required to minimize the residual stresses in the printed hip joint implant.

Table 4.7 shows ANOVA results for residual stresses. From the Table, printing temperature, layer thickness, and print speed had a significant impact on the residual stresses since their p-values were less than 0.05. Printing temperature had the highest effect on the residual stresses with a contribution of 80.7%, followed by the layer thickness with 14.48%, and print speed with 4.6%. The interaction between parameters had no effect on the residual stresses since their relative percentage contributions were less than 1%. Higher temperatures increase the fluidity of the filament, allowing it to stretch more freely and resulting in higher dimensional variations (Frunzaverde et al., 2022). The layer thickness and print speed also affect the residual stresses. However, the influence was lesser than that of the printing time.

Table 4.7: ANOVA results for the simulated residual stresses

Source	Degree of freedom	Sum of squares	Mean of squares	F-value	P-value	Contribution
A	2	0.3345	0.16730	37052.11	0.000	80.70%
B	2	0.0600	0.03000	6649.30	0.000	14.48%
C	2	0.0191	0.00950	2110.70	0.000	4.60%
A*B	4	0.0000	0.00000	0.11	0.977	0.00%
A*C	4	0.0000	0.00000	0.31	0.863	0.00%
B*C	4	0.0009	0.00020	47.61	0.000	0.21%
Error	8	0.0000	0.00000			0.01%
Total	26	0.4145				100%

4.2.3 Optimum Parameters for Build Time

Build time is an important characteristic for maximizing the production cost for FDM printer. Analyzed signal-to-noise ratios for build time were obtained to identify the optimum processing parameters. The results are presented in Table 4.8. Depending on the rank obtained, it can be seen that the build time was highly influenced by the

layer thickness, followed by the print speed, and printing temperature. The main effect plots for the signal-to-noise ratios on the build time are shown in Figure 4.6. From Table 4.8 and Figure 4.6, the optimal parameter levels required to minimize build time were printin temperature of 265°C, layer thickness of 0.3 mm, and print speed of 50 mm/s.

Table 4.8: Signal to noise ratio results for build time

Level	Printing temperature	Layer thickness	Print speed
1	-95.44	-100.15	-98.42
2	-95.24	-94.45	-94.93
3	-95.24	-91.32	-92.56
Delta	0.2	8.82	5.86
Rank	3	1	2

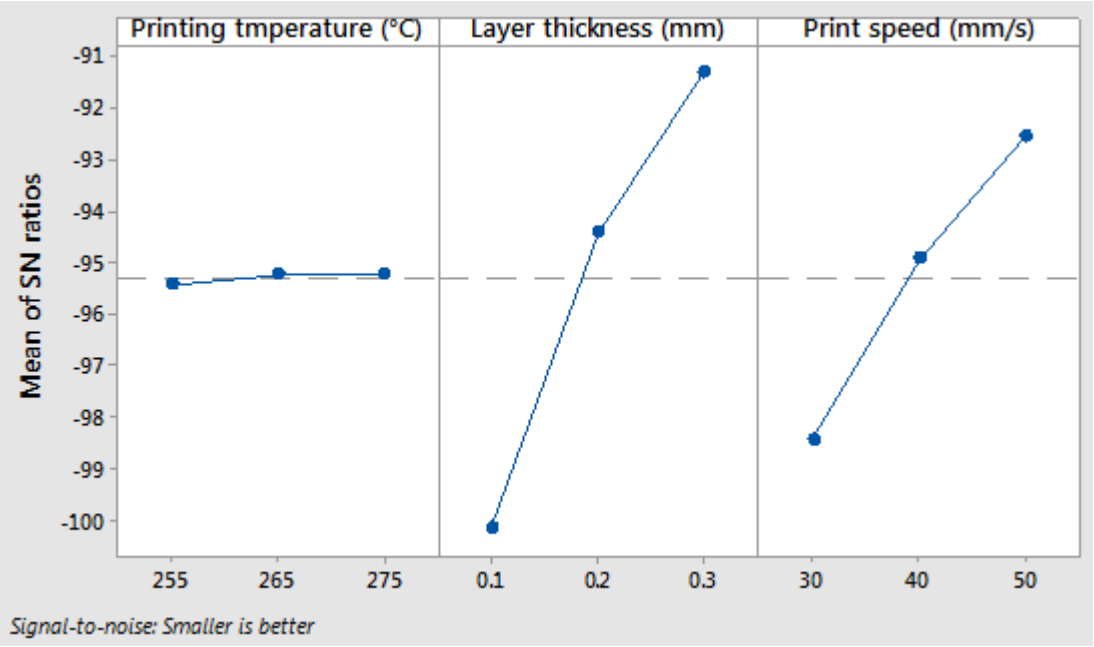

Figure 4.6: Effect of process parameters on Build Time

The ANOVA results for the build-time values are shown in Table 4.9. From the table, layer thickness with a contribution of 56.9 % has the strongest impact on build time. The other factors having minimal contribution. The relevance of layer

thickness is related to build time, with the higher layer thickness, the shorter build time. When layer thickness increases, the tensile bond strength increases and the build time decreases (Liu et al., 2020).

Table 4.9: ANOVA results for build time

Source	Degree of freedom	Sum of squares	Mean of squares	F-value	P-value	Contribution
A	2	$7.1X10^{16}$	$3.5X10^{20}$	12.73	0.003	0.01%
B	2	$5.7X10^{20}$	$2.9X10^{20}$	102852.15	0.000	56.90%
C	2	$2.6X10^{20}$	$1.3X10^{20}$	46798.69	0.000	25.89%
A*B	4	$3.6X10^{16}$	$9.0X10^{15}$	3.25	0.073	0.00%
A*C	4	$3.5X10^{16}$	$8.7X10^{15}$	3.13	0.079	0.00%
B*C	4	$1.7X10^{20}$	$4.3X10^{19}$	15536.75	0.000	17.19%
Error	8	$2.2X10^{16}$	$2.8X10^{15}$			0.00%
Total	26	$1.0X10^{21}$				100.00%

Where A is the printing temperature, B is the layer thickness, C is the print speed, A*B is the interaction between the printing temperature and the layer thickness, A*C is the interaction of the printing temperature and the print speed, and B*C is the interaction of the layer thickness and the print speed.

4.3 Multi-objective Optimization Results and Discussion

As already explained, the optimum parameter levels for part deflection, residual stresses, and build time were different. In practice, hip joint implants are manufactured at the same optimal levels. For this reason, it was necessary to find the optimized process parameters that result in minimal part deflection (D), residual stresses (RS), and build time (PT) during 3D printing of the part. In order to achieve this, all the responses were transformed into a single response called grey relational grade (GRG), with a higher value indicating better results. The normalized values and deviation sequences as calculated in Equations 3.9 and 3.11 respectively, are shown in Table 4.10.

Table 4.10: Normalized values and deviation sequence results

Exp. No	Normalized values			Deviation Sequences		
	RS	D	PT	Δ_{01}	Δ_{02}	Δ_{03}
1	0.6602	0.6778	0.0000	0.3398	0.3222	1.0000
2	0.7093	0.7360	0.4003	0.2907	0.2640	0.5997
3	0.7553	0.7920	0.6004	0.2447	0.2080	0.3996
4	0.7884	0.7349	0.5774	0.2116	0.2651	0.4227
5	0.8693	0.8459	0.7882	0.1307	0.1541	0.2118
6	0.9187	0.9364	0.8936	0.0813	0.0636	0.1064
7	0.8542	0.7651	0.7595	0.1458	0.2349	0.2405
8	0.9267	0.8944	0.9268	0.0733	0.1056	0.0732
9	1.0000	1.0000	0.9862	0.0000	0.0000	0.0138
10	0.3360	0.3459	0.0000	0.6640	0.6541	1.0000
11	0.3955	0.4106	0.4003	0.6045	0.5894	0.5997
12	0.4533	0.4741	0.6004	0.5467	0.5259	0.3996
13	0.4923	0.4041	0.5944	0.5078	0.5959	0.4056
14	0.5769	0.5291	0.7998	0.4231	0.4709	0.2002
15	0.6309	0.6272	0.9025	0.3691	0.3728	0.0975
16	0.5614	0.4429	0.7863	0.4386	0.5571	0.2137
17	0.6443	0.5873	0.9288	0.3557	0.4127	0.0712
18	0.7310	0.7058	1.0000	0.2690	0.2942	0.0000
19	0.0000	0.0000	0.0000	1.0000	1.0000	1.0000
20	0.0704	0.0722	0.4003	0.9296	0.9278	0.5997
21	0.1378	0.1444	0.6004	0.8622	0.8556	0.3996
22	0.1906	0.0668	0.5944	0.8094	0.9332	0.4056
23	0.2736	0.2037	0.7998	0.7264	0.7963	0.2002
24	0.3393	0.3093	0.9025	0.6607	0.6907	0.0975
25	0.2547	0.1088	0.7863	0.7453	0.8912	0.2137
26	0.3515	0.2651	0.9288	0.6485	0.7349	0.0712
27	0.4575	0.3933	1.0000	0.5425	0.6067	0.0000

Results for the grey relational coefficients and their averages as calculated using Equations 3.10 and 3.12, respectively are presented in Table 4.10. Since the optimized GRG should be equivalent to all the optimized quality responses considered, the optimum process parameter levels are derived from the highest GRG (0.9910) as shown in the Table 4.11.

Table 4.11: Grey relational coefficients and GRG results

	Grey Relational Coefficient					
Exp. No	**RS**	**D**	**PT**	**GRG**	**S/N ratio**	**Order**
1	0.5954	0.6081	0.3333	0.5123	-5.8097	21
2	0.6323	0.6544	0.4547	0.5805	-4.7243	16
3	0.6714	0.7062	0.5558	0.6445	-3.8157	10
4	0.7027	0.6535	0.5419	0.6327	-3.9760	11
5	0.7928	0.7644	0.7024	0.7532	-2.4617	5
6	0.8602	0.8872	0.8245	0.8573	-1.3374	3
7	0.7742	0.6804	0.6752	0.7099	-2.9757	6
8	0.8721	0.8256	0.8723	0.8567	-1.3436	2
9	1.0000	1.0000	0.9731	0.9910	-0.0782	1
10	0.4295	0.4332	0.3333	0.3987	-7.9869	25
11	0.4527	0.4590	0.4547	0.4554	-6.8315	22
12	0.4777	0.4874	0.5558	0.5070	-5.9007	18
13	0.4962	0.4562	0.5521	0.5015	-5.9946	20
14	0.5416	0.5150	0.7141	0.5902	-4.5795	13
15	0.5753	0.5728	0.8368	0.6616	-3.5876	9
16	0.5327	0.4730	0.7006	0.5688	-4.9014	14
17	0.5843	0.5478	0.8754	0.6692	-3.4893	7
18	0.6502	0.6296	1.0000	0.7599	-2.3845	4
19	0.3333	0.3333	0.3333	0.3333	-9.5424	27
20	0.3497	0.3502	0.4547	0.3849	-8.2938	26
21	0.3671	0.3688	0.5558	0.4306	-7.3194	23
22	0.3819	0.3489	0.5521	0.4276	-7.3790	24
23	0.4077	0.3857	0.7141	0.5025	-5.9775	17
24	0.4308	0.4199	0.8368	0.5625	-4.9978	15
25	0.4015	0.3594	0.7006	0.4872	-6.2463	19
26	0.4353	0.4049	0.8754	0.5719	-4.8542	12
27	0.4796	0.4518	1.0000	0.6438	-3.8250	8

The response table for the GRG, (see Table 4.12), illustrates the priority of the parameters that influence the process. The results showed that printing temperature had the highest influence on the multi-response with delta value of 3.546 than others as shown Table4.12. The optimal parameter levels were those that had the highest grey relational grade value. From Figure 4.7 and Table 4.12, the optimum parameter levels for multiple response were printing temperature 255°C, layer thickness of 0.3 mm, and print speed of 50 mm/s. The S/N ratios for grey relational grade are shown

in Table 4.11. The highest S/N for GRG was -0.0782, which showed that the optimal process parameters corresponded to the highest S/N ratio were: printing temperature 255 °C, layer thickness of 0.3 mm, and print speed of 50 mm/s. These two techniques gave the desirable parameters required to minimize deflection, residual stresses and build time simultaneously.

Table 4.12: Signal to noise ratio results for GRG

Level	Printing temperature	Layer thickness	Print speed
1	-2.947	-6.692	-6.09
2	-5.073	-4.477	-4.728
3	-6.493	-3.344	-3.694
Delta	3.546	3.347	2.396
Rank	1	2	3

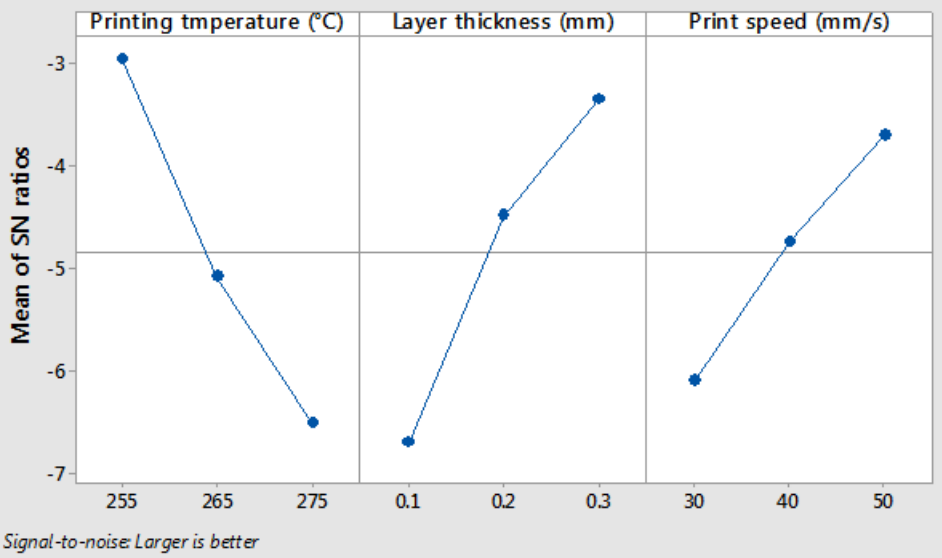

Figure 4.7: Effect of process parameters on GRGs

Figure 4.8 shows the interaction among the selected input parameters for the GRG. Interaction effect gives important information on how two variables work together to affect the output response. The interaction effect can be obtained by evaluating the non-parallel and parallel lines in the plot (Panda & Singh, 2013). However, the interaction plot does not reveal if the interaction is statistically significant on the model (Panda & Singh, 2013). The interaction plot shows that printing temperature

and layer thickness interact at some point, their interaction is weak as the lines are nearly parallel to each other. Therefore, as the printing temperature increases, GRG fell more in higher thickness compared to low thickness. It was revealed that simultaneously increasing the printing temperature and layer thickness caused an increase in GRG. Similar trends were observed in the interaction between layer thickness and print speed. Since these parameters produced similar effects on the GRG, there was no interaction.

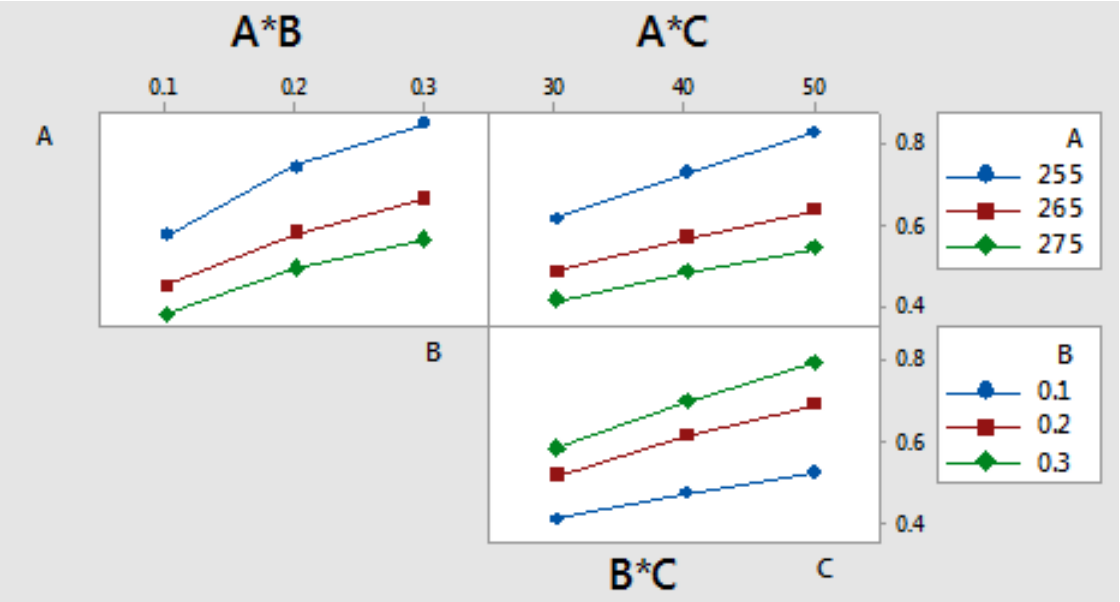

Figure 4.8: Interaction plot for GRG

ANOVA results are shown in Table 4.13. The results shows that printing temperature had the highest influence with percentage contribution of 41.27 % and a p-value of 0. The layer thickness had a percentage contribution of 39.29 % and a p-value of 0. The print speed had a percentage contribution of 18.95 % with a p-value of 0. The relative percentage contribution of the interaction between printing temperature and layer thickness was less than 1%. Interaction between printing temperature and print speed and layer thickness and print speed did not affect the GRG because their p-values were greater than 0.05. The p-value results were also supported by the mean

squares and F-values. As seen in Table 4.13, the greater the mean square or F-value, the larger the effect. Therefore, the printing temperature was strongly associated with residual stresses and deflection. Thus, printing temperature negatively affect the adhesion between layers, which in turn affect the quality of the printed parts (Le, Rabsatt, Eisazadeh, & Torabizadeh, 2022). The higher layer height favored achieving higher mechanical properties (Bakhtiari, Aamir, & Tolouei-Rad, 2023). The print speed also significantly affected residual stresses, deflection and build time. Printing speed causes the filaments to be in contact with the hot nozzle (Hsueh et al., 2021).. When the filaments are subjected to high temperatures, thermal degradation occurs in deposited layers, resulting in lowered mechanical properties (Hsueh et al., 2021).

Table 4.13: ANOVA results for GRG

Source	Degree of freedom	Sum of squares	Mean of squares	F-value	P-value	Contribution
A	2	0.329	0.165	3491.830	0.000	41.27%
B	2	0.314	0.157	3324.370	0.000	39.29%
C	2	0.151	0.076	1603.490	0.000	18.95%
A*B	4	0.003	0.001	15.630	0.001	0.37%
A*C	4	0.001	0.000	2.950	0.090	0.07%
B*C	4	0.000	0.000	0.340	0.847	0.01%
Error	8	0.000	0.000			0.05%
Total	26	0.798				100%

Using the regression feature in Minitab-18, a relationship was obtained between the input variables (printing temperature, layer thickness, and print speed) and the multi-response (GRG). The interaction between parameters were removed from the regression model because they did not affect the multi-response, as illustrated by the ANOVA results in Table 4.13. The GRG equation is given by:

$$GRG = 3.915 - 0.020A + 1.927B + 0.014C \tag{4.1}$$

Where A is the printing temperature (°C), B is the layer thickness (mm), and C is the print speed (mm/s).

Equation 4.1 is the objective function that was maximized using genetic algorithm optimization technique. The presented relationship can also be used to forecast the estimated value of grey relational grade (responses) for the chosen input parameters.

Contour plots were generated to help determined effect of factors on grey relational grade. Higher GRG corresponded to the minimal deflection, residual stresses and build time concurrently. Figure 4.9 shows the contour plot for GRG versus printing temperature and layer thickness. The contours were found to be in varied ranges depending on the GRG. It is noted that, an increase in layer thickness while printing temperature is kept constant will result in an increase in GRG from 0.4 to 0.9. To achieve a GRG of more than 0.9, the printing temperature should be in the range of 255 °C to 256 °C, and the layer thickness should be in the range of 0.24 mm and 0.30 mm, as indicated in Figure 4.9.

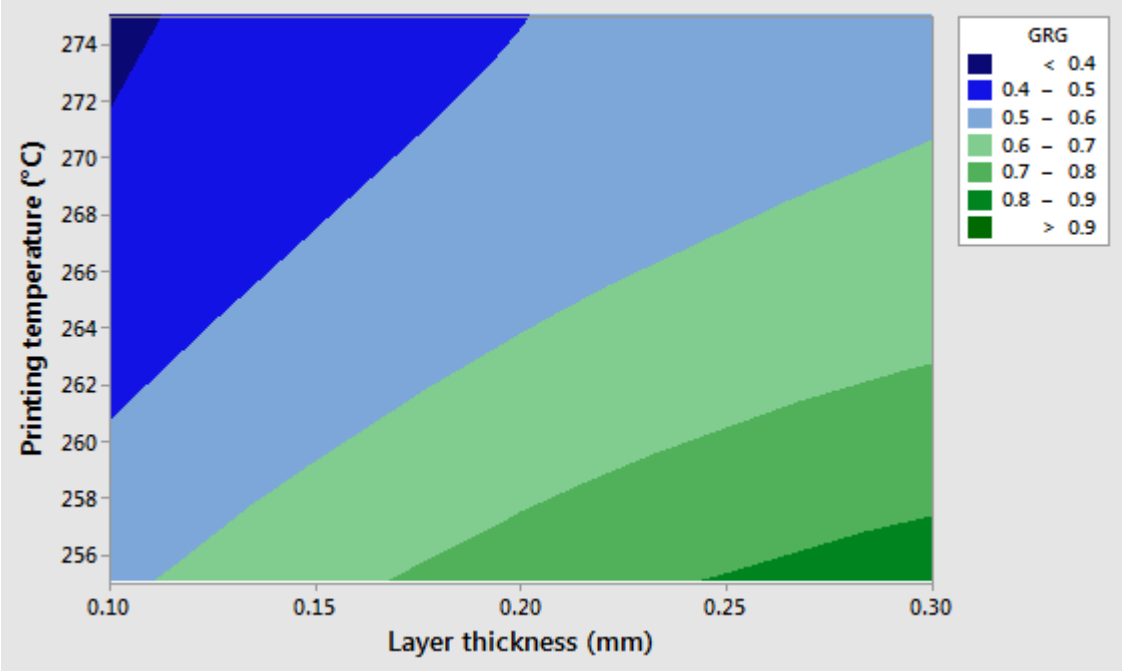

Figure 4.9: Contour plot for GRG versus printing temperature and layer thickness

Contour plot for the grey relational grade versus printing temperature and print

speed is shown in Figure 4.10. It is noted that, an increase in printing temperature, while print speed is kept constant will result in a decrease in GRG from 0.9 to 0.4. Increase in print speed, while printing temperature is kept constant will result in a decrease in GRG from 0.9 to 0.4. To achieve a GRG of more than 0.9, the printing temperature should be in the range of 255 °C to 256 °C and the print speed should be in the range of 47.5 mm/s and 50 mm/s, as indicated in Figure 4.10.

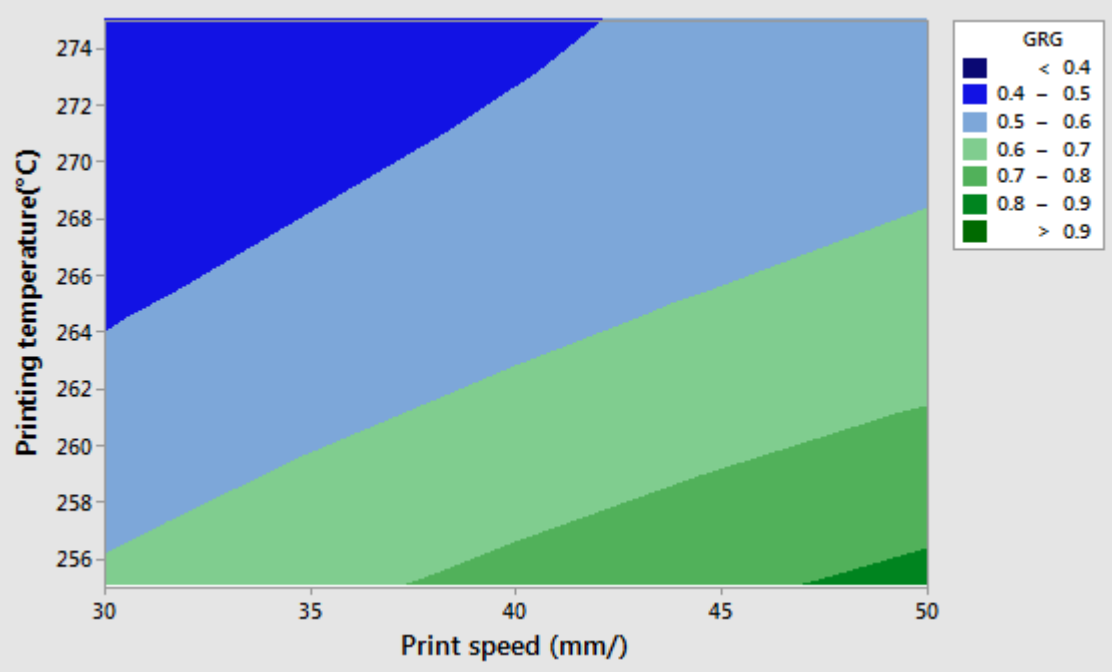

Figure 4.10: Contour plot for GRG versus printing temperature and print speed

Contour plot for the grey relational grade versus layer thickness and print speed is shown in Figure4.11. It is noted that, an increase in layer thickness, while print speed is kept constant will result in an increase in GRG from 0.4 to 0.9. An increase in print speed, while layer thickness is kept constant will result in an increase in GRG from 0.4 to 0.9. To achieve a GRG of more than 0.9, the layer thickness should be in the range of 40 mm/s to 50 mm/s, and the print speed should be in the range of 0.21 mm and 0.3 mm, as indicated in Figure 4.11.

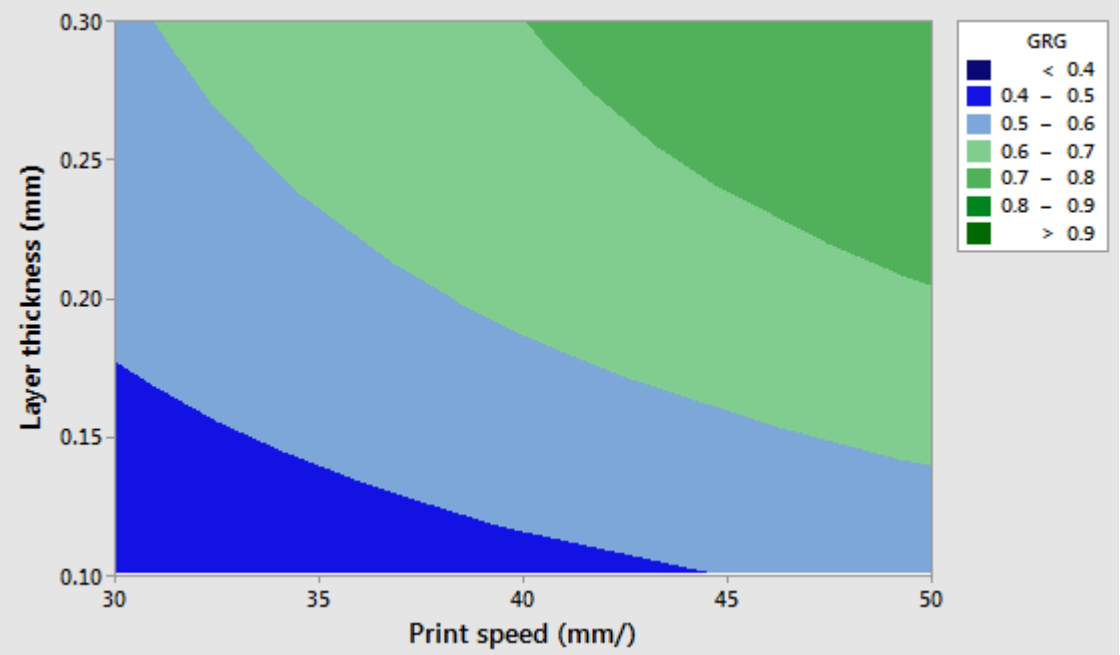

Figure 4.11: Contour plot for GRG versus layer thickness and print speed

4.4 Optimization Using GA Results

A genetic algorithm code (Figure A.1) was used for optimization of selected FDM process parameters. The objective function, Equation 4.1 was used with GA code in MATLAB to obtain optimized parameter levels for simultaneous minimization of the multi-response and the results shown in Table 4.14. These results were similar to those obtained using the Taguchi grey relational analysis with zero variance.

Table 4.14: Optimum process parameter results

Parameter	Optimal Value
Printing temperature (°C)	255
Layer thickness (mm)	0.3
Printing speed (mm/s)	50

An objective function with all interactions was developed as shown in Equation 4.2 and used in the GA code to check the interaction effect on the output. Results

indicated similar optimum parameter levels.

$$GRG = 3.66 - 0.01901A + 0.63B + 0.0237C + 0.0027AB - 0.000048AC + 0.0147BC \tag{4.2}$$

Where A is the printing temperature (°C), B is the layer thickness (mm), and C is the print speed (mm/s). Therefore, the presented relationship can be used to predict the estimated GRG for selected input process parameters.

4.5 Confirmation Test

A confirmation test was conducted to ascertain the optimality of the parameters. This was done by comparing optimization results obtained using three optimization techniques which were: Taguchi GRA, basic Taguchi optimization and GA. The aim of the optimization was to minimize all the responses simultaneously (deflection, residual stresses, and build time). The findings of these three methods are shown in Table 4.15. Using GRA, the optimal parameters were: a printing temperature of 255 °C, a layer thickness of 0.3 mm, and a print speed of 50 mm/s. Thereafter, the GRG was used as a single response for basic Taguchi optimization. Based on the S/N ratio for GRG, the optimal parameters obtained were the same as those using GRA. The findings of GA were also the same as those of the two preceding methods. An inspection of the optimization results from GRA and S/N in Table 4.11 showed that the values of the response studied were minimum in all their respective data sets. For instance, the deflection of 3.175 mm, residual stress of 41.75 MPa, and a build time of 28,090 seconds were the least in their respective columns. This means that the optimal response obtained using the three optimization techniques were in good agreement. Similar findings have been obtained by other researchers (Simiyu et al., 2023; Y. Zhang & Chou, 2006b).

Table 4.15: Comparison of optimization techniques

Technique	Optimal Parameter Levels				Responses	
	A (°C)	B (mm)	C (mm/s)	D (mm)	RS (MPa)	BT (s)
GRA	255	0.3	50	3.175	41.75	28,090
Basic Taguchi method	255	0.3	50	3.175	41.75	28,090
Genetic Algorithm	255	0.3	50	3.175	41.75	28,090

4.6 Experimental Results

4.6.1 Part Deflection and Printing Time

The final dimension of the femoral head after 3D printing, part deflection results and time taken to print the hip joint implants are presented in Table 4.16.The average part deflection was 2.91 mm. This meant that the part must be overdesigned by 2.91 mm before 3D printing so as to the exact dimensions. The minimum time required to print CF/PA12 hip joint implant was found to be 29385 seconds(8hours and 6minutes).

Table 4.16: Part deflection and printing time results

Exp. No	Initial implant size (mm)	Final implant size (mm)	Deflection (mm)	Build time (s)
1	49.5	46.6	2.9	29563
2	49.5	46.58	2.92	29217
3	49.5	46.59	2.91	29374
Average	49.5	46.59±0.008	2.91±0.008	29,385±141

4.6.2 Residual Stresses

The tensile and compressive residual stress measurements were done from the surface to a depth of 1 mm. The stresses were calculated by considering a distribution of 20 constant steps within the 1 mm depth. A new data set was obtained after every 0.05 mm and the results recorded in Table B.1. These results were used to

generate the residual stress distribution as shown in Figure 11 where the red and blue curves indicate tensile and compressive residual stresses, respectively. As indicated in the earlier work (Maxwell & Turnbull, 2003), engineering thermoplastics have been reported to exhibit both tensile and compressive surface stresses.

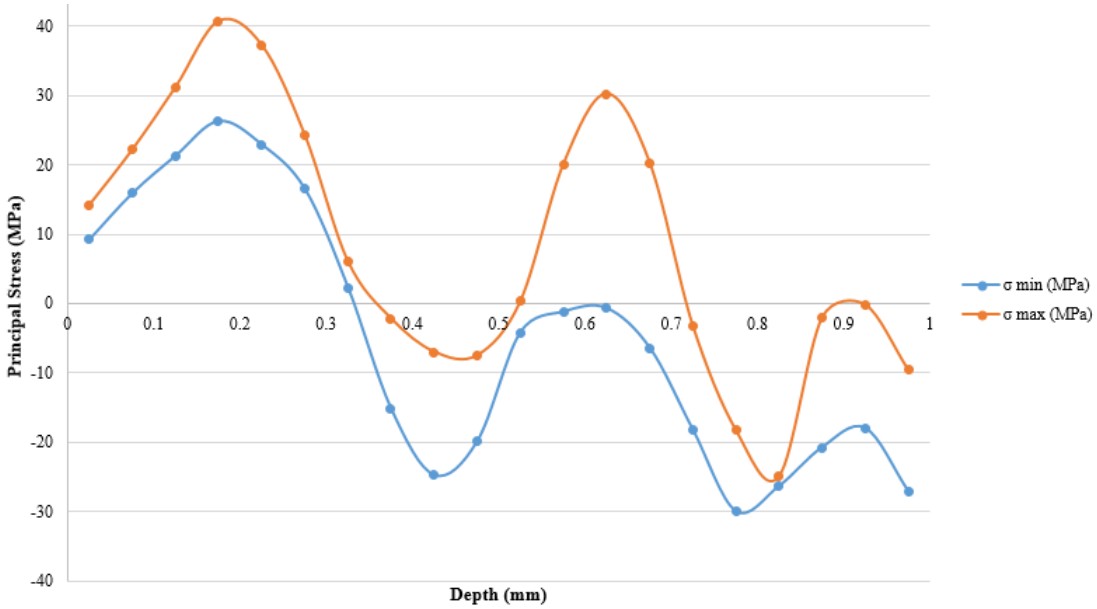

Figure 4.12: Variation of principle stresses with depth

This stress distribution occurred due to the layering process where the added new layer starts to cool down faster than the deposited layers of the part, resulting in tensile stresses in the new layer and compressive stress in the lower layer. Subsequent heating and cooling of layers during the FDM process causes the part to shrink due to thermal contraction. Consequently, tensile residual stresses are formed in the printed part and balanced by compressive stresses as illustrated in Figure 4.12. Tensile residual stresses are undesirable since they tend to promote initiation and growth of cracks that are responsible for the part failure. In contrast, compressive residual stresses are desirable as they tend to delay crack initiation and growth which prevents part failure, hence increasing its strength.

Indeed, residual stress is a balancing act in which compressive stresses compensate

for tensile stresses within the component Khmyrov, Kotoban, and Gusarov (2016). The magnitude of the tensile stresses varied from 0.3 MPa to (40.7±11.8) MPa, while compressive residual stresses varied from -0.2 MPa to (-30 ±9.7) MPa. The unbalanced residual stresses in the maximum principal stress curve were (15.7±2.1) MPa, while tensile residual stresses in minimum principal stress curve were all compensated by compressive residual stresses. This meant that the total minimum amount of tensile residual stress in the printed part was (15.7±2.1) MPa. This value was obtained at a printing temperature of 255°C, a layer thickness of 0.3 mm, and a print speed of 50 mm/s. Mechanical strengths of the manufactured hip implant were then determined to check maximum stresses that the component could resist.

4.7 Validation of Simulation Results

The simulation results obtained from the Digimat 2020 AM software were validated using data from experimental work. Experimental and simulations results for the part deflection, residual stresses and printing time were compared as shown in Table 4.17.

Table 4.17: Comparison of simulated and experimental results

Responses	**Simulated values**	**Experimental values**	**Deviation (%)**
Part deflection (mm)	3.175±0.266	2.91±0.008	8.34±0.38
Residual stresses (MPa)	41.75±6.5	40.7±11.8	2.51±0.04
Build time (s)	28090	29385±141	4.61±0.10

From the table, simulated results for the part deflection, residual stresses, and printing time had a relatively good agreement with the experimental values. The error margins were (8.34 ±0.38) %, ((2.51±0.04) %, and (4.61±0.10) %. The general percent difference between the simulation and experimental results was less than 13%, indicating acceptable agreement Zhou, Hsieh, and Sun (2017). Hence, the errors in this study is therefore considered acceptable.

4.8 Surface Roughness

The surface morphology of the hip implant can be classified as a function of its roughness (Ra) i.e., smooth surfaces (Ra = 0–0.5 μm), minimally rough (Ra = 0.5–1 μm), moderately rough (Ra = 1–2 μm), and highly rough surfaces (Ra > 2μm) Albrektsson and Wennerberg (2004). According to the ISO 7206-2 standards *ISO 7206-2, Implants for Surgery* (2011) for surgery implants, the maximum permissible surface roughness value is 2 μm. The average measured surface roughness values were: femur (1.51±0.47) μm, femoral neck (1.57±0.07)μm, and femoral head (1.61±0.07) μm surfaces of the manufactured hip implant, as shown in Table 4.18. These results indicated surface roughness values of the manufactured implant fall within the recommended standard.

Table 4.18: Surface roughness results

No. of points	**Ra for femur (±0.47μm)**	**Ra neck (±0.07 μm)**	**Ra for head (±0.07 μm)**
1	1.11	1.71	1.51
2	1.18	1.73	1.58
3	2.28	1.68	1.7
4	1.16	1.78	1.6
5	1.84	1.57	1.69
Average	1.51	1.57	1.61

The surface texture for hip implants achieved in this study is preferable over a smooth surface as it enhances osseointegration between the bone and the implant surface which results in long life. Dong et al. (H. Dong et al., 2020),reported simular results that rough-surfaced implants had a higher percentage of bone-to-implant contact rate than those with a smooth surface. The use of rough surfaces has also been encouraged because they enhance the bonding strength of the stem–cement interfacial bond (Datir & Wynn-jones, 2005). The rough surface increases bone-to-implant contact and enhances the removal of torque forces, which contributes to the initial and long-term stability of implants (Datir & Wynn-jones, 2005).

4.9 Tensile Test

The primary goal of the tensile testing is to investigate how well fused deposition modeling (FDM) technique could produce a CF/PA12 composite hip joint implant. Besides good biocompatibility and processability, the manufactured CF/PA12 hip implant should have sufficient strength to withstand the static loading (body weight) experienced. Even though the body weight primarily applies compression load on the implant, during action the implant will fail in tension. For this reason, the mechanical properties of the printed CF/PA12 composite hip implant were compared to those of the cortical bone. Since this composite is designed to replace the hip joint, the ultimate goal is to have identical mechanical properties to those of the cortical bone to minimize stress shielding and, ultimately bone resorption. The elastic modulus, tensile strength, and percentage elongation at fracture of the human cortical bone range from 7–30 GPa, 50–150 MPa, and 1–3%, respectively as reported in (C. Liao & Li, 2020; Rahim et al., 2017).

Figure 4.13 shows stress-strain curves for all the specimens tested. From these curves, the ultimate tensile strength (UTS), Young's modulus, and maximum elongation were determined. The results are presented in Table Table 4.19.

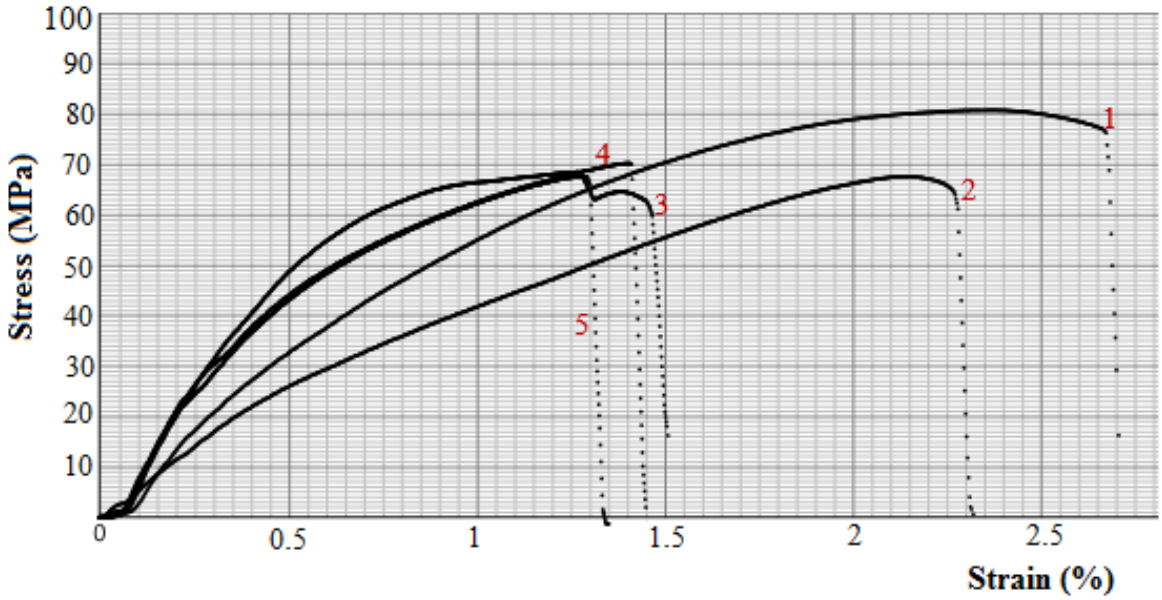

Figure 4.13: Stress-strain curves of the 3D printed hip joint implant

Table 4.19: Results from tensile tests

No. of Exp.	Tensile Strength (±4.80 MPa)	Percentage Elongation (±0.54 %)	Modulus of Elasticity (±0.22 GPa)
1	69.4	1.35	7.5
2	70	1.45	7.6
3	69	1.5	7.5
4	68	2.3	7.2
5	81	2.7	7.9
Average	71.48	1.86	7.54

The mechanical properties of the hip implant were: the ultimate strength (71.48±4.80) MPa, Young's modulus (7.54±0.22) GPa, and percentage elongation (1.86±0.54)%. These results were compared with those of the cortical bone found in the human femur, as shown in Table 4.20. The results indicated that the strength, Young's modulus and percentage elongation of the CF/PA12 composite were within the recommended range for the human femur tensile strength of 50-150MPa, Young's modulus of 7–30 GPa, and percentage elongation of 1–3%.

Table 4.20: Tensile properties comparison

Property	3Dprinted	Cortical bone
Tensile strength (MPa)	(71.48±4.80)	50-150
Young's modulus (GPa)	(7.54±0.22)	7–30
Percentage elongation (%)	(1.86±0.54)	1–3

Therefore, the artificial hip implant developed in this study should be considered as a suitable candidate for medical trial tests. The results have shown that tensile properties are within the desired range for the cortical in the femur bone. The results obtained highlighted the benefits of substituting the one with fiber-reinforced polymer composites instead of metallic alloys. The metallic implants have been shown to have higher mechanical properties than the cortical bone, which leads to premature failure of the implant (Apostu et al., 2018). These results should therefore be considered for making composite hip implants.

The fracture surfaces of the specimens after tensile testing were observed using SEM. The image showed the presence of carbon fibers at the fracture of the specimen, as illustrated in Figure 4.14. The fracture surfaces of the tensile specimens were brittle due to debonding of carbon fibers with nylon 12 matrix. From Figure 4.14 a), it is noted that carbon fibers were mainly pulled out of the matrix at the fracture interface of the specimen which could be attributed to the poor interfacial strength between the fiber and the nylon 12 matrix. These carbon fibers do not seem to have broken with the fracture of the matrix during tensile testing. Furthermore, the stresses encountered during the tensile test may be insufficient to produce fiber failure even if the stresses in the fibers increase due to load transfer from the matrix. Hence, causing fibers to be pulled out of the matrix rather than fracturing. Some voids were observed in Figure 4.14 a) that could be attributed to the fiber pull-out. Figure 4.14 b) showed that some carbon fibers were ruptured at the fracture interface of the specimen. This could be due to a strong interbonding between the layers that resulted in high tensile strength. Hence, providing a stronger fracture path.

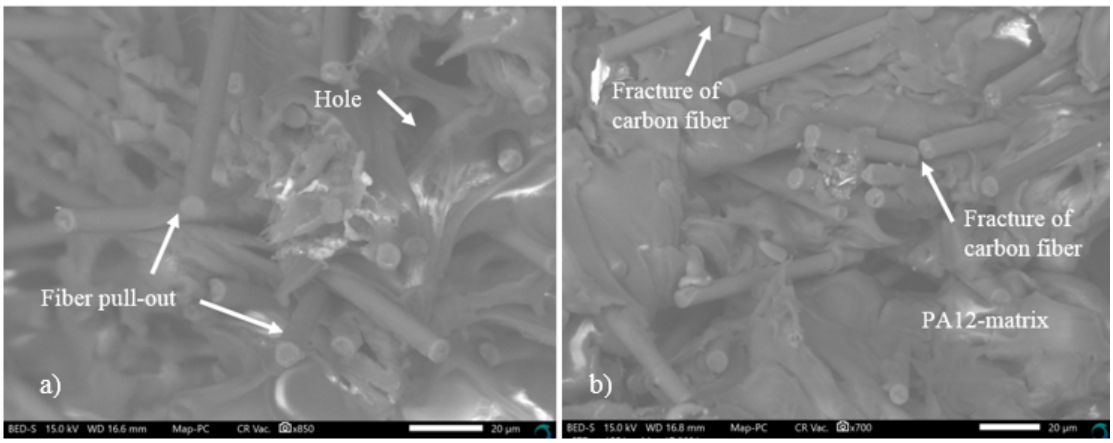

Figure 4.14: Fracture surface image of the tensile specimen

4.10 Compression Test Results

The hip implant is subjected to compressive loads; therefore it is essential to obtain the compressive strength of the 3D printed CF/PA12 hip implant to ensure resistance of the component to similar loading conditions. Compression results are shown in Figure 4.15. The maximum compressive strength of the artificial hip implant was compared to that of the cortical bone in the femur, as shown in Table 4.21. The compression strength result was 135.8 MPa. This result was within the reported range of the compressive strength of the femur bone (100-230) MPa (Fiume, Barberi, Vern, & Baino, 2018; Havaldar, Pilli, & Putti, 2014; S. Mohamed & Shamaz, 2015). The results infer that the composite had excellent stress shielding reduction. Therefore, the implant had better life due to its good mechanical property compared to the human femur bone values.

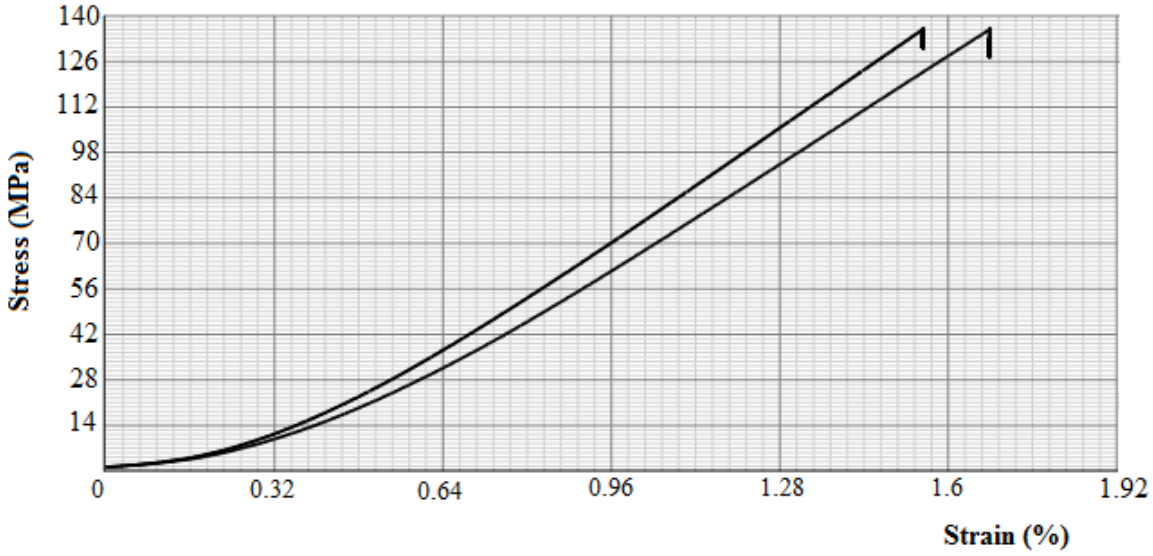

Figure 4.15: Compression test stress-strain curves

Table 4.21: Compressive strength comparison

Materials	Compressive strength (MPa)
Human cortical bone	100-230
3D printed CF/PA12 hip implant	135.8

4.11 Fatigue Results

The fatigue test results under different loading conditions for the 3D printed hip implant is presented in Table 4.22. The tests were done at 50%, 60%, 70%, and 80% UTS conditions which are within the range of the recommended loadings between 300 and 3,000 N in the ISO 7206-4 (2010) (*ASTM:F2996-13. Standard Practice for Finite Element Analysis (FEA) of Non-Modular Metallic Orthopaedic Hip Femoral Stems*, 2013) for a femoral stem to yield fatigue life of at least 5 million cycles. The S-N curve shown in Figure 4.16 illustrates variation of the fatigue strength (stress) with the total fatigue life cycles (N), which is known as an S-N curve. This curve shows relation between the cyclic stress amplitude and the number of cycles to failure. Results showed that 50% of the UTS loading conditions resulted in the

highest number of cycles. Increasing the load cause a decrease in the fatigue life of the specimen. This was consistent with the fatigue theory, which states that the greater the stress, the fewer cycles the material can withstand before it collapses (Afrose, Masood, Iovenitti, Nikzad, & Sbarski, 2016; Padzi, Bazin, & Muhamad, 2017). The average fatigue life results shown in Table 4.22 were in agreement with the expected level of high cycle fatigue performance which should be $\geq 10^5$ cycles for all loadings (*ASTM:F2996-13. Standard Practice for Finite Element Analysis (FEA) of Non-Modular Metallic Orthopaedic Hip Femoral Stems*, 2013). Therefore, the 3D printed hip implant had better fatigue strengths and therefore better longevity in service.

Table 4.22: Applied loads and fatigue life for CF/PA12 hip implant

Applied loads (N)	Maximum stress (MPa)	Number of cycles	Average number of cycles
1043.3	35.7	5,248,133	5,080,709
		4,913,285	
1251.9	42.9	1,062,408	1,146,842
		1,231,276	
1460.6	50	522,731	585,731.50
		648,732	
1669.2	57.2	240,764	212,237.50
		183,711	

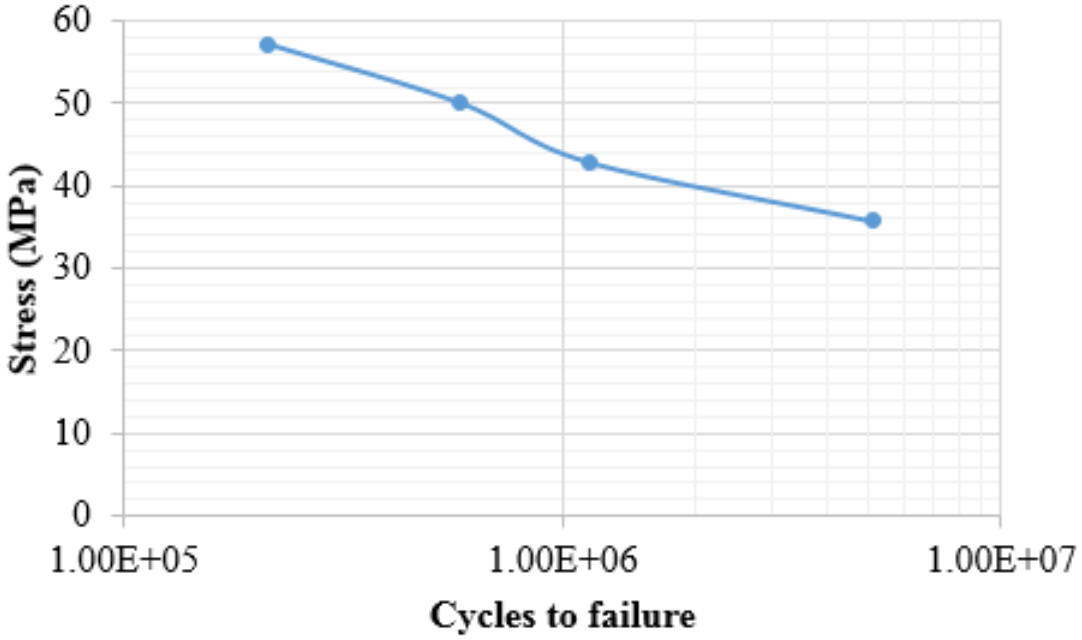

Figure 4.16: S-N Curve for 3D printed CF/PA12 hip implant

4.12 Summary

This chapter presented the results for FFF process parameters to manufacture hip joint implant using CF/PA12 filament. The optimum parameters to minimize part deflection, residual stresses and printing time were printing temperature of 255 °C, layer thickness of 0.3 mm and print speed of 50 mm/s. Experimental results were in agreement with simulated results with minimal deviation. The surface texture of the manufactured implant was rough within the acceptable range of below 2μm for hip implant. The magnitudes of the tensile, compression and fatigue properties of the 3D printed CF/PA12 composite product fell within the recommended standard for the cortical bone in the femur. Therefore, the 3D printed component is suitable candidate for further medical tests.

CHAPTER FIVE

CONCLUSIONS AND RECOMMENDATIONS

5.1 Conclusions

From this study, the following were the main conclusions:

1. The artificial prototype of hip joint implant was designed and the optimum process parameter levels determined. The results from Taguchi method with Grey relational analysis showed that a printing temperature of 255°C, a layer thickness of 0.3 mm, and a print speed of 50 mm/s simultaneously optimized deflection, residual stresses, and build time. The simulated hip joint with these settings exhibited a minimum part deflection of (3.175 ±0.266) mm, residual stress of (41.75±6.5) MPa, and build time of 28090 seconds. Printing temperature had the strongest effect on the multi-response whereas interaction between the printing temperature and the print speed, and interaction between the layer thickness and the print speed, and interaction between the printing temperature and the layer thickness did not affect the multi-response.

2. The simulation model for numerical determination of the residual stresses, part deflection and build time was developed and validated. Simulation and experimental results had acceptable agreement with error margin variation in the range of (2.51±0.04)% to (8.34±0.38)%.

3. The determined surface roughness values of (1.51±0.47) μm, (1.57±0.07)μm, and (1.61±0.07) μm for the 3D printed prototype of hip implant on the femur, femoral neck, and femoral head of the manufactured implant, respectively fell within the acceptable range of <2 μm for a better bone-to-implant contact.

The optimum process parameters yielded the desirable tensile strength of (71.48±4.80) MPa, compressive strength of 135.8 MPa, Young's Modulus of (7.54±0.22) GPa, percentage elongation of (1.86±0.54)%, and fatigue life for all investigated loadings were $\geq 10^5$ cycles .

4. The investigated mechanical integrity of the 3D printed prototype of hip implant were within the acceptable range for the cortical human bone.

5.2 Recommendations

The following are recommendations for future considerations:

1. Further study should consider wear and friction for the 3Dprinted prototype of the CF/PA12 hip implant.

2. All cyclic loadings acting on the hip implant should also be considered since hip implant will be continually loaded.

3. Other trial medical tests (in vivo and vitro) should be done to ensure the functionality the 3D printed prototype of the CF/PA12 hip implant.

4. Further research should consider thermal conductivity and diffusivity of CF/PA12 hip implant.

Publications

1. G. Nyiranzeyimana, J. M. Mutua, B. R. Mose, and T. O. Mbuya, "Optimization of process parameters in fused deposition modelling of thermoplastics:A review," Materwiss. Werksttech., vol. 52, pp.682–694, 2021. https://doi.org/10.1002/mawe.202000193

2. G. Nyiranzeyimana, J. M. Mutua, B. R. Mose, and T. O. Mbuya, "A grey-based Taguchi method to optimize fused deposition modelling process parameters for manufacture of a hip joint implant," Materwiss. Werksttech., vol. 53, issue 1, pp. 89-108, 2022. https://doi.org/10.1002/mawe.202100129.

3. Gaudence Nyiranzeyimana, James Mutuku Mutua, Thomas Ochuku Mbuya, Bruno Robert Mose, "Optimization of Fused Deposition Modelling Process Parameters and the Effect on Residual Stresses of Built Parts" Materials Today: Proceedings, vol. 62, pp.1-5, 2022. https://doi.org/10.1016/j.matpr.2022.06.557.

4. G. Nyiranzeyimana, J. M. Mutua, T. Ochuku Mbuya, B. R. Mose, and E. Bisengimana, "Fused deposition modelling (FDM) process parameter optimization to minimize residual stresses of 3 d printed carbon fiber nylon 12 hip joint implant," Materwiss. Werksttech., vol. 53, no. 10, pp. 1184–1199, 2022. https://doi.org/10.1002/mawe.202100320.

REFERENCES

Abeykoon, C., Sri-Amphorn, P., & Fernando, A. (2020). Optimization of fused deposition modeling parameters for improved PLA and ABS 3D printed structures. *International Journal of Lightweight Materials and Manufacture*, *3*(3), 284–297. Retrieved from https://doi.org/10.1016/j.ijlmm.2020.03.003 doi: 10.1016/j.ijlmm.2020.03.003

Aduba, D. C., Margaretta, E. D., Marnot, A. E., Heifferon, K. V., Surbey, W. R., Chartrain, N. A., ... Williams, C. B. (2019). Vat photopolymerization 3D printing of acid-cleavable PEG-methacrylate networks for biomaterial applications. *Materials Today*, *19*(‘1), 204–211. doi: 10.1016/j.mtcomm.2019.01.003

Afrose, M. F., Masood, S. H., Iovenitti, P., Nikzad, M., & Sbarski, I. (2016). Effects of part build orientations on fatigue behaviour of FDM-processed PLA material. *Progress in Additive Manufacturing*, *1*(1-2), 21–28. doi: 10.1007/s40964-015-0002-3

Aherwar, A., K Singh, A., & Patnaik, A. (2015). Current and future biocompatibility aspects of biomaterials for hip prosthesis. *AIMS Bioengineering*, *3*(1), 23–43. doi: 10.3934/bioeng.2016.1.23

Aimar, A., Palermo, A., & Innocenti, B. (2019). The Role of 3D Printing in Medical Applications: A State of the Art. *Journal of Healthcare Engineering*, *2019*, 1–10. doi: 10.1155/2019/5340616

Alafaghani, A., & Qattawi, A. (2018). Investigating the e ff ect of fused deposition modeling processing parameters using Taguchi design of experiment method. *Journal of Manufacturing Processes*, *36*, 164–174. Retrieved from https://doi.org/10.1016/j.jmapro.2018.09.025 doi: 10.1016/j.jmapro.2018.09.025

Albrektsson, T., & Wennerberg, A. (2004). Oral Implant Surfaces : Part 1 — Review Focusing on Topographic and Chemical Properties of Different Surfaces and In Vivo Responses to them. *International Journal of prosthodontics*, *17*, 536–543.

Al-Maharma, A. Y., Patil, S. P., & Markert, B. (2020). Effects of porosity on the mechanical properties of additively manufactured components: a critical review. *Materials Research Express*, *7*(12). doi: 10.1088/2053-1591/abcc5d

Alvarez C., K. L., Lagos C., R. F., & Aizpun, M. (2016). Investigating the influence of infill percentage on the mechanical properties of fused deposition modelled ABS parts. *Ingenieria e Investigacion*, *36*(3), 110–116. doi: 10.15446/ing .investig.v36n3.56610

Ansari, S. M. U., Ali, M. N., & Rana, N. F. (2015). Original Research Article A Study of Determination of Exhaled Carbon Monoxide and Carboxyhemoglobin in School Children. *International Journal of Biomedical And Advance Research*, *6*(11), 758–760. doi: 10.7439/ijbar

Apostu, D., Lucaciu, O., Berce, C., Lucaciu, D., & Cosma, D. (2018). Current methods of preventing aseptic loosening and improving osseointegration of titanium implants in cementless total hip arthroplasty: a review. *Journal of International Medical Research*, *46*(6), 2104–2119. doi: 10.1177/ 0300060517732697

Arabnejad, S., Johnston, B., Tanzer, M., & Pasini, D. (2017). Fully porous 3D printed titanium femoral stem to reduce stress-shielding following total hip arthroplasty. *Journal of Orthopaedic Research*, *35*(8), 1774–1783. doi: 10 .1002/jor.23445

Aslani, K. E., Chaidas, D., Kechagias, J., Kyratsis, P., & Salonitis, K. (2020). Quality performance evaluation of thinwalled PLA 3D printed parts using the taguchi method and grey relational analysis. *Journal of Manufacturing and Materials Processing*, *4*(2), 1–17. doi: 10.3390/jmmp4020047

ASTM D638-14: Standard Test Method for Tensile Properties of Plastics. (2014). doi: 10.1520/D0638-14.1

ASTM D695-15: Standard Test Method for Compressive Properties of Rigid Plastics. (2015). doi: 10.1520/D0695-15

ASTM E 837-13a: Standard Test Method for Determining Residual Stresses by the Hole-Drilling Strain-Gage Method (Tech. Rep.). (2013). doi: 10.1520/E0837-13A.2

ASTM F2792-12a "Standard Terminology for Additive Manufacturing Technologies". (2012). doi: 10.1520/F2792-12A.2

ASTM:F2996-13. Standard Practice for Finite Element Analysis (FEA) of Non-Modular Metallic Orthopaedic Hip Femoral Stems. (2013). doi: 10.1520/F2996-13.Copyright

Attaran, M. (2017). The rise of 3-D printing: The advantages of additive manufacturing over traditional manufacturing. *Business Horizons*, *60*(5), 677–688. doi: 10.1016/j.bushor.2017.05.011

Attoye, S., Malekipour, E., & El-Mounayri, H. (2019). Correlation between process parameters and mechanical properties in parts printed by the fused deposition modeling process. *Conference Proceedings of the Society for Experimental Mechanics Series*, *8*(1), 35–41. doi: 10.1007/978-3-319-95083-9_8

Bähr, F., & Westkämper, E. (2018). Correlations between Influencing Parameters and Quality Properties of Components Produced by Fused Deposition Modeling. *Procedia CIRP*, *72*(1), 1214–1219. Retrieved from `https://doi.org/10.1016/j.procir.2018.03.048` doi: 10.1016/j.procir.2018.03.048

Bakhtiari, H., Aamir, M., & Tolouei-Rad, M. (2023). Effect of 3D Printing Parameters on the Fatigue Properties of Parts Manufactured by Fused Filament Fabrication: A Review. *Applied Sciences*, *13*(2). doi: 10.3390/app13020904

Bakir, A., Atik, R., & Özerinç, S. (2020). Effect of fused deposition modeling process parameters on the mechanical properties of recycled polyethylene terephthalate parts. *Journal of Applied Polymer Science*, *138*(3), 1–12. doi: 10.1002/app.49709

Banjanin, B., Vladić, G., Pál, M., Baloš, S., Dramićanin, M., Rackov, M., &

Kneţević, I. (2018). Consistency analysis of mechanical properties of elements produced by FDM additive manufacturing technology. *Revista Materia*, *23*(4), 1–15. doi: 10.1590/s1517-707620180004.0584

Barclift;, M. W., & Williams, C. B. (2019). Examining Variability in the Mechanical Properties of Parts Mamufactured via Poljet Direct 3D Printing. *Journal of Chemical Information and Modeling*, *53*(9), 1689–1699. doi: 10.1017/CBO9781107415324.004

Bhavar, V., Kattire, P., Patil, V., Khot, S., Gujar, K., & Singh, R. (2017). A review on powder bed fusion technology of metal additive manufacturing. *Additive Manufacturing Handbook: Product Development for the Defense Industry*, 251–261. doi: 10.1201/9781315119106

Bougherara, H., & Bureau, M. (2008). Biomimetic Composite-Metal Hip Resurfacing Implant. *Research Letters in Materials Science*, *2008*, 1–6. doi: 10.1155/2008/368985

Bougherara, H., Bureau, M., Campbell, M., Vadean, A., & Yahia, L. (2007). Design of a biomimetic polymer-composite hip prosthesis. *Journal of Biomedical Materials Research - Part A*, *82*(1), 27–40. doi: 10.1002/jbm.a.31146

Bougherara, H., Bureau, M. N., & Yahia, L. (2010). Bone remodeling in a new biomimetic polymer-composite hip stem. *Journal of Biomedical Materials Research - Part A*, *92*(1), 164–174. doi: 10.1002/jbm.a.32346

Brockett, C. L., Carbone, S., Fisher, J., & Jennings, L. M. (2017). PEEK and CFR-PEEK as alternative bearing materials to UHMWPE in a fixed bearing total knee replacement: An experimental wear study. *Wear*, *374-375*, 86–91. Retrieved from `http://dx.doi.org/10.1016/j.wear.2016.12.010` doi: 10.1016/j.wear.2016.12.010

Buj-Corral, I., Domínguez-Fernández, A., & Durán-Llucià, R. (2019). Influence of print orientation on surface roughness in fused deposition modeling (FDM) processes. *Materials*, *12*(23). doi: 10.3390/ma122333834

Caminero, M. Á., Chacón, J. M., García-Plaza, E., Núñez, P. J., Reverte, J. M., &

Becar, J. P. (2019). Additive manufacturing of PLA-based composites using fused filament fabrication: Effect of graphene nanoplatelet reinforcement on mechanical properties, dimensional accuracy and texture. *Polymers*, *11*(5). doi: 10.3390/polym11050799

Campbell, M., Bureau, M. N., & Yahia, L. (2008). Performance of CF/PA12 composite femoral stems. *Journal of Materials Science: Materials in Medicine*, *19*(2), 683–693. doi: 10.1007/s10856-007-3073-y

Casavola, C., Cazzato, A., Moramarco, V., & Pappalettera, G. (2017a). Preliminary study on residual stress in FDM parts. *Conference Proceedings of the Society for Experimental Mechanics Series*, *9*(12), 91–96. doi: 10.1007/978-3-319-42255-8_12

Casavola, C., Cazzato, A., Moramarco, V., & Pappalettera, G. (2017b). Residual stress measurement in Fused Deposition Modelling parts. *Polymer Testing*, *58*(1), 249–255. Retrieved from `http://dx.doi.org/10.1016/j.polymertesting.2017.01.003` doi: 10.1016/j.polymertesting.2017.01.003

Chavan, S. A., Anwar, P. M. A., & R, P. S. B. (2017). Review of Effect of Process Parameters on Mechanical Properties of 3D Printed Components. *Internation Journal of Advance Research in Science and Engineerng*, *6*(5), 461–467.

Chergui, K., Ameddah, H., & Mazouz, H. (2018). Biomechanical analysis of fatigue behavior of a fully composite-based designed hip resurfacing prosthesis. *Journal of the Serbian Society for Computational Mechanics*, *12*(2), 80–94. doi: 10.24874/jsscm.2018.12.02.06

Chethan, K. N., Shyamasunder Bhat, N., Zuber, M., & Satish Shenoy, B. (2019). Finite element analysis of different hip implant designs along with femur under static loading conditions. *Journal of Biomedical Physics and Engineering*, *9*(5), 507–516. doi: 10.31661/jbpe.v0i0.1210

Christiyan, K. G., Chandrasekhar, U., & Venkateswarlu, K. (2016). A study on the influence of process parameters on the Mechanical Properties of 3D printed ABS composite. *IOP Conference Series: Materials Science and Engineering*,

114(1), 1–9. doi: 10.1088/1757-899X/114/1/012109

Corapi, D., Morettini, G., Pascoletti, G., & Zitelli, C. (2019). Characterization of a polylactic acid (PLA) produced by Fused Deposition Modeling (FDM) technology. *Procedia Structural Integrity*, *24*(2019), 289–295. doi: 10.1016/j.prostr.2020.02.026

Cordova, L. A., Stresing, V., Gobin, B., Rosset, P., Passuti, N., Gouin, F., ... Heymann, D. (2014). Orthopaedic implant failure: Aseptic implant loosening - the contribution and future challenges of mouse models in translational research. *Clinical Science*, *127*(5), 277–293. doi: 10.1042/CS20130338

Costa, S. F., Duarte, F. M., & Covas, J. A. (2014). Thermal conditions affecting heat transfer in FDM / FFE : a contribution towards the numerical modelling of the process. *Virtual and Physical Prototyping*, *9*, 1–12.

Da Silva, L. L., Ribeiro, V. S., Scaldaferri, D. H., Rabello, E. G., Campos, W. R., & Mansur, T. R. (2016). Development and test of an equipment to measure residual strain inside pipes using the hole-drilling method. *Latin American Journal of Solids and Structures*, *13*(13), 2439–2450. doi: 10.1590/1679-78253126

Dancel, R. (2019). Case Study Paper on Additive Manufacturing (3D Printing Technology). *Philosophy of Technology*. doi: 10.13140/RG.2.2.32535.21924

Dass, A., & Moridi, A. (2019). State of the Art in Directed Energy Deposition: From Additive Manufacturing to Materials Design. *Coatings*, *9*(7), 418. doi: 10.3390/coatings9070418

Datir, S. P., & Wynn-jones, C. H. (2005). Staged bilateral total hip arthroplasty using rough and smooth surface femoral stems with similar design. *Acta Orthopaedica*, *76*(6), 809–814. doi: 10.1080/17453670510045417

Deng, X., Zeng, Z., Peng, B., Yan, S., & Ke, W. (2018). Mechanical Properties Optimization of Poly-Ether-Ether-Ketone via Fused. *Materials*, *11*, 216. doi: 10.3390/ma11020216

Díez-Pascual, A. M. (2019). Synthesis and applications of biopolymer

composites. *International Journal of Molecular Sciences*, *20*(9). doi: 10.3390/ijms20092321

Dimitrievska, S., Whitfield, J., Hacking, S. A., & Bureau, M. N. (2009). Novel carbon fiber composite for hip replacement with improved in vitro and in vivo osseointegration. *Journal of Biomedical Materials Research - Part A*, *91*(1), 37–51. doi: 10.1002/jbm.a.32175

Dong, G., Wijaya, G., Tang, Y., & Zhao, Y. F. (2018). Optimizing process parameters of fused deposition modeling by Taguchi method for the fabrication of lattice structures. *Additive Manufacturing*, *19*, 62–72. Retrieved from http://dx.doi.org/10.1016/j.addma.2017.11.004 doi: 10.1016/j.addma.2017.11.004

Dong, H., Liu, H., Zhou, N., Li, Q., Yang, G., & Chen, L. (2020). Surface Modified Techniques and Emerging Functional Coating of Dental Implants. *Coatings*, *10*, 1–25.

du Plessis, A. (2019). Effects of process parameters on porosity in laser powder bed fusion revealed by X-ray tomography. *Additive Manufacturing*, *30*(July), 100871. Retrieved from https://doi.org/10.1016/j.addma.2019.100871 doi: 10.1016/j.addma.2019.100871

Dutta, B., & Sam Froes, F. H. (2015). The additive manufacturing (AM) of titanium alloys. *Titanium Powder Metallurgy: Science, Technology and Applications*, *1019*, 447–468. doi: 10.1016/B978-0-12-800054-0.00024-1

Elkaseer, A., Chen, K. J., Janhsen, J. C., Refle, O., Hagenmeyer, V., & Scholz, S. G. (2022). Material jetting for advanced applications: A state-of-the-art review, gaps and future directions. *Additive Manufacturing*, *60*(PA), 103270. Retrieved from https://doi.org/10.1016/j.addma.2022.103270 doi: 10.1016/j.addma.2022.103270

E-Xstream. (2019). *Digimat 2020 AM User ' s Manual* (Vol. 2886) (No. 408).

Ezoji, M., Razavi-nouri, M., & Rezadoust, A. M. (2016). Effect of Raster Angle on the Mechanical Properties of PLA 3D Printed Articles. *12th International*

Seminar on Polymer Science and Technology.

Fadhil Alani, T., Basil Ali, H., Fadhil Abbas, T., & Mohammad Othman, F. (2018). Influence of Layer Thickness on Impact Property of 3D-Printed PLA. *International Research Journal of Engineering and Technology*, *5*(2), 1–4.

Ferreira, R. T. L., & Quelho de Macedo, R. (2017). Residual thermal stress in fused deposition modelling. *24th ABCM International Congress of Mechanical Engineering December 3-8, 2017, Curitiba, PR, Brazil*, 1–7. doi: 10.26678/abcm.cobem2017.cob17-0124

Fiberlogy. (2021). *Technical Data Sheet.* Retrieved 2021-05-11, from `https://fiberlogy.com/en/fiberlogy-filaments/pa12cf{\_}en/`

Fiume, E., Barberi, J., Vern, E., & Baino, F. (2018). Bioactive Glasses : From Parent 45S5 Composition to Scaffold-Assisted Tissue-Healing Therapies. *Journal of Functional Biomaterials*, *9*(24), 1–33. doi: 10.3390/jfb9010024

Fountas, N. A., & Vaxevanidis, N. M. (2021). Optimization of fused deposition modeling process using a virus-evolutionary genetic algorithm. *Computers in Industry*, *125*, 1–11. doi: 10.1016/j.compind.2020.103371

Frunzaverde, D., Cojocaru, V., Ciubotariu, C. R., Miclosina, C. O., Ardeljan, D. D., Ignat, E. F., & Marginean, G. (2022). The Influence of the Printing Temperature and the Filament Color on the Dimensional Accuracy, Tensile Strength, and Friction Performance of FFF-Printed PLA Specimens. *Polymers*, *14*(10). doi: 10.3390/polym14101978

Garcia-Gonzalez, D., Jayamohan, J., Sotiropoulos, S. N., Yoon, S. H., Cook, J., Siviour, C. R., ... Jérusalem, A. (2017). On the mechanical behaviour of PEEK and HA cranial implants under impact loading. *Journal of the Mechanical Behavior of Biomedical Materials*, *69*(January), 342–354. doi: 10.1016/j.jmbbm.2017.01.012

Gebrehiwot, S. Z., Espinosa Leal, L., Eickhoff, J. N., & Rechenberg, L. (2021). The influence of stiffener geometry on flexural properties of 3D printed polylactic acid (PLA) beams. *Progress in Additive Manufacturing*, *6*(1), 71–81. Retrieved

from https://doi.org/10.1007/s40964-020-00146-2 doi: 10.1007/s40964-020-00146-2

Geng, P., Zhao, J., Wu, W., Ye, W., Wang, Y., Wang, S., & Zhang, S. (2019). Effects of extrusion speed and printing speed on the 3D printing stability of extruded PEEK filament E ff ects of extrusion speed and printing speed on the 3D printing stability of extruded PEEK filament. *Journal of Manufacturing Processes*, *37*(December 2018), 266–273. doi: 10.1016/j.jmapro.2018.11.023

Ghalme, S. G., Mankar, A., & Bhalerao, Y. (2016). Biomaterials in Hip Joint Replacement. *International Journal of Materials Science and Engineering*, *4*(2), 113–125. doi: 10.17706/ijmse.2016.4.2.113-125

Haleem, A., & Javaid, M. (2019). Polyether ether ketone (PEEK) and its 3D printed implants applications in medical field: An overview. *Clinical Epidemiology and Global Health*(3), 1–7. doi: 10.1016/j.cegh.2019.01.003

Han, X., Yang, D., Yang, C., Spintzyk, S., Scheideler, L., Li, P., ... Rupp, F. (2019). Carbon Fiber Reinforced PEEK Composites Based on 3D-Printing Technology for Orthopedic and Dental Applications. *Journal of Clinical Medicine*, *8*(2), 240. doi: 10.3390/jcm8020240

Hanon, M. M., Zsidai, L., & Ma, Q. (2021). Accuracy investigation of 3D printed PLA with various process parameters and different colors. *Materials Today: Proceedings*, *4*, 1–9. Retrieved from https://doi.org/10.1016/j.matpr.2020.12.1246 doi: 10.1016/j.matpr.2020.12.1246

Havaldar, R., Pilli, S. C., & Putti, B. B. (2014). Insights into the effects of tensile and compressive loadings on human femur bone. *Advanced Biomedical Research*, *3*, 1–6. doi: 10.4103/2277-9175.129375

Hegab, H. A. (2016). Design for additive manufacturing of composite materials and potential alloys: A review. *Manufacturing Review*, *3*(11), 1–17. doi: 10.1051/mfreview/2016010

Higuchi, Y., Seki, T., Takegami, Y., Komatsu, D., & Morita, D. (2018). Orthopaedics & Traumatology : Surgery & Research Same survival but higher

rate of osteolysis for metal-on-metal Ultamet versus ceramic-on-ceramic in patients undergoing primary total hip arthroplasty after 8 years of follow-up. *Orthopaedics & Traumatology: Surgery & Research*, *104*(8), 1155–1161. Retrieved from https://doi.org/10.1016/j.otsr.2018.08.005 doi: 10.1016/j.otsr.2018.08.005

Hsueh, M.-h., Lai, C.-j., Wang, S.-h., Zeng, Y.-s., Hsieh, C.-h., & Pan, C.-y. (2021). Effect of Printing Parameters on the Thermal and Mechanical Properties of 3D-Printed PLA and PETG , Using Fused. *Polymers*, *13*, 1–11.

Ibrahim, M. Z., Sarhan, A. A., Yusuf, F., & Hamdi, M. (2017). Biomedical materials and techniques to improve the tribological, mechanical and biomedical properties of orthopedic implants – A review article. *Journal of Alloys and Compounds*, *714*, 636–667. doi: 10.1016/j.jallcom.2017.04.231

ISO 7206-2, Implants for Surgery (Tech. Rep.). (2011).

Jansson, A., & Pejryd, L. (2015). Characterisation of carbon fibre-reinforced polyamide manufactured by selective laser sintering. *Additive Manufacturing*, *30*, 7–13. Retrieved from http://dx.doi.org/10.1016/j.addma.2015.12.003 doi: 10.1016/j.addma.2015.12.003

Jatti, V. S., Jatti, S. V., & Patel, A. P. (2019). A study on effect of fused deposition modeling process parameters on mechanical properties. *International Journal of Scientific and Technology Research*, *8*(11), 689–693.

Jia, H., Sun, H., Wang, H., Wu, Y., & Wang, H. (2021). Scanning strategy in selective laser melting (SLM): a review. *International Journal of Advanced Manufacturing Technology*, *113*(9-10), 2413–2435. doi: 10.1007/s00170-021-06810-3

Kamachi Mudali, U., Sridhar, T. M., & Baldev, R. A. (2003). Corrosion of bio implants. *Proceedings in Engineering Sciences*, *28*(3-4), 601–637. doi: 10.1007/BF02706450

Kantaros, A., & Karalekas, D. (2013). Fiber Bragg grating based investigation of residual strains in ABS parts fabricated by fused deposition modeling process.

Materials and Design, *50*(1), 44–50. Retrieved from http://dx.doi.org/10.1016/j.matdes.2013.02.067 doi: 10.1016/j.matdes.2013.02.067

Kapadia, D. (2018). *Characterising and Quantifying Volumetric Edge-Wear in Ceramic-On-Ceramic Hip Arthroplasty Devices* (PhD Thesis). Huddersfield.

Kasim, M. S., Harun, N. H., Hafiz, M. S. A., Mohamed, S. B., & Mohamad, W. N. F. W. (2019). Multi-response optimization of process parameter in fused deposition modelling by response surface methodology. *International Journal of Recent Technology and Engineering*, *8*(3), 327–338. doi: 10.35940/ijrte.C4152.098319

Kasperovich, G., Haubrich, J., Gussone, J., & Requena, G. (2016). Correlation between porosity and processing parameters in TiAl6V4 produced by selective laser melting. *Materials and Design*, *105*, 160–170. Retrieved from http://dx.doi.org/10.1016/j.matdes.2016.05.070 doi: 10.1016/j.matdes.2016.05.070

Katschnig, M., & Holzer, C. (2018). Cranial polyetheretherketone implants by extrusion–based additive manufacturing: state of the art and prospects. *Material Science & Engineering International Journal*, *2*(3), 66–68. doi: 10.15406/mseij.2018.02.00036

Khmyrov, R. S., Kotoban, D., & Gusarov, A. V. (2016). Distortions and residual stresses at layer- by-layer additive manufacturing by fusion. *Journal of Manufacturing Science and Engineering*, *139*. doi: 10.1115/1.4034714

Kosaraju, S., Anne, V. G., & Popuri, B. B. (2013). Finite element simulation of cutting forces in turning Ti6AI4V using deform 3D. *ASME International Mechanical Engineering Congress and Exposition, Proceedings (IMECE)*, *2 A*, 1–7. doi: 10.1115/IMECE2013-62868

Kovan, V., Tezel, T., Camurlu, H., & Topal, E. (2018). Effect of processing parameters on mechanical properties of 3D printed PLA/Carbon fibre composites. *Materials Science Forum*, *919*(4), 230–235. doi: 10.4028/www.scientific.net/MSF.919.230

Krajangsawasdi, N., Blok, L. G., Hamerton, I., & Longana, M. L. (2021). Fused Deposition Modelling of Fibre Reinforced Polymer Composites : A Parametric Review. *Journal of Composites Science*, *5*(29), 1–38.

Kumar, P., Ahuja, I. S., & Singh, R. (2016). Effect of process parameters on surface roughness of hybrid investment casting. *Progress in Additive Manufacturing*, *1*(1), 45–53. doi: 10.1007/s40964-016-0004-9

Kumar, S., Kannan, V., & Sankaranarayanan, G. (2014). Parameter Optimization of ABS-M30i Parts Produced by Fused Deposition Modeling for Minimum Surface Roughness. *International Journal of Current Engineering and Technology*(3), 93–97.

Kumbhar, N. N., & Mulay, A. V. (2018). Post Processing Methods used to Improve Surface Finish of Products which are Manufactured by Additive Manufacturing Technologies: A Review. *Journal of The Institution of Engineers (India): Series C*, *99*(4), 481–487. doi: 10.1007/s40032-016-0340-z

Kuo, Y., Yang, T., & Huang, G. W. (2008). The use of a grey-based Taguchi method for optimizing multi-response simulation problems. *Computers and Industrial Engineering*, *55*(1), 80–93. doi: 10.1016/j.cie.2007.12.002

Le, L., Rabsatt, M. A., Eisazadeh, H., & Torabizadeh, M. (2022). Reducing print time while minimizing loss in mechanical properties in consumer FDM parts. *International Journal of Lightweight Materials and Manufacture*, *5*(2), 197–212. Retrieved from `https://doi.org/10.1016/j.ijlmm.2022.01.003` doi: 10.1016/j.ijlmm.2022.01.003

Lecis, N., Beltrami, R., & Mariani, M. (2021). Binder jetting 3D printing of 316 stainless steel: Influence of process parameters on microstructural and mechanical properties. *Metallurgia Italiana*, *113*(2), 31–41.

Liao, C., & Li, Y. (2020). Polyetheretherketone and Its Composites for Bone. *Polymers*, *12*(2858), 1–48.

Liao, G., Li, Z., Cheng, Y., Xu, D., Zhu, D., Jiang, S., ... Zhu, Y. (2017). Properties of oriented carbon fiber/polyamide 12 composite parts fabricated

by fused deposition modelling. *Materials & Design*, *139*, 1–49. Retrieved from http://dx.doi.org/10.1016/j.matdes.2017.11.027 doi: 10.1016/j.matdes.2017.11.027

Lim, J. S., Oh, W. J., Lee, C. M., & Kim, D. H. (2021). Selection of effective manufacturing conditions for directed energy deposition process using machine learning methods. *Scientific Reports*, *11*(1), 1–13. Retrieved from https://doi.org/10.1038/s41598-021-03622-z doi: 10.1038/s41598-021-03622-z

Limmahakhun, S. (2017). *Development of Functionally Graded Materials for Innovation in Bone-Replacement Applications* (Unpublished doctoral dissertation). Queensland University of Technology, Australia.

Liu, Y., Bai, W., Cheng, X., Tian, J., Wei, D., Sun, Y., & Di, P. (2020). Effects of printing layer thickness on mechanical properties of 3D-printed custom trays. *Journal of Prosthetic Dentistry*, *123*(1), 1–7. Retrieved from https://doi.org/10.1016/j.prosdent.2020.08.025 doi: 10.1016/j.prosdent.2020.08.025

Madireddy, G., Li, C., Liu, J., & Sealy, M. P. (2019). Modeling thermal and mechanical cancellation of residual stress from hybrid additive manufacturing by laser peening. *Nanotechnology and Precision Engineering*, *2*(2), 49–60. doi: 10.1016/j.npe.2019.07.001

Manivasagam, G., Dhinasekaran, D., & Rajamanickam, A. (2010). Biomedical Implants: Corrosion and its Prevention - A Review. *Recent Patents on Corrosion Science*, *2*(1), 40–54. doi: 10.2174/1877610801002010040

Mansour, S., & Hague, R. (2003). Impact of rapid manufacturing on design for manufacture for injection moulding. *Proceedings of the Institution of Mechanical Engineers, Part B: Journal of Engineering Manufacture*, *217*(4), 453–461. doi: 10.1243/095440503321628134

Mathew, E., Domínguez-Robles, J., Larrañeta, E., & Lamprou, D. A. (2019). Fused deposition modelling as a potential tool for antimicrobial dialysis catheters manufacturing: New trends vs. conventional approaches. *Coatings*, *9*(8), 1–15.

doi: 10.3390/coatings9080515

Maxwell, A. S., & Turnbull, A. (2003). Measurement of residual stress in engineering plastics using the hole-drilling technique. *Polymer Testing*, *22*, 231–233.

Megahed, M., Mindt, H. W., N'Dri, N., Duan, H., & Desmaison, O. (2016). *Metal additive-manufacturing process and residual stress modeling* (Vol. 5) (No. 1). Integrating Materials and Manufacturing Innovation. Retrieved from `http://dx.doi.org/10.1186/s40192-016-0047-2` doi: 10.1186/s40192-016-0047-2

Mercelis, P., & Kruth, J. P. (2006). Residual stresses in selective laser sintering and selective laser melting. *Rapid Prototyping Journal*, *12*(5), 254–265. doi: 10.1108/13552540610707013

Miazio, Ł. (2019). Impact of Print Speed on Strength of Samples Printed in FDM Technology. *Agricultural Engineering*, *23*(2), 33–38. doi: 10.1515/agriceng-2019-0014

Mirzababaei, S., & Pasebani, S. (2019). A Review on Binder Jet Additive Manufacturing of 316L Stainless Steel. *Journal of Manufacturing and Materials Processing*, *3*(3), 82. doi: 10.3390/jmmp3030082

Mohamed, O. A., Masood, S. H., & Bhowmik, J. L. (2016a). Analytical modelling and optimization of the temperature-dependent dynamic mechanical properties of fused deposition fabricated parts made of PC-ABS. *Materials*, *9*(11), 895. doi: 10.3390/ma9110895

Mohamed, O. A., Masood, S. H., & Bhowmik, J. L. (2016b). Investigation of dynamic elastic deformation of parts processed by fused deposition modeling additive manufacturing. *Advances in Production Engineering And Management*, *11*(3), 227–238. doi: 10.14743/apem2016.3.223

Mohamed, O. A., Masood, S. H., & Bhowmik, J. L. (2016c). Optimization of fused deposition modeling process parameters for dimensional accuracy using I-optimality criterion. *Measurement*, *81*(4), 174–196. doi: 10.1016/j.measurement.2015.12.011

Mohamed, O. A., Masood, S. H., Bhowmik, J. L., Nikzad, M., & Azadmanjiri, J.

(2016). Effect of Process Parameters on Dynamic Mechanical Performance of FDM PC/ABS Printed Parts Through Design of Experiment. *Journal of Materials Engineering and Performance*, *25*(7), 2922–2935. doi: 10.1007/s11665-016-2157-6

Mohamed, S., & Shamaz, B. H. (2015). Bone Tissue Engineering and Bony Scaffolds. *International Journal of Dentistry and Oral Health*, *1*(1), 15–20. doi: 10.25141/2471-657X-2015-1.0001

Mohan, N., Senthil, P., Vinodh, S., & Jayanth, N. (2017). A review on composite materials and process parameters optimisation for the fused deposition modelling process. *Virtual and Physical Prototyping*, *12*(1), 47–59. doi: 10.1080/17452759.2016.1274490

Monzón, M., Ortega, Z., Hernández, A., Paz, R., & Ortega, F. (2017). Anisotropy of photopolymer parts made by digital light processing. *Materials*, *10*(1), 1–15. doi: 10.3390/ma10010064

Morales, N. G., Fleck, T. J., & Rhoads, J. F. (2018). The effect of interlayer cooling on the mechanical properties of components printed via fused deposition. *Additive Manufacturing*, *24*, 243–248. Retrieved from `https://doi.org/10.1016/j.addma.2018.09.001` doi: 10.1016/j.addma.2018.09.001

Mostafa, K. G., Montemagno, C., & Qureshi, A. J. (2018). Strength to cost ratio analysis of FDM Nylon 12 3D Printed Parts. *Procedia Manufacturing*, *26*, 753–762. doi: 10.1016/j.promfg.2018.07.086

Mostafaei, A., Elliott, A. M., Barnes, J. E., Li, F., Tan, W., Cramer, C. L., ... Chmielus, M. (2021). Binder jet 3D printing—Process parameters, materials, properties, modeling, and challenges. *Progress in Materials Science*, *119*(June 2020), 100707. Retrieved from `https://doi.org/10.1016/j.pmatsci.2020.100707` doi: 10.1016/j.pmatsci.2020.100707

Mugwagwa, L., Yadroitsev, I., & Matope, S. (2019). Effect of process parameters on residual stresses, distortions, and porosity in selective laser melting of maraging steel 300. *Metals*, *9*(10). doi: 10.3390/met9101042

Mukherjee, T., Zhang, W., & DebRoy, T. (2017a). An improved prediction of residual stresses and distortion in additive manufacturing. *Computational Materials Science*, *126*, 360–372. Retrieved from http://dx.doi.org/10.1016/j.commatsci.2016.10.003 doi: 10.1016/j.commatsci.2016.10.003

Mukherjee, T., Zhang, W., & DebRoy, T. (2017b). An improved prediction of residual stresses and distortion in additive manufacturing. *Computational Materials Science*, *126*, 360–372. Retrieved from http://dx.doi.org/10.1016/j.commatsci.2016.10.003 doi: 10.1016/j.commatsci.2016.10.003

Mutua, J. M. (2018). *3D Additive Manufacturing, Microstructure, and Mechanical Properties of High Performance Materials* (Unpublished doctoral dissertation). Tottori.

Nag, S., & Banerjee, R. (2012). Fundamentals of Medical Implant Materials. *ASM Handbook*, *23*, 1–12. doi: 10.1111/j.1755-6724.1935.mp14001006.x

Nancharaiah, T. (2011). Optimization of Process Parameters in FDM Process Using Design of Experiments. *International Journal on Emerging Technologies*, *2*(1), 100–102. doi: 10.1109/15.990730

Nickel, A. H., Barnett, D. M., & Prinz, F. B. (2001). Thermal stresses and deposition patterns in layered manufacturing. *Materials Science and Engineering*, *A317*, 59–64.

Ning, F., Cong, W., Hu, Y., & Wang, H. (2017). Additive manufacturing of carbon fiber-reinforced plastic composites using fused deposition modeling : Effects of process parameters on tensile properties. *Journal of Composite Materials*, *5*(4), 452–462. doi: 10.1177/0021998316646169

Nyiranzeyimana, G., Mutua, J., Mose, B., & Mbuya, T. (2021). Optimization of process parameters in fused deposition modelling of thermoplastics : A review. *Materialwissenschaft und Werkstofftechnik*, *52*, 682–694. doi: 10.1002/mawe.202000193

Nyiranzeyimana, G., Mutua, J. M., Mose, B. R., & Mbuya, T. O. (2022). A grey-based Taguchi method to optimize fused deposition modelling process

parameters for manufacture of a hip joint implant. *Materialwissenschaft und Werkstofftechnik*, *53*(1), 89–108. doi: 10.1002/mawe.202100129

Obiko, J. O., Mwema, F. M., & Bodunrin, M. O. (2021). Validation and optimization of cutting parameters for Ti-6Al-4V turning operation using DEFORM 3D simulations and Taguchi method. *Manufacturing Review*, *8*(5), 1–13. doi: 10.1051/mfreview/2021001

Ogawa, M., Tohma, Y., Ohgushi, H., Takakura, Y., & Tanaka, Y. (2012). Early fixation of cobalt-chromium based alloy surgical implants to bone using a tissue-engineering approach. *International Journal of Molecular Sciences*, *13*(5), 5528–5541. doi: 10.3390/ijms13055528

Oshkour, A. A., Osman, N. A., Bayat, M., Afshar, R., & Berto, F. (2014). Three-dimensional finite element analyses of functionally graded femoral prostheses with different geometrical configurations. *Materials and Design*, *56*, 998–1008. Retrieved from `http://dx.doi.org/10.1016/j.matdes.2013.12.054` doi: 10.1016/j.matdes.2013.12.054

Othman, F. M., Fadhil, T., & Hind, A. (2018). Influence of Process Parameters on Mechanical Properties and Printing Time of FDM PLA Printed Parts Using Design of Experiment. *Engineering Research and Applications*, *8*(7), 65–69. doi: 10.9790/9622-0807026569

Ouhsti, M., Haddadi, B. E., Mellal, B., & Belhouideg, S. (2018). Effect of Printing Parameters on the Mechanical Properties of Parts Fabricated with Open-Source 3D Printers in PLA by Fused Deposition Modeling. *Mechanics and Mechanical Engineering*, *22*(4), 895–907.

Ozkan, D., Gok, M. S., & Karaoglanli, A. C. (2020). Carbon Fiber Reinforced Polymer (CFRP) Composite Materials, Their Characteristic Properties, Industrial Application Areas and Their Machinability. *Advanced Structured Materials*, *124*(May), 235–253. doi: 10.1007/978-3-030-39062-4_20

Padhi, S. K., Sahu, R. K., Mahapatra, S. S., Das, H. C., Sood, A. K., Patro, B., & Mondal, A. K. (2017). Optimization of fused deposition modeling process

parameters using a fuzzy inference system coupled with Taguchi philosophy. *Advances in Manufacturing*, *5*(3), 231–242. doi: 10.1007/s40436-017-0187-4

Padzi, M. M., Bazin, M. M., & Muhamad, W. M. (2017). Fatigue Characteristics of 3D Printed Acrylonitrile Butadiene Styrene (ABS). *IOP Conference Series: Materials Science and Engineering*, *269*(1), 1–6. doi: 10.1088/1757-899X/269/1/012060

Palaniappan, T., Ajitha, V., Dorairaju, K., Anitha, G., Gnanavel, S., & Gupta, N. (2020). Study of 3D model hip implant using ANSYS analysis. *AIP Conference Proceedings*, *2281*. doi: 10.1063/5.0026236

Panda, A. K., & Singh, R. K. (2013). Optimization of Process Parameters in the Catalytic Degradation of Polypropylene to Liquid Fuel by Taguchi Method. *International Journal of Multidisciplinary and Current*, *2*(4), 50–58. Retrieved from `www.seipub.org/acer`

Pavan Kumar, G., & Regalla, S. P. (2012). Optimization of support material and build time in fused deposition modeling (FDM). *Applied Mechanics and Materials*, *110-116*, 2245–2251. doi: 10.4028/www.scientific.net/AMM.110-116.2245

Peral, D., Vicente, J. D., Porro, J. A., & Ocaña, J. L. (2017). Uncertainty analysis for non-uniform residual stresses determined by the hole drilling strain gauge method. *Measurement*, *97*(5), 51–63. Retrieved from `http://dx.doi.org/10.1016/j.measurement.2016.11.010` doi: 10.1016/j.measurement.2016.11.010

Pervez, N., Faizan, S., Zahid, S., Muhammad, M. J., & Yingjie, C. (2018). Multi-Response Optimization of Resin Finishing by Using a Taguchi-Based Grey Relational Analysis. *materials*, *11*(426), 1–19. doi: 10.3390/ma11030426

Pietrzak, W. S. (2019). Ultra-High Molecular Weight Polyethylene for Total Hip Acetabular Liners : A Brief Review of Current Status. *Journal of Investigative Surgery*, *0*(0), 1–3. Retrieved from `https://doi.org/10.1080/08941939.2019.1624898` doi: 10.1080/08941939.2019.1624898

Pilipović, A., Šercer, M., & Raos, P. (2011). Experimental testing of quality of polymer parts produced by laminated object manufacturing - LOM. *Tehnicki Vjesnik*, *18*(2), 253–260.

Polozov, I., Sufiiarov, V., & Borisov, E. (2016). Producing hip implants of titanium alloys by additive manufacturing. *International Journal of Bioprinting*, *2*(2), 78–84. doi: 10.18063/IJB.2016.02.004

Prasad, K., Bazaka, O., Chua, M., Rochford, M., Fedrick, L., Spoor, J., ... Bazaka, K. (2017). Metallic biomaterials: Current challenges and opportunities. *Materials*, *10*(8), 1–33. doi: 10.3390/ma10080884

Qamar Tanveer, M., Mishra, G., Mishra, S., & Sharma, R. (2022). Effect of infill pattern and infill density on mechanical behaviour of FDM 3D printed Parts-a current review. *Materials Today: Proceedings*, *62*(March), 100–108. doi: 10.1016/j.matpr.2022.02.310

Qayyum, H., Hussain, G., Sulaiman, M., Hassan, M., Ali, A., Muhammad, R., ... Altaf, K. (2022). Effect of Raster Angle and Infill Pattern on the In-Plane and Edgewise Flexural Properties of Fused Filament Fabricated Acrylonitrile–Butadiene–Styrene. *Applied Sciences*, *12*(24), 1–15. doi: 10 .3390/app122412690

Rahim, T. N., Abdullah, A. M., Akil, H. M., Mohamad, D., & Rajion, Z. A. (2017). The improvement of mechanical and thermal properties of polyamide 12 3D printed parts by fused deposition modelling. *Express Polymer Letters*, *11*(12), 963–982. doi: 10.3144/expresspolymlett.2017.92

Rajpurohit, S. R., & Dave, H. K. (2018). Effect of process parameters on tensile strength of FDM printed PLA part. *Rapid Prototyping Journal*, *24*(8), 1317–1324. doi: 10.1108/RPJ-06-2017-0134

Ramya, A., & Vanapalli, S. L. (2016). 3D printing technologies in various applications. *International Journal of Mechanical Engineering and Technology*, *7*(3), 396–409.

Rarani, M., Ezati, N., Sadeghi, P., & Badrossamay, M. (2020). Optimization of FDM

process parameters for tensile properties of polylactic acid specimens using Taguchi design of experiment method. *Thermoplastic Composite Materials*, *2*(1), 1–18. doi: 10.1177/0892705720964560

Rashid, R., Masood, S., Ruan, D., Palanisamy, S., Huang, X., & Rahman Rashid, R. A. (2023). Design Optimization and Finite Element Model Validation of LPBF-Printed Lattice-Structured Beams. *Metals*, *13*(2). doi: 10.3390/met13020184

Rayegani, F., & Onwubolu, G. C. (2014). Fused deposition modelling (fdm) process parameter prediction and optimization using group method for data handling (gmdh) and differential evolution (de). *International Journal of Advanced Manufacturing Technology*, *73*(1-4), 509–519. doi: 10.1007/s00170-014-5835-2

Rebelo, R., Fernandes, M., & Fangueiro, R. (2017). Biopolymers in Medical Implants: A Brief Review. *Procedia Engineering*, *200*, 236–243. doi: 10.1016/j.proeng.2017.07.034

Ridzwan, M. I., Shuib, S., Hassan, A. Y., Shokri, A. A., & Mohammad Ibrahim, M. N. (2007). Problem of stress shielding and improvement to the hip implant designs: A review. *Journal of Medical Sciences*, *7*(3), 460–467. doi: 10.3923/jms.2007.460.467

Rodríguez-Panes, A., Claver, J., & Camacho, A. M. (2018). The influence of manufacturing parameters on the mechanical behaviour of PLA and ABS pieces manufactured by FDM: A comparative analysis. *Materials*, *11*(8), 1–21. doi: 10.3390/ma11081333

Saboori, A., Aversa, A., Marchese, G., Biamino, S., Lombardi, M., & Fino, P. (2019). Application of Directed Energy Deposition-Based Additive Manufacturing in Repair. *Applied Sciences*, *9*(16), 3316. doi: 10.3390/app9163316

Santhakumar, J., Iqbal, U. M., & M.Prakash. (2017). Investigation on the Effect of Tensile Strength on FDM Build Parts using Taguchi-Grey Relational Based Multi-Response Optimization. *International Journal of Mechanical Engineering and Technology*, *8*(12), 53–60.

Saphronov, V., Khmyrov, R. S., & Gusarov, A. V. (2015). Experimental and theoretical study of residual deformations and stresses at additive manufacturing by fusion. *Lasers in Manufacturing*, 1–5.

Satish, B., Girish, H., & Siddesh, B. (2019). Taguchi grey relational analysis for parametric optimization of severe plastic deformation process. *SN Applied Sciences*, *1*(8), 1–11. Retrieved from https://doi.org/10.1007/s42452-019-0982-6 doi: 10.1007/s42452-019-0982-6

Schajer, G. S. (2017). Measurement of Non-Uniform Residual Stresses Using the Hole- Drilling Method . Part I — Stress Calculation Procedures. *Journal of Engineering Materials and Technology*, *110*, 338–343.

Semlitsch, M. (1987). Titanium alloys for hip joint replacements. *Clinical Materials*, *2*(1), 1–13. doi: 10.1016/0267-6605(87)90015-1

Senalp, A. Z., Kayabasi, O., & Kurtaran, H. (2007). Static, dynamic and fatigue behavior of newly designed stem shapes for hip prosthesis using finite element analysis. *Materials and Design*, *28*(5), 1577–1583. doi: 10.1016/j.matdes.2006.02.015

Shahali, H., Jaggessar, A., & Yarlagadda, P. K. (2017). Recent Advances in Manufacturing and Surface Modification of Titanium Orthopaedic Applications. *Procedia Engineering*, *174*, 1067–1076. Retrieved from http://dx.doi.org/10.1016/j.proeng.2017.01.259 doi: 10.1016/j.proeng.2017.01.259

Shakeria, Z., Benfriha, K., Zirak, N., Shirinbayan, M., & Shakeri, Z. (2021). Optimization of FFF Processing Parameters to Improve Geometrical Accuracy and Mechanical Behavior of Polyamide 6 Using Grey Relational Analysis (GRA). Retrieved from https://doi.org/10.21203/rs.3.rs-1118150/v1

Sharma, K., Kumar, K., Singh, K. R., & Rawat, M. S. (2021). Optimization of FDM 3D printing process parameters using Taguchi technique. *IOP Conference Series: Materials Science and Engineering*, *1168*(1), 012022. doi: 10.1088/1757-899x/1168/1/012022

Shi, L., Northwood, D. O., & Cao, Z. (1994). The properties of a wrought biomedical cobalt-chromium alloy. *Journal of Materials Science*, *29*(5), 1233–1238. doi: 10.1007/BF00975070

Simiyu, L. W., Mutua, J. M., Muiruri, P. I., & Ikua, B. W. (2023). Optimization of polygonal cross-sectioned conformal cooling channels in injection molding. *International Journal on Interactive Design and Manufacturing*, *17*(2), 1–17. Retrieved from `https://doi.org/10.1007/s12008-023-01226-7` doi: 10 .1007/s12008-023-01226-7

Srivastava, M., & Rathee, S. (2018). Optimisation of FDM process parameters by Taguchi method for imparting customised properties to components. *Virtual and Physical Prototyping*, *13*(3), 203–210. doi: 10.1080/17452759.2018 .1440722

Sumalatha, M., Malleswara Rao, J. N., & Supraja Reddy, B. (2021). Optimization Of Process Parameters In 3d Printing-Fused Deposition Modeling Using Taguchi Method. *IOP Conference Series: Materials Science and Engineering*, *1112*(1), 14. doi: 10.1088/1757-899x/1112/1/012009

Tang, C., Liu, J., Yang, Y., Liu, Y., Jiang, S., & Hao, W. (2020). Effect of process parameters on mechanical properties of 3D printed PLA lattice structures. *Composites Part C: Open Access*, *3*(September), 100076. doi: 10.1016/j.jcomc .2020.100076

Taqriban, R. B., Ismail, R., Jamari, J., & Bayuseno, A. P. (2021). Finite element analysis of artificial hip joint implant made from stainless steel 316l. *Bali Medical Journal*, *10*(1), 448–452. doi: 10.15562/bmj.v10i1.2236

Tavakkoli Avval, P., Samiezadeh, S., Klika, V., & Bougherara, H. (2015). Investigating stress shielding spanned by biomimetic polymer-composite vs. metallic hip stem: A computational study using mechano-biochemical model. *Journal of the Mechanical Behavior of Biomedical Materials*, *41*, 56–67. doi: 10.1016/j.jmbbm.2014.09.019

Teo, A. J., Mishra, A., Park, I., Kim, Y. J., Park, W. T., & Yoon, Y. J. (2016).

Polymeric Biomaterials for Medical Implants and Devices. *ACS Biomaterials Science and Engineering*, *2*(4), 454–472. doi: 10.1021/acsbiomaterials.5b00429

Tran, N. H., Nguyen, V. N., Ngo, A. V., & Nguyen, V. C. (2017). Study on the Effect of Fused Deposition Modeling (FDM) Process Parameters on the Printed Part Quality. *Int. Journal of Engineering Research and Application*, *7*(2), 71–77. doi: 10.9790/9622-0712027177

Tyagi, S., Yadav, A., & Deshmukh, S. (2021). Review on mechanical characterization of 3D printed parts created using material jetting process. *Materials Today: Proceedings*, *51*(xxxx), 1012–1016. Retrieved from `https://doi.org/10.1016/j.matpr.2021.07.073` doi: 10.1016/j.matpr.2021.07.073

Udroiu, R. (2012). Powder Bed Additive Manufacturing Systems and its applications. *Academic Journal of Manufacturing Engineering*, *10*(O4), 122–129.

Van Noort, R. (1987). Titanium: The implant material of today. *Journal of Materials Science*, *22*(11), 3801–3811. doi: 10.1007/BF01133326

Vanaei, H. R., Raissi, K., Deligant, M., Shirinbayan, M., Fitoussi, J., Khelladi, S., & Tcharkhtchi, A. (2020). Toward the understanding of temperature effect on bonding strength, dimensions and geometry of 3D-printed parts. *Journal of Materials Science*, *55*(29), 14677–14689. doi: 10.1007/s10853-020-05057-9

Verdejo, E., Toro, D., Coello, J., Matínez, A., Técnica, E., & Ingenieros, S. D. (2019). Analysis of the influence of the variables of the Fused Deposition Modeling (FDM) process on the mechanical properties of a carbon-reinforced polyamide. *Procedia Manufacturing*, *41*(1), 731–738. Retrieved from `https://doi.org/10.1016/j.promfg.2019.09.064` doi: 10.1016/j.promfg.2019.09.064

Verma, A., Vishnoi, P., Sukhotskiy, V., & Furlani, E. P. (2018). Numerical simulation of extrusion additive manufacturing: Fused deposition modeling. *Advanced Materials*, *4*(1), 118–121.

Walczak, J., Shahgaldi, F., & Heatley, F. (1998). In vivo corrosion of 316L stainless-steel hip implants: Morphology and elemental compositions of

corrosion products. *Biomaterials*, *19*(1-3), 229–237. doi: 10.1016/S0142-9612(97)00208-1

Wang, C. C., Lin, T. W., & Hu, S. S. (2007). Optimizing the rapid prototyping process by integrating the Taguchi method with the Gray relational analysis. *Rapid Prototyping Journal*, *13*(5), 304–315. doi: 10.1108/13552540710824814

Wang, D., Dou, W., & Yang, Y. (2018). Research on selective laser melting of Ti6Al4V: Surface morphologies, optimized processing zone, and ductility improvement mechanism. *Metals*, *8*(7). doi: 10.3390/met8070471

Wang, W. L., Cheah, C. M., Fuh, J. Y., & Lu, L. (1996). Influence of process parameters on stereolithography part shrinkage. *Materials and Design*, *17*(4), 205–213. doi: 10.1016/S0261-3069(97)00008-3

Wang, Y., Xu, Z., Wu, D., & Bai, J. (2020). Current status and prospects of polymer powder 3D printing technologies. *Materials*, *13*(10). doi: 10.3390/ma13102406

Wankhede, V., Jagetiya, D., Joshi, A., & Chaudhari, R. (2020). Experimental investigation of FDM process parameters using Taguchi analysis Materials Today : Proceedings Experimental investigation of FDM process parameters using Taguchi analysis. *Materials Today: Proceedings*, *27*, 2117–2120. doi: 10.1016/j.matpr.2019.09.078

Wickramasinghe, S., Do, T., & Tran, P. (2020). FDM-Based 3D printing of polymer and associated composite: A review on mechanical properties, defects and treatments. *Polymers*, *12*(7), 1–42. doi: 10.3390/polym12071529

Wu, A. S., Brown, D. W., Kumar, M., Gallegos, G. F., & King, W. E. (2014). An Experimental Investigation into Additive Manufacturing-Induced Residual Stresses in 316L Stainless Steel. *Metallurgical and Materials Transactions A*, *45*(13), 6260–6270. doi: 10.1007/s11661-014-2549-x

Wu, W., Geng, P., Li, G., Zhao, D., Zhang, H., & Zhao, J. (2015). Influence of layer thickness and raster angle on the mechanical properties of 3D-printed PEEK and a comparative mechanical study between PEEK and ABS. *Materials*,

8(9), 5834–5846. doi: 10.3390/ma8095271

Xia, H., Lu, J., Dabiri, S., & Tryggvason, G. (2018). Fully resolved numerical simulations of fused deposition modeling. Part I: fluid flow. *Rapid Prototyping Journal*, *24*(2), 463–476. doi: 10.1108/RPJ-12-2016-0217

Xia, Z., Ricciardi, B. F., Liu, Z., Ruhland, C. V., Ward, M., Lord, A., ... Perino, G. (2017). Nano-analyses of wear particles from metal-on-metal and non-metal-on-metal dual modular neck hip arthroplasty. *Nanomedicine: Nanotechnology, Biology, and Medicine*, *13*(3), 1205–1217. Retrieved from `http://dx.doi.org/10.1016/j.nano.2016.11.003` doi: 10.1016/j.nano.2016.11.003

Xing, W., Ouyang, D., Li, N., & Liu, L. (2018). Estimation of residual stress in selective laser melting of a Zr-based amorphous alloy. *Materials*, *11*(8), 1–16. doi: 10.3390/MA11081480

Yadav, D., Chhabra, D., Kumar Garg, R., Ahlawat, A., & Phogat, A. (2020). Optimization of FDM 3D printing process parameters for multi-material using artificial neural network. *Materials Today: Proceedings*, *21*(40), 1583–1591. doi: 10.1016/j.matpr.2019.11.225

Zameer, S., & Haneef, M. (2015). Fatigue Life Estimation of Artificial Hip Joint Model Using Finite Element Method. *Materials Today: Proceedings*, *2*(4-5), 2137–2145. doi: 10.1016/j.matpr.2015.07.220

Zaroog, O. S., Yap, C., Ken, W., Noorlina, A., & Manap, A. (2014). Current and Challenge of Residual Stress Measurement Techniques. *International Journal of Science and Research (IJSR)*, *3*(9), 210–216.

Zekavat, A. R., Jansson, A., Larsson, J., & Pejryd, L. (2019). Investigating the effect of fabrication temperature on mechanical properties of fused deposition modeling parts using X-ray computed tomography. *International Journal of Advanced Manufacturing Technology*, *100*(1-4), 287–296. doi: 10.1007/s00170-018-2664-8

Zhang, W., Wu, A. S., Sun, J., Quan, Z., Gu, B., Sun, B., ... Chou, T. W. (2019). Characterization of residual stress and deformation in additively manufactured

ABS polymer and composite specimens. *Composites Science and Technology*, *150*, 102–110. doi: 10.1016/j.compscitech.2017.07.017

Zhang, Y., & Chou, Y. K. (2006a). A parametric study of part distortions in FDM using FEA. *Engineering Manufacture*, *220*, 410–420.

Zhang, Y., & Chou, Y. K. (2006b). Three-dimensional finite element analysis simulations of the fused deposition modelling process. *Journal of Engineering Manufacture*, *220*, 1663–1672. doi: 10.1243/09544054JEM572

Zhang, Y., & Shapiro, V. (2017). Linear-Time Thermal Simulation of As-Manufactured FDM Components. *ASME 2017 International Design Engineering Technical Conferences and Computers and Information in Engineering Conference*, 1–19.

Zhou, X., Hsieh, S.-j., & Sun, Y. (2017). Experimental and numerical investigation of the thermal behaviour of polylactic acid during the fused deposition process. *Virtual and Physical Prototyping*, *0*(0), 1–13. Retrieved from `https://doi.org/10.1080/17452759.2017.1317214` doi: 10.1080/17452759.2017.1317214

Zhu, Q., Liu, Y., Cai, Y., & Wu, M. (2017). Research on the Shrinkage of Model with Hole in PLA Material Based on the FDM 3D Printing. , *154*(Icmia), 547–551. doi: 10.2991/icmia-17.2017.95

Ziemian, C., Sharma, M., & Ziemi, S. (2012). Anisotropic Mechanical Properties of ABS Parts Fabricated by Fused Deposition Modelling. *Mechanical Engineering*, *10*(1), 160–180. doi: 10.5772/34233

APPENDICES

Appendix I: Genetic Algorithm

```
ObjFcn= @multiresponsesf;
nvars =3;
LB =[255 0.1 30];
UB =[275 0.3 50];
ConsFcn=@gaudencec; %myConstraints;
%IntCon=[1 1 1];
options.PopulationSize = 200;
%options = gaoptimset('plotfcns',{@gaplotbestf,@gaplotbestindiv},'CrossoverFcn',@crossoversinglepoint,
%options = gaoptimset(options,'OutputFcn',@myoutputfcn);
%----- put this (in the main your code)
[x,fval]=ga(ObjFcn,nvars,[],[],[],[],LB,UB,ConsFcn,options)
%[x,fval]=ga(ObjFcn,nvars,[],[],[],[],LB,UB,ConsFcn,options)%gaoptimset('Display','iter'))
```

Figure A.1: Genetic algorithm code

Appendix II: Residual Stress Results

Table B.1: Measured strains and principal stresses

Depth (mm)	ϵ_1 (μ**m**)	ϵ_2 (μ**m**)	ϵ_3 (μ**m**)	σ_{Min} **(MPa)**	σ_{Max} **(MPa)**	**beta** (°)
0.025	103.66	259.55	172.67	9.2	14.2	-8.5
0.075	109.3	254.89	177.03	15.9	22.2	-25.5
0.125	111.71	236.87	175.4	21.3	31.2	-40.6
0.175	123.89	280.63	196.61	26.3	40.7	-48.4
0.225	133.48	288.23	190.18	22.9	37.2	-51.9
0.275	153	315.75	220.04	16.5	24.2	-52.8
0.325	153.03	299.31	218.22	2.3	6	30.1
0.375	148.47	267.1	206.59	-15.2	-2.2	31.8
0.425	150.01	278.52	190.66	-24.8	-7	31.7
0.475	138.77	248.18	182.28	-19.9	-7.5	30.1
0.525	137.29	264.18	153.99	-4.2	0.3	-42.9
0.575	124.31	213.23	145.03	-1.2	20.1	-51.3
0.625	97.97	177.88	145.03	-0.7	30.2	-50.2
0.675	133.84	214.43	168.01	-6.4	20.3	-43.5
0.725	149	240.09	161.34	-18.2	-3.2	-22.2
0.775	117.7	95.93	113.32	-30	-18.3	7.3
0.825	61.57	36.49	75.85	-26.4	-25	40
0.875	48.05	68.43	50.64	-20.8	-2.1	-61.6
0.925	52.83	46.18	29.19	-18	-0.2	-21.7
0.975	11.48	9.22	14.37	-27.1	-9.6	58.9